ORNL/NUREG/TM-120

Heavy-Section Steel Technology Program Quarterly Progress Report for January—March 1977

G. D. Whitman

Prepared for the U.S. Nuclear Regulatory Commission
Office of Nuclear Regulatory Research
Under Interagency Agreements ERDA 40-551-75 and ERDA 40-552-75

OAK RIDGE NATIONAL LABORATORY
OPERATED BY UNION CARBIDE CORPORATION FOR THE ENERGY RESEARCH AND DEVELOPMENT ADMINISTRATION

Printed in the United States of America. Available from
National Technical Information Service
U.S. Department of Commerce
5285 Port Royal Road, Springfield, Virginia 22161
Price: Printed Copy ~~$5.50~~ $6.50 Microfiche $3.00

ORNL/NUREG/TM-120
Dist. Category NRC-5

Contract No. W-7405-eng-26

Engineering Technology Division

HEAVY-SECTION STEEL TECHNOLOGY PROGRAM QUARTERLY PROGRESS REPORT FOR JANUARY—MARCH 1977

G. D. Whitman

Manuscript Completed — August 5, 1977
Date Published — September 1977

NOTICE: This document contains information of a preliminary nature. It is subject to revision or correction and therefore does not represent a final report.

Prepared for the
U.S. Nuclear Regulatory Commission
Office of Nuclear Regulatory Research
Under Interagency Agreements ERDA 40-551-75 and ERDA 40-552-75

Prepared by the
OAK RIDGE NATIONAL LABORATORY
Oak Ridge, Tennessee 37830
operated by
UNION CARBIDE CORPORATION
for the
ENERGY RESEARCH AND DEVELOPMENT ADMINISTRATION

CONTENTS

PREFACE

The Heavy-Section Steel Technology (HSST) Program is a Nuclear Regulatory Commission (NRC)-sponsored engineering research activity devoted to extending and developing the technology for assessing the margin of safety against fracture of the thick-walled steel pressure vessels used in light-water-cooled nuclear power reactors. The program is being carried out in close cooperation with the nuclear power industry. This report covers HSST work performed from January to March 1977, except for subcontractor contributions which may cover the three-month period ending in February. The Oak Ridge National Laboratory (ORNL) work and subcontracts are managed by the Engineering Technology Division. Major tasks at ORNL are carried out by the Engineering Technology Division and the Metals and Ceramics Division. Prior progress reports on this program are ORNL-4176, ORNL-4315, ORNL-4377, ORNL-4463, ORNL-4512, ORNL-4590, ORNL-4653, ORNL-4681, ORNL-4764, ORNL-4816, ORNL-4855, ORNL-4918, ORNL-4971, ORNL/TM-4655 (Vol. II), ORNL/TM-4729 (Vol. II), ORNL/TM-4805 (Vol. II), ORNL/TM-4914 (Vol. II), ORNL/TM-5021 (Vol. II), ORNL/TM-5170, ORNL/NUREG/TM-3, ORNL/NUREG/TM-28, ORNL/NUREG/TM-49, ORNL/NUREG/TM-64, and ORNL/NUREG/TM-94.

SUMMARY

1. PROGRAM ADMINISTRATION AND PROCUREMENT

The Heavy-Section Steel Technology (HSST) Program is an engineering research activity being conducted by the Oak Ridge National Laboratory (ORNL) for the Nuclear Regulatory Commission (NRC) in coordination with other research sponsored by the federal government and private organizations. The program comprises studies relating to all areas of the technology of the materials fabricated into thick-section primary-coolant containment systems of light-water-cooled nuclear power reactors. The principal area of investigation is the behavior and structural integrity of steel pressure vessels containing cracklike flaws. Current work is organized into the following tasks: (1) program administration, (2) fracture mechanics analyses and investigations, (3) effect of high-temperature primary reactor water on the subcritical crack growth of the reactor vessel steel, (4) investigations of irradiated materials, (5) pressure vessel investigations, (6) thermal shock investigations, (7) foreign research, and (8) prestressed concrete reactor vessel (PCRV) tendon corrosion studies.

Work under the four existing research and development subcontracts is included in this report.

During this quarter, 15 briefings or presentations were made.

2. FRACTURE MECHANICS ANALYSES AND INVESTIGATIONS

Two photoelastic models of boiling-water-reactor (BWR) vessels with feedwater nozzles have been tested and a third model is being tested. Measured stress-intensity factors for the BWR models are close to the values determined previously from models of intermediate test vessels if all values are normalized by an average hoop stress.

3. EFFECT OF HIGH-TEMPERATURE PRIMARY REACTOR WATER ON THE SUBCRITICAL CRACK GROWTH OF REACTOR VESSEL STEEL

Wedge-opening-loading specimens of pressure vessel steels are being fatigued in five chambers, where they are also exposed to pressurized-water reactor (PWR) primary coolant environments. The effects on crack growth rate of ramp and hold times, low cyclic frequency, and high ΔK are currently being studied; in addition, specimens of submerged-arc weld metal are being tested.

Measurements of striation spacing observed microscopically have been used to increase the amount of data from which crack growth rates are deduced in studying the effects of hold time. The striation and original data agree, indicating that crack growth rates with trapezoidal loading forms having hold times up to 12 min are about the same as those obtained with sinusoidal loading of equivalent frequency.

Crack growth rates observed in weld metal, although somewhat erratic, are similar to the rates measured in base metal at low R ratios (k_{min}/K_{max}) and substantially less than those in base metal at high R ratios. Additional weld specimens are being tested.

4. INVESTIGATIONS OF IRRADIATED MATERIALS

Irradiation of the three capsules containing 4T compact-tension specimens of submerged-arc weld material was completed in March. On the basis of flux measurements with dummy capsules, the estimated fluences are higher than the target fluence; however, the effect of this deviation on transition temperature shift and upper-shelf energy is expected to be small.

The capability for testing 4T irradiated specimens for ductile fracture toughness by the unloading compliance method is being developed at Hanford Engineering Development Laboratory (HEDL). Reduction of loading and extensometer hysteresis with the use of bearing grips, linear variable differential transformer (LVDT) load line displacement, and real time test data processing will be the principal goals of the technique development.

5. PRESSURE VESSEL INVESTIGATIONS

Intermediate test vessels V-7B and V-8 were repaired by the Westinghouse Electric Corporation, Tampa Division, using the half-bead weld technique. After return of the vessels and associated test weldments to ORNL, the machined portion of the flaw was put into V-7B. The prolongation of V-8 containing welds typical of both V-7B and V-8 repairs was strain gaged and sectioned for determination of material properties and residual stresses in preparation for testing.

Two steel crack-arrest model vessels were tested in the first of a series of tests required to plan a crack propagation and arrest test in an intermediate vessel. The sharp edge of the prepared flaw in each model was in relatively brittle A533 quenched-only material. Crack growth in both tests at 91 and 4°C (196 and 39°F) was predominantly stable; but in the second test two run-arrest events occurred, one of which arrested in the brittle material while K_I was increasing.

Studies of material properties for the crack-arrest models are continuing. Average yield and ultimate stresses of the brittle material in the first two models are 2 1/2 times the value for the tough sections.

The effect of crack velocity on the stress-intensity factor was studied by means of dynamic finite-element analysis. The effect can be large, with the factor decreasing with increasing velocity. Also, the statically calculated stress-intensity factor may not always be a conservative approximation of the dynamic factor.

The fracture surfaces of the flaw region, removed from intermediate test vessel V-7A after the pneumatic sustained-load test, were examined by light microscopy and scanning electron microscopy. The fracture surfaces formed during the test have a dimpled morphology that is characteristic of cracks extended by ductile tearing.

6. THERMAL SHOCK INVESTIGATIONS

During the reporting period for the LOCA-ECC Thermal Shock Program, the fourth thermal shock experiment (TSE-4) was conducted, metallographic examination of the TSE-1 and TSE-3 fracture surfaces was completed, the

possibility of demonstrating warm prestressing using cryogenic quenching was investigated, an experimental program for determining heat transfer coefficients associated with cryogenic quenching was begun, and progress was made in the development of a three-dimensional finite-element code for calculating stress-intensity factors.

Results from TSE-4 indicate that linear elastic fracture mechanics is quite applicable for a LOCA-ECC thermal shock analysis, and recent scanning electron microscope (SEM) examinations of the fracture surfaces associated with TSE-1 and TSE-3 show that the fracture was ductile (subcritical crack growth) for TSE-1 and was brittle for TSE-3. The SEM results confirm conclusions based on other observations and analysis.

Cryogenic studies indicate that warm prestressing cannot be demonstrated in the present thermal shock test facility, but such a demonstration may be possible using a cryogenic quench. Results from heat transfer experiments show that the heat transfer coefficient for liquid nitrogen can be increased considerably by adding a thin layer of insulation to the heat transfer surface, provided that the initial surface temperature is less than $\sim$70°C (150°F).

7. FOREIGN RESEARCH

Products of foreign research applicable to the safety of light-water reactor (LWR) primary systems are being collected and reviewed systematically. The initial thrust of this activity is to identify research programs and reports of interest, arrange for acquisition of documents, and establish procedures for review of reports and distribution of information.

8. PCRV TENDON CORROSION STUDIES

Slow strain rate ($\sim 2.46 \times 10^{-5}$ per minute) tests have been conducted on the center wire from seven-wire tendons of the type intended for use in PCRVs. Of all the environments tested, only 0.2*M* NH_4NO_3 at 66 and 52°C (150 and 125°F) and sulfide at room temperature and with pH values of 4 or less produced cracks.

HEAVY-SECTION STEEL TECHNOLOGY PROGRAM QUARTERLY PROGRESS REPORT FOR JANUARY–MARCH 1977

G. D. Whitman

ABSTRACT

The Heavy-Section Steel Technology (HSST) Program is an engineering research activity conducted by the Oak Ridge National Laboratory for the Nuclear Regulatory Commission. It comprises studies related to all areas of the technology of the materials fabricated into thick-section primary-coolant systems of light-water-cooled nuclear power reactors. The principal area of investigation is the behavior and structural integrity of steel pressure vessels containing cracklike flaws. Current work is organized into eight tasks: program administration and procurement, fracture mechanics analyses and investigations, effect of high-temperature primary reactor water on subcritical crack growth, investigations of irradiated materials, pressure vessel investigations, thermal shock investigations, foreign research, and prestressed concrete reactor vessel (PCRV) tendon corrosion studies.

Stress-intensity factors measured on photoelastic models of BWR vessels with nozzles are consistent with values from vessel burst tests. Subcritical crack growth specimens are being subjected to low-frequency cyclic loading and ramp and hold cycles in a PWR environment. Intermediate test vessels V-7B and V-8 were repaired by the half-bead welding technique prescribed in Section XI of the ASME Boiler and Pressure Vessel Code in preparation for testing with flaws in the repair zones, and the first two crack arrest model vessels were tested. The fourth thermal shock experiment indicated that linear elastic fracture mechanics analysis is applicable to a loss-of-coolant type of thermal shock to a reactor pressure vessel. Fractographic examination of fracture surfaces of earlier experiments confirmed the character of the fractures.

1. PROGRAM ADMINISTRATION AND PROCUREMENT

G. D. Whitman

The Heavy-Section Steel Technology (HSST) Program is a major Nuclear Regulatory Commission (NRC)-sponsored safety program concerned with the structural integrity of the primary systems, particularly the reactor pressure vessel, of water-cooled nuclear power reactor stations. Almost

all areas of materials technology relating to the steels and weldments used in fabricating the vessels of present and contemplated plants in the United States have been or are being investigated. Extensive studies have been made of the metallurgical, mechanical, and toughness properties exhibited by typical reactor vessel product forms. Quantitative techniques for determining toughness properties, which may be used in analytical methods for predicting structural behavior in the presence of flaws, have been developed. Plates, forgings, and weldments are being investigated, including the effects of cyclic crack propagation, environmental corrosion, and irradiation.

One of the major objectives of the HSST program is to quantitatively relate the flaw size (under a specified constraint condition), load, and toughness at which fracture will occur over the temperature range of interest for water-cooled reactors [from room temperature to around 288°C (550°F)]. Such a relationship would allow the margin of safety against fracture of a structure to be calculated. Currently, major emphasis is on the development of a technology that is capable of making quantitative engineering calculations of fracture conditions using conservative parameters. Such a technology provides for the assessment of the fracture, burst, or leakage potential of water-cooled reactor pressure vessels as well as other structural components of the primary containment system during all phases of normal operation and under conditions imposed by accidents.

The program is coordinated with other government agencies and the manufacturing and utility sectors of the nuclear power industry in the United States and abroad. The overall objective is a quantification of safety assessments for regulatory agencies, professional code-writing bodies, and the nuclear power industry. Several of the activities are conducted under subcontracts by research facilities in the Unites States and through informal cooperative efforts on an international basis. Four research and development subcontracts are currently in force.

Administratively, the program is organized into eight tasks, as reflected in this report: program administration and procurement, fracture mechanics analyses and investigations, effect of high-temperature

primary water on subcritical crack growth of reactor vessel steel, investigations of irradiated material, pressure vessel investigations, thermal shock investigations, foreign research, and prestressed concrete reactor vessel (PCRV) tendon corrosion studies. The last task, instituted this fiscal year, is included in the HSST program for administrative convenience.

Fifteen program briefings, reviews, or presentations were made by the HSST staff during this quarter at technical meetings, at program reviews for NRC staff, or for visitors.

2. FRACTURE MECHANICS ANALYSES AND INVESTIGATIONS

2.1 Stress Intensities for Nozzle Cracks in Reactor Vessels*

C. W. Smith† W. H. Peters†

2.1.1 Introduction

Stress-intensity factor determination for cracks emanating from pressure vessel nozzles has been an unsolved problem in the reactor vessel industry for many years due to the complex and widely varying geometries involved. To date, only approximate analytical solutions, such as those of Hellen and Dowling,[1] Reynen,[2] Broekhoven and Spaas,[3] and Schmitt,[4] are available in the open literature; but substantial additional efforts are under way.

As a result of the degree of analytical intractability of the problem and the need for experimental correlation of approximate analytical methods such as the finite-element method (FEM), the authors have undertaken several experimental investigations. The experimental technique employed has been developed by the authors over a period of years.[5-12] It consists of a union between the "frozen stress" photoelastic analysis of cracked bodies and a simplified digital computer analysis of the experimental data for determining the stress-intensity factor.

This study has consisted of two phases to date. The first involved applying the above technique to a cracked nozzle geometry identical to that studied by Derby.[13] Results showed good agreement with Derby's residual static strength fracture data, except for shallow flaws (a/T = 0.25), where the stress-intensity factors were 15% below Derby's results, the latter of which showed a scatter of about ±7%. Results of the first phase of the study are found in Ref. 14.

---

*Research performed by the Photoelasticity and Fracture Laboratory, Engineering Science and Mechanics Dept., Virginia Polytechnic Institute and State University for the HSST program under UCCND Subcontract 7015 between Union Carbide Corporation and Virginia Polytechnic Institute and State University.

†Engineering Science and Mechanics Department, Virginia Polytechnic Institute and State University.

Once the Derby residual static strength technique was verified, the present study entered phase II, which involved frozen stress photoelastic determination of stress-intensity factor distributions for a scale model of a cracked inlet nozzle for an existing BWR vessel design. The analytical phases of the technique are briefly reviewed and the results noted and compared with other studies.

2.1.2 Analytical considerations

The maximum shearing stress in the n-z plane along $\theta = \pi/2$ (Fig. 2.1) near the crack tip can be expressed as:[9]

$$\tau_{max} = \frac{A}{r^{1/2}} + B \ , \qquad (2.1)$$

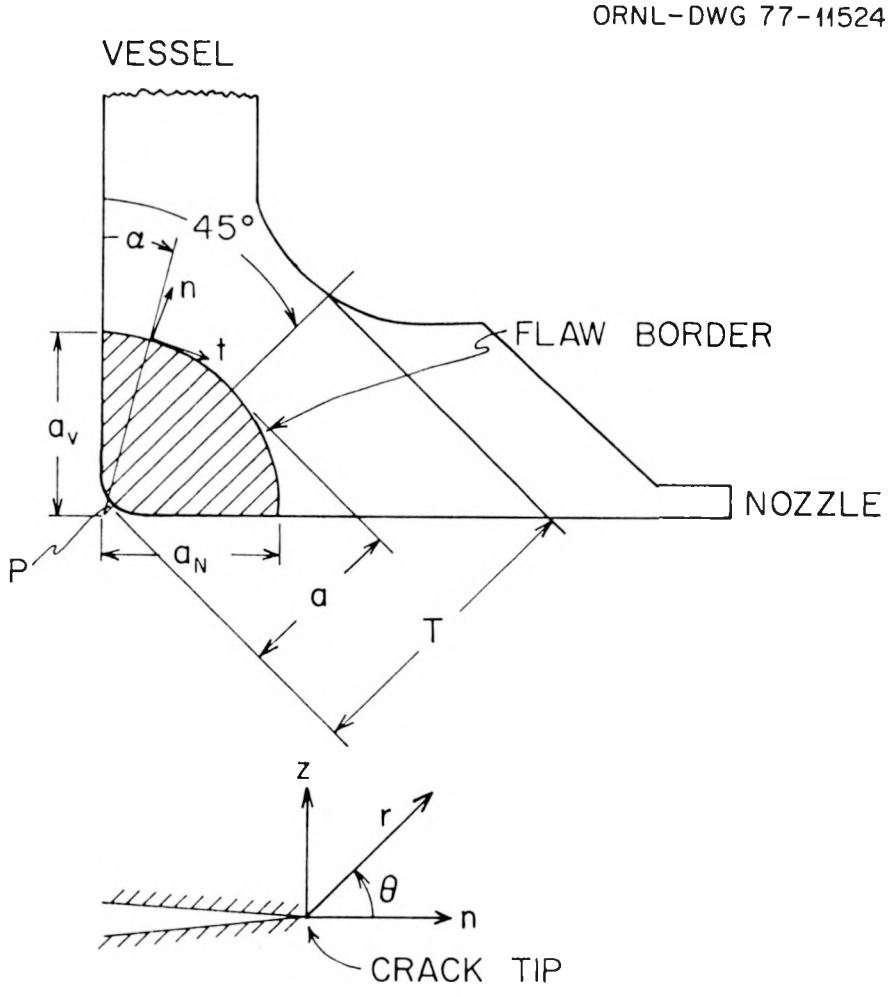

Fig. 2.1. Local problem geometry and notation.

where $A = K_I/(8\pi)^{1/2}$, K_I = stress-intensity factor, and B is the leading term of a Taylor series expansion of the regular stress field near the crack tip. Data are taken along $\theta = \pi/2$ since fringes tend to spread in that direction (Fig. 2.2). From the Stress Optic Law,

$$\tau_{max} = \frac{Nf}{2t'} , \tag{2.2}$$

where N is the stress fringe order, f is the material fringe value, and t' is the slice thickness parallel to the crack front. The zone in which Eq. (2.1) is valid can be determined experimentally by rewriting the equation in normalized form:

$$\frac{\tau_{max}\,(8\pi r)^{1/2}}{p(\pi a)^{1/2}} = \frac{K_I}{p(\pi a)^{1/2}} + \frac{B\,(8\pi r)^{1/2}}{p(\pi a)^{1/2}} \tag{2.3}$$

or

$$\frac{K_{AP}}{p(\pi a)^{1/2}} = \frac{K_I}{p(\pi a)^{1/2}} + \frac{B(8)^{1/2}}{p}\left(\frac{r}{a}\right)^{1/2} , \tag{2.4}$$

where $K_{AP} = \tau_{max}\,(8\pi r)^{1/2}$ is defined as "apparent" stress-intensity factor and p = the internal pressure. Equation (2.4), when plotted as $K_{AP}/p(\pi a)^{1/2}$ vs $(r/a)^{1/2}$, yields a straight line which will yield $K_I/p(\pi a)^{1/2}$, the normalized stress-intensity factor, when extrapolated to the origin. The above approach for mode I loading has been extended to cover the mixed mode situation.[6,11]

When mode I loads are applied to the crack tip, blunting occurs, producing a nonlinear zone that extends approximately to r/a = 0.04 from the crack tip along $\theta = \pi/2$. The linear zone described by Eq. (2.4) extends substantially from the crack tip in problems with slowly varying effects along the flaw border (as in the two-dimensional case). Conversely, a constriction of the singular zone occurs in problems with strong three-dimensional effects. However, if a linear zone is present in the raw data plot of normalized apparent stress-intensity factor vs $(r/a)^{1/2}$, then the presence of the desired data zone is assured.

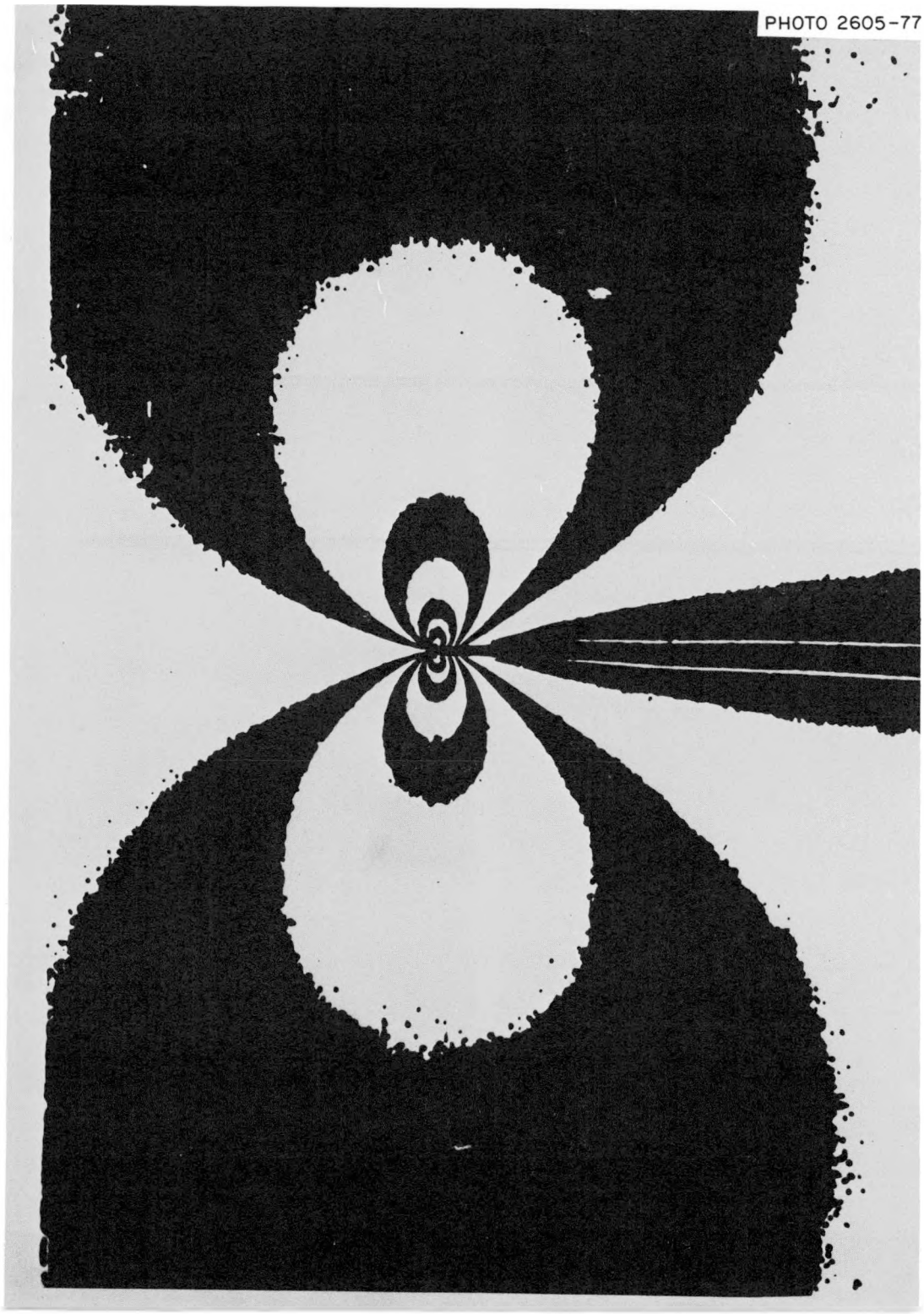

Fig. 2.2. Typical mode I fringe pattern.

2.1.3 Experiments

The present contract calls for the manufacture and testing of sufficient models to accumulate eight valid sets of test data (including near replications) from nozzles containing different size flaws. Model geometry is given in Fig. 2.3 and an assembled model is pictured in Fig. 2.4. Two nozzles are located at diametrically opposite positions on each model. The test procedure is as follows:

1. Starter cracks were made on the "inner" surface of the juncture of the vessel wall with the nozzle at point P (Fig. 2.1). The photoelastic models were then glued together, placed in a test rig in a stress freezing electric oven, and heated to a critical temperature.

2. Vessels were pressurized while being supported in soft, surface-matching, part-spherical bases. Pressure was increased until the flaws had grown to desired dimensions. The models were then cooled under reduced pressure to room temperature, freezing in both fringe and deformation fields.

3. Slices were taken mutually orthogonal to the flaw border and the flaw surface at intervals along the border. The slices were coated with a fluid having the same index of refraction as the model material and analyzed by the Tardy method. A crossed circular polariscope set at about 10× magnification, with a white light field, was used to read tint of passage.

4. Optical data were introduced into a least-squares computer program which extracted estimates of the stress-intensity factor.

2.1.4 Data and results

Two models (four nozzles) have been tested. However, data from one nozzle (a very shallow flaw) did not exhibit a linear region, probably because the crack shape was not planar, and data were consequently discarded. Data on valid tests obtained to date are given in Table 2.1. (Tests 1A and 1B may be regarded as near replications.) Figure 2.5 shows a typical set of data revealing the desired linear zone, and Fig. 2.6 shows actual flaw geometries studied.

The stress-intensity factor distributions obtained to date are shown in Fig. 2.7 normalized with respect to both p and $\bar{\sigma}$ for comparison of

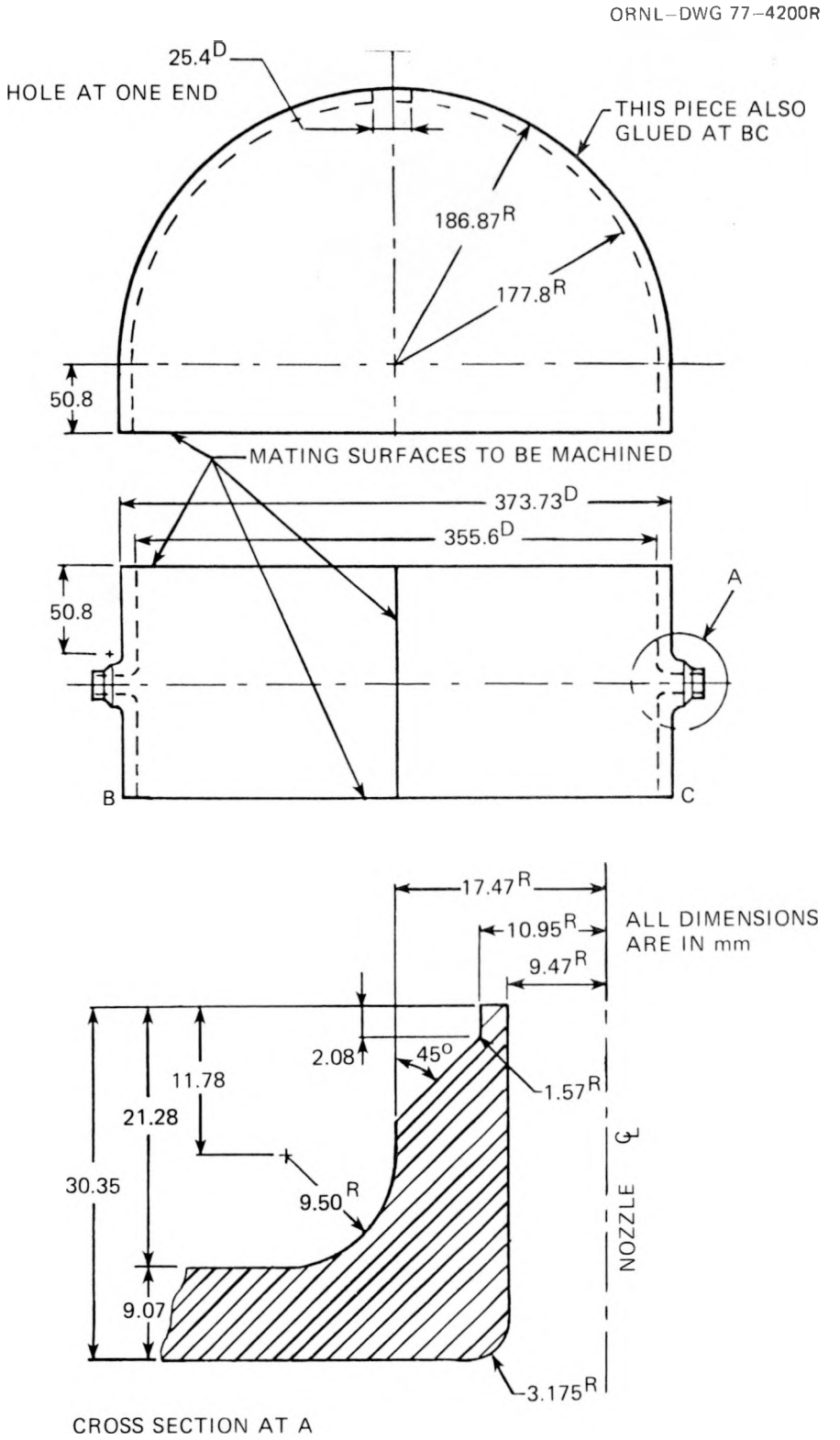

Fig. 2.3. Boiling-water reactor model and nozzle detail (1 mm = 0.039 in.).

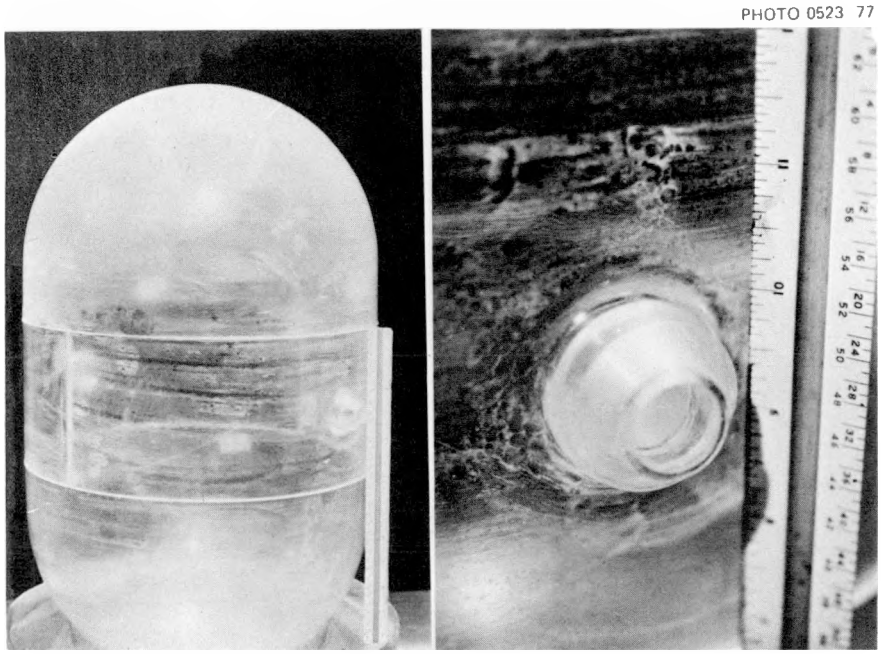

Fig. 2.4. Assembled BWR model vessel and closeup of nozzle.

Table 2.1. Data from tests of two BWR model vessels

Parameter[a]	1A	1B	2A	2B[b]
p (kPa)	2.76	2.76	2.62	2.62
a_v (mm)	10.67	10.16	16.51	6.60
a_n (mm)	10.67	10.16	13.72	5.59
a (mm)	8.56	7.96	12.19	4.57
a/T[c]	0.57	0.53	0.81	0.30

[a] See Fig. 2.1 for definition of geometric parameters.

[b] Initial flaw inclined to plane of flaw geometry.

[c] T = 15.1 mm for all tests.

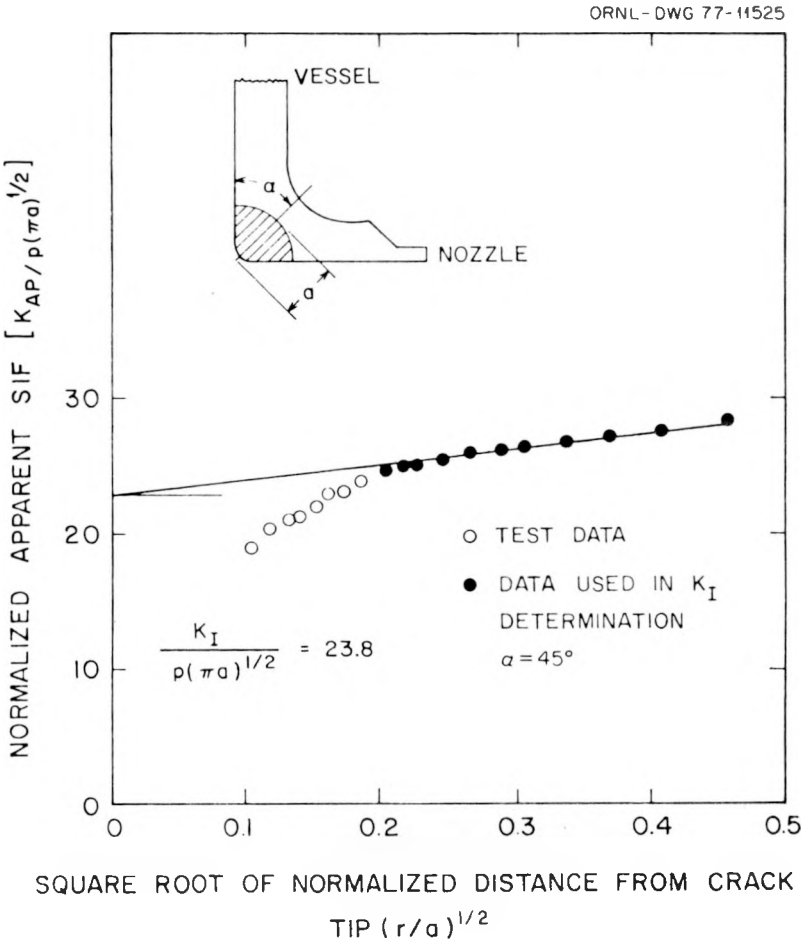

Fig. 2.5. Typical raw fringe data and K_I estimation.

results of the phase II tests with results from the thick-wall vessel tests of phase I. These results show the same trends as in phase I, which indicates that the maximum stress-intensity factor occurs near the center of the flaw border for moderate to deep flaws. The $\bar{\sigma}$ for the thick-walled vessel in Fig. 2.7 is the integrated average Lamé hoop stress across the wall thickness. Even for moderately deep flaws, the effects of variations in back surface geometry (see Fig. 2.8) are less than the difference in T'/R_i in the pressure vessels, which appears to dominate the stress-intensity factor level in the nozzle.

The above remarks are based upon results from only three sets of data and should be regarded as conjectural pending completion of phase II of the project. The third model is currently being tested.

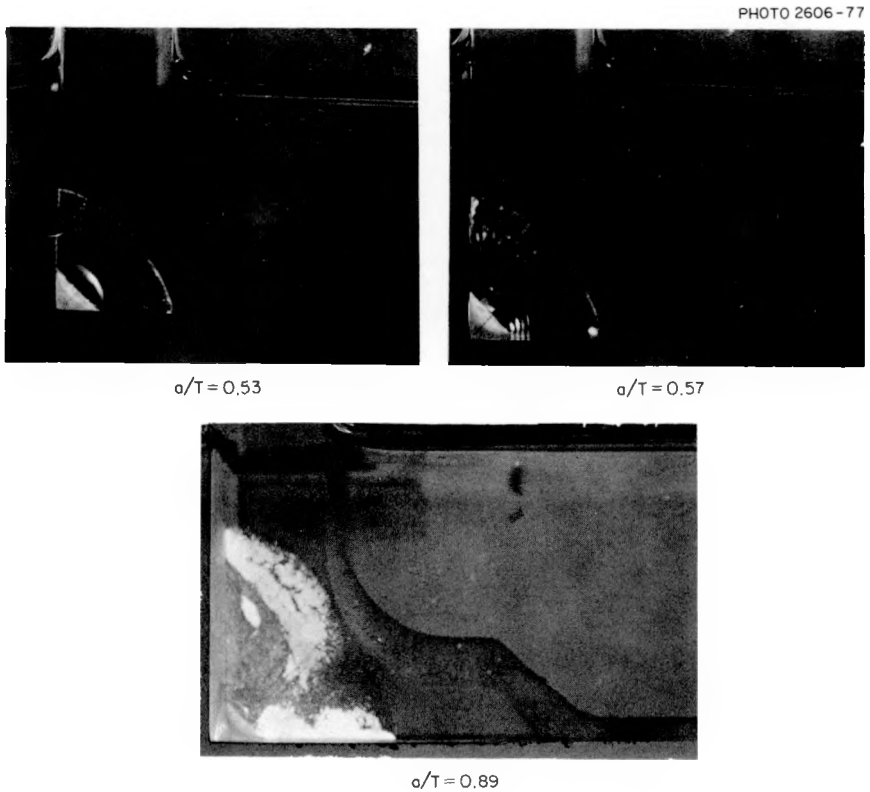

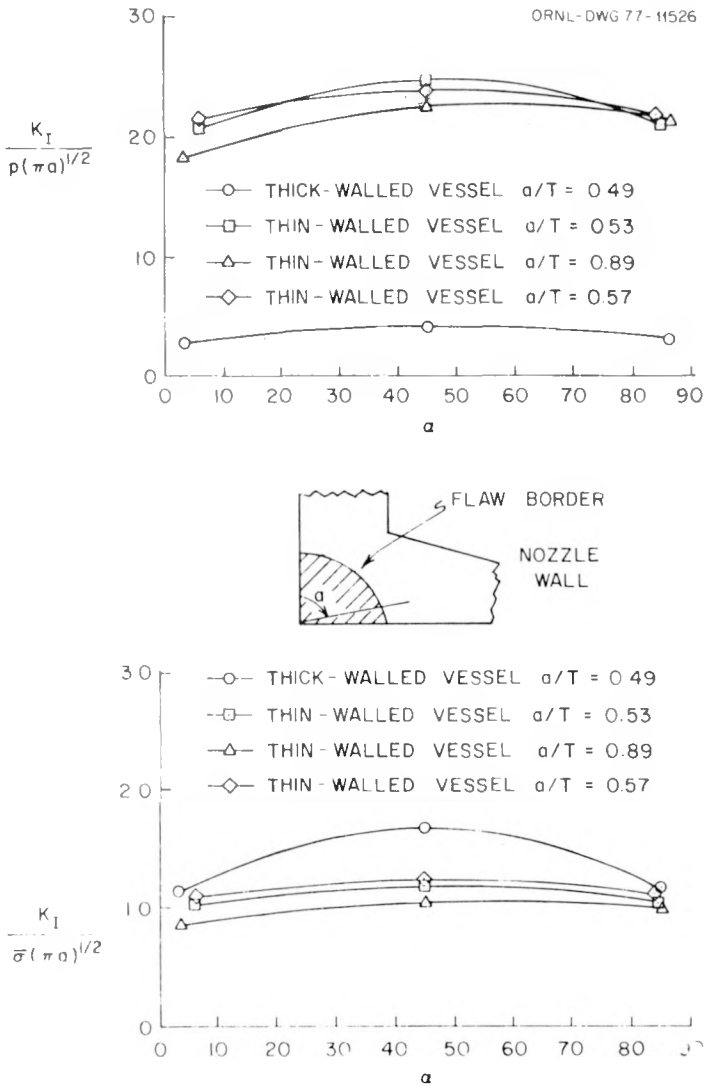

Fig. 2.7. K_I distribution along the flaw border.

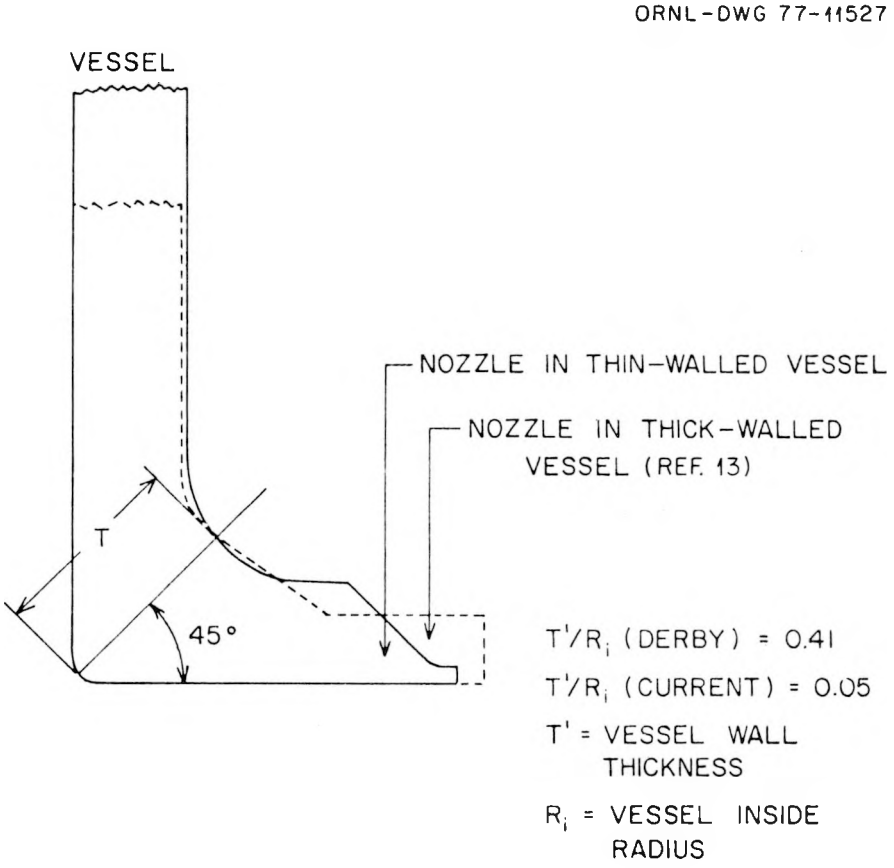

Fig. 2.8. Geometries of BWR model nozzle and Derby's (ITV) model nozzle normalized to the same T.

References

1. T. K. Hellen and A. H. Dowling, "Three Dimensional Crack Analysis Applied to an LWR Nozzle-Cylinder Intersection," *Int. J. Pressure Vessels Piping* 3, 57–74 (1975).

2. J. Reynen, "On the Use of Finite Elements in the Fracture Analysis of Pressure Vessel Components," *Trans. ASME, Pressure Vessel Technol.* 98(1), 8–16 (February 1976).

3. M. G. J. Broekhoven and H. A. C. M. Spaas, *Application of the Finite Element Technique to a Complex 3-D Elastic Problem (Nozzle Junction with Cracks)*, Report MMPP101, Laboratory for Nuclear Engineering, Delft University of Technology (August 1974).

4. W. Schmitt et al., "Calculation of Stress Intensity Factors for Cracks in Nozzles," *Int. J. Fract. Mech.* 12(3), 381–90 (June 1976).

5. D. G. Smith and C. W. Smith, "A Photoelastic Investigation of Closure and Other Effects upon Local Bending Stresses in Cracked Plates," *Int. J. Fract. Mech.* 6(3), 305–18 (September 1970).

6. D. G. Smith and C. W. Smith, "Photoelastic Determination of Mixed Mode Stress Intensity Factors," *Eng. Fract. Mech.* 4(73), 357–66 (1972).

7. C. W. Smith, J. J. McGowan, and M. Jolles, "Effects of Artificial Cracks and Poisson's Ratio upon Photoelastic Stress Intensity Determination," *Exp. Mech.* 16(5), 188–93 (May 1976).

8. J. J. McGowan and C. W. Smith, "Stress Intensity Factors for Deep Cracks Emanating from the Corner Formed by a Hole Intersecting a Plate Surface," *Mechanics of Crack Growth*, ASTM STP 590, American Society for Testing and Materials, pp 460–76, 1976.

9. M. Jolles, J. J. McGowan, and C. W. Smith, "Use of a Hybrid Computer Assisted Photoelastic Technique for Stress Intensity Determination in Three-Dimension Problems," pp 63–82, *Computational Fracture Mechanics*, E. F. Rybicki and S. E. Benzley, eds., ASME, New York, 1975.

10. C. W. Smith, M. Jolles, and W. H. Peters, "Stress Intensity Determination in Three-Dimensional Problems by the Photoelastic Method," *Proceedings of the Second International Conference on Mechanical Behavior of Materials*, pp 235–39, 1976.

11. C. W. Smith, M. Jolles, and W. H. Peters, "Stress Intensities for Cracks Emanating from Pin Loaded Holes," for Proceedings of 10th National Symposium on Fracture Mechanics, 1976.

12. C. W. Smith, M. Jolles, and W. H. Peters, "Stress Intensities in Flawed Pressure Vessels," for Third International Conference on Pressure Vessel Technology, 1977.

13. R. W. Derby, "Shape Factors for Nozzle Corner Cracks," *Exp. Mech.* 12(12), 580–84 (December 1972).

14. C. W. Smith, M. Jolles, and W. H. Peters, *Stress Intensities for Nozzle Cracks in Reactor Vessels*, V.P.I.-E-76-25, 21 pp (November 1976).

3. EFFECT OF HIGH-TEMPERATURE PRIMARY REACTOR WATER ON THE SUBCRITICAL CRACK GROWTH OF REACTOR VESSEL STEEL*

W. H. Bamford† D. M. Moon† K. V. Scott†

3.1 Introduction

The objective of this continuing program is to characterize the fatigue crack growth rate properties of ferritic vessel steels exposed to PWR primary coolant environments. Five chambers are presently in use, and the following areas are being investigated:

Ramp and hold time effects (2T WOL specimens)	1 chamber [14 MPa, 288°C (2000 psi, 550°F)] 1 chamber [0.14 MPa, 93°C (20 psi, 200°F)]
Cyclic frequency effects (2T WOL specimen now being tested at 0.1 cpm)	1 chamber (14 MPa, 288°C)
Crack growth rates at high ΔK values (4T specimens, 1 cpm)	1 chamber (14 MPa, 288°C)
Crack growth in weldments (2T WOL specimens)	1 chamber (14 MPa, 288°C)

In addition to the testing specified by the program, efforts are under way to derive a further understanding of the fatigue crack growth process in steels exposed to this environment by fractographic examination. A section of this report will be devoted to recent findings in this area.

3.2 Ramp and Hold Time Effects

This task involves a series of tests with trapezoidal loading forms consisting of programmed ramp and hold times as summarized in Table 3.1.

---

*Work sponsored by HSST program under UCCND Subcontract 3290 between Union Carbide Corporation and Westinghouse Electric Corporation.

†Westinghouse Electric Corporation.

Table 3.1. Projected ramp and hold time tests of 2T-WOL specimens in PWR environment, A508 class 2 forging material[a]

Test	Ramp time (min)	Hold time (min)	Crack growth [mm (in.)]
2a1	Rapid	1	10 (0.4)
2a2	Rapid	3	10 (0.4)
2a3	Rapid	12	10 (0.4)
2a4	Rapid	60	10 (0.4)
2b1	1	1	10 (0.4)
2b2	1	3	10 (0.4)
2b3	1	12	10 (0.4)
2b4	1	60	10 (0.4)
2c1	5	1	10 (0.4)
2c2	5	3	10 (0.4)
2c3	5	12	10 (0.4)
2c4	5	60	10 (0.4)

[a]WOL = wedge opening loading.

The objective is to determine whether or not hold time has a significant effect on crack growth rates, an important question since reactor vessel operational loadings often involve such hold times. It is also of interest to determine if crack growth rates obtained with the trapezoidal loading form are equivalent to those from sinusoidal loading forms which have been used to generate the majority of the available data. Testing during this report period continued on the second phase of the test sequence, with a ramp time of 1 min and three different hold times. This phase should be completed during the next report period.

Data obtained during the first phase, summarized in the previous quarterly report,[1] showed that hold time had no significant effect. This conclusion was reached with the limited data for the 12-min hold time on specimen F-2; so the fracture surface was examined microscopically to attempt to obtain more data. Crack growth rate data obtained from striation spacing measurements agreed well with the single point previously reported. These are summarized in Table 3.2 and are shown in Fig. 3.1.

Table 3.2. Crack growth rate determinations for striation spacing measurements (specimen F-2 — 12-min hold time)

Average crack depth [in. (mm)]	Striation spacing [in. (mm)]	Magnification	da/dn		ΔK	
			in./cycle	mm/cycle	ksi$\sqrt{\text{in.}}$	MN•m$^{-3/2}$
2.880 (73.15)	0.059 (1.5)	2000×	3×10^{-5}	7.6×10^{-4}	51.09	56.37
2.901 (73.69)	0.079 (2.0)	2000×	4×10^{-5}	1.0×10^{-3}	51.27	56.57
2.923 (74.24)	0.079 (2.0)	2000×	4×10^{-5}	1.0×10^{-3}	51.47	56.79
2.945 (74.80)	0.098 (2.5)	2000×	5×10^{-5}	1.3×10^{-3}	51.66	57.00
2.966 (75.35)	0.098 (2.5)	2000×	5×10^{-5}	1.3×10^{-3}	51.85	57.21

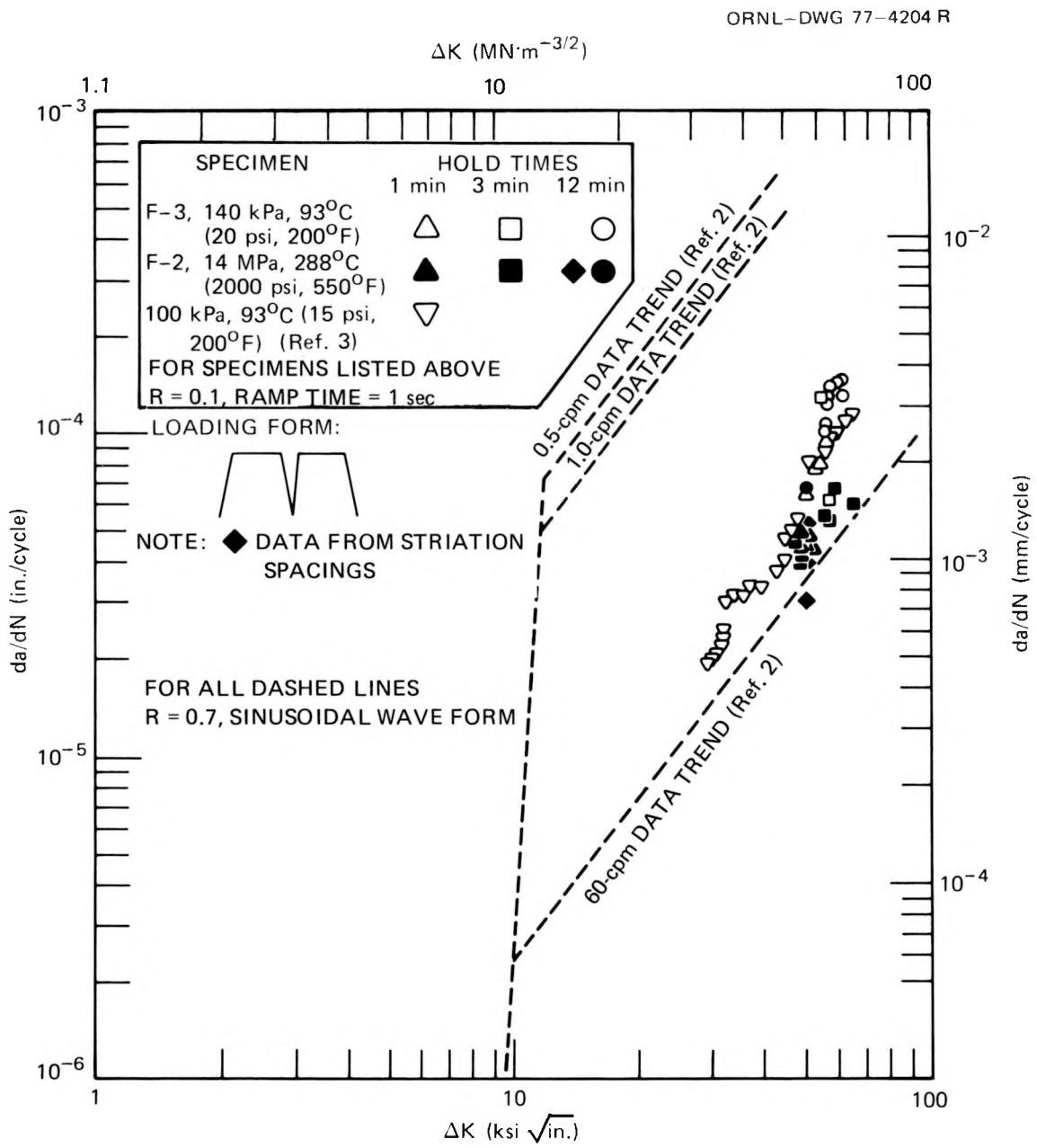

Fig. 3.1. Effect of hold time on fatigue crack growth for A508 class 2 forging steel in water environments with data from fractographic measurements included.

3.3 Cyclic Frequency Effects

It is now well known that fatigue crack growth rates increase at low cyclic frequencies, because the environment has more time to influence the cracking process. This task is designed to determine the frequency at which this effect is maximized and to characterize the effect. Testing is continuing on a specimen of forging material at 0.1 cpm which was begun in August 1976. Experience has shown that tests at such frequencies require eight to ten months to complete.

3.4 Crack Growth Rates at High ΔK Values

This task is devoted to completing the characterization of crack growth in reactor vessel steels throughout the range of loadings normally experienced by operating components. Considerable hardware problems have been experienced in starting the new 4T chamber, but testing is under way and results of the first test are expected during the next reporting period.

3.5 Crack Growth in Weldments

The most likely locations for cracks to be produced during the manufacture of a reactor pressure vessel are in the weld regions. It is thus very important to characterize the fatigue crack growth rate properties of weldments which are typical of those in operating reactor vessels. Results of tests completed on two specimens during this report period are shown in Figs. 3.2 and 3.3. These results are similar to those reported earlier for other specimens from the same weldment. Both showed somewhat erratic crack growth with frequent decelerations of crack growth rate (Figs. 3.2 and 3.3). The same effect of R ratio (K_{min}/K_{max}) previously reported[2-4] for tests of base metal specimens was seen in the weldments. The results now available at low R ratio are shown in Fig. 3.4. Note that the crack growth data for the weldments scatter among the data for the base metal, but the weld data seldom exceed the crack growth rates shown for the base metal. Figure 3.5 provides a similar

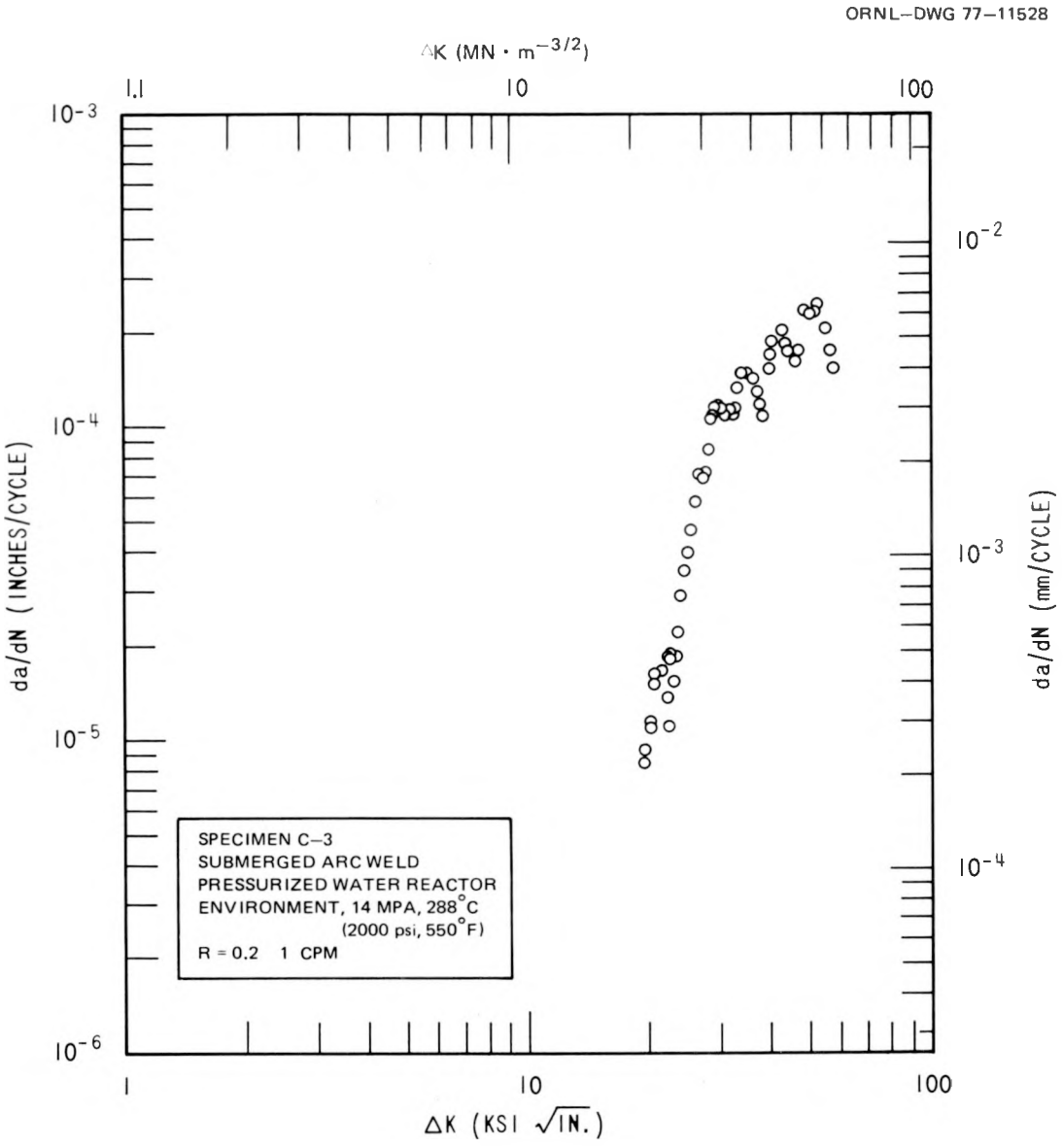

Fig. 3.2. Fatigue crack growth rate results for specimen C-3.

comparison for high R-ratio data. Again the data do not exceed the data for base metals, but in this case the crack growth rates for specimen C-4 fall considerably below the equivalent base metal data. One explanation for this might be the somewhat higher cyclic frequency used in the test.

All the weldment specimens tested thus far at low cyclic frequency have been from the same production weldment, made by the automatic submerged arc process typically used in the fabrication of reactor pressure

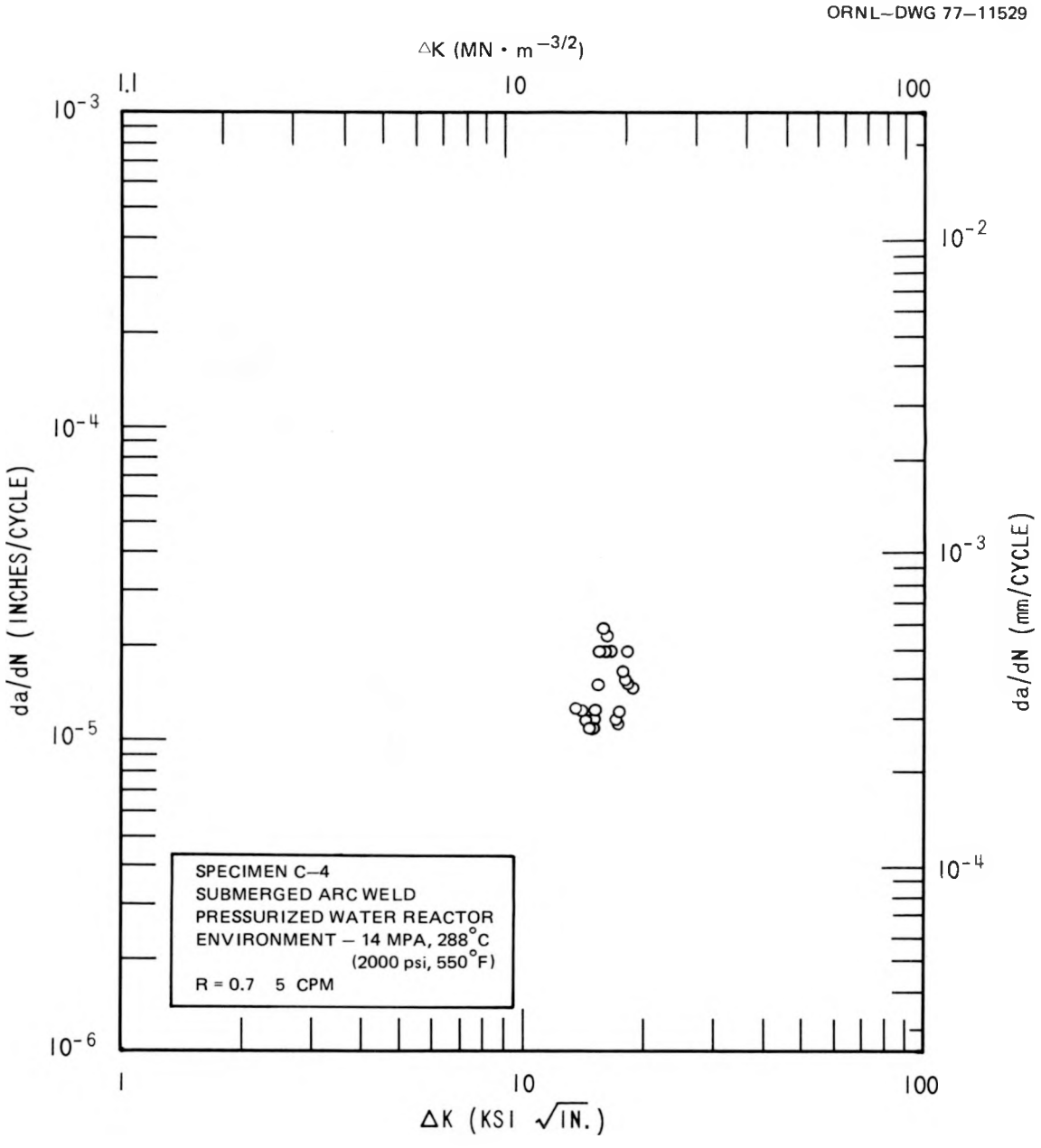

Fig. 3.3. Fatigue crack growth rate results for specimen C-4.

vessels. The specimens were oriented with the crack following the weld direction (Fig. 3.6). Examination has shown that there are four to five uniform weld beads through the thickness of the specimens. The crack planes are such that the crack propagates approximately parallel to the beads, but because of the irregularities in the weld the crack will cross weld beads as it propagates. This could be part of the cause for the

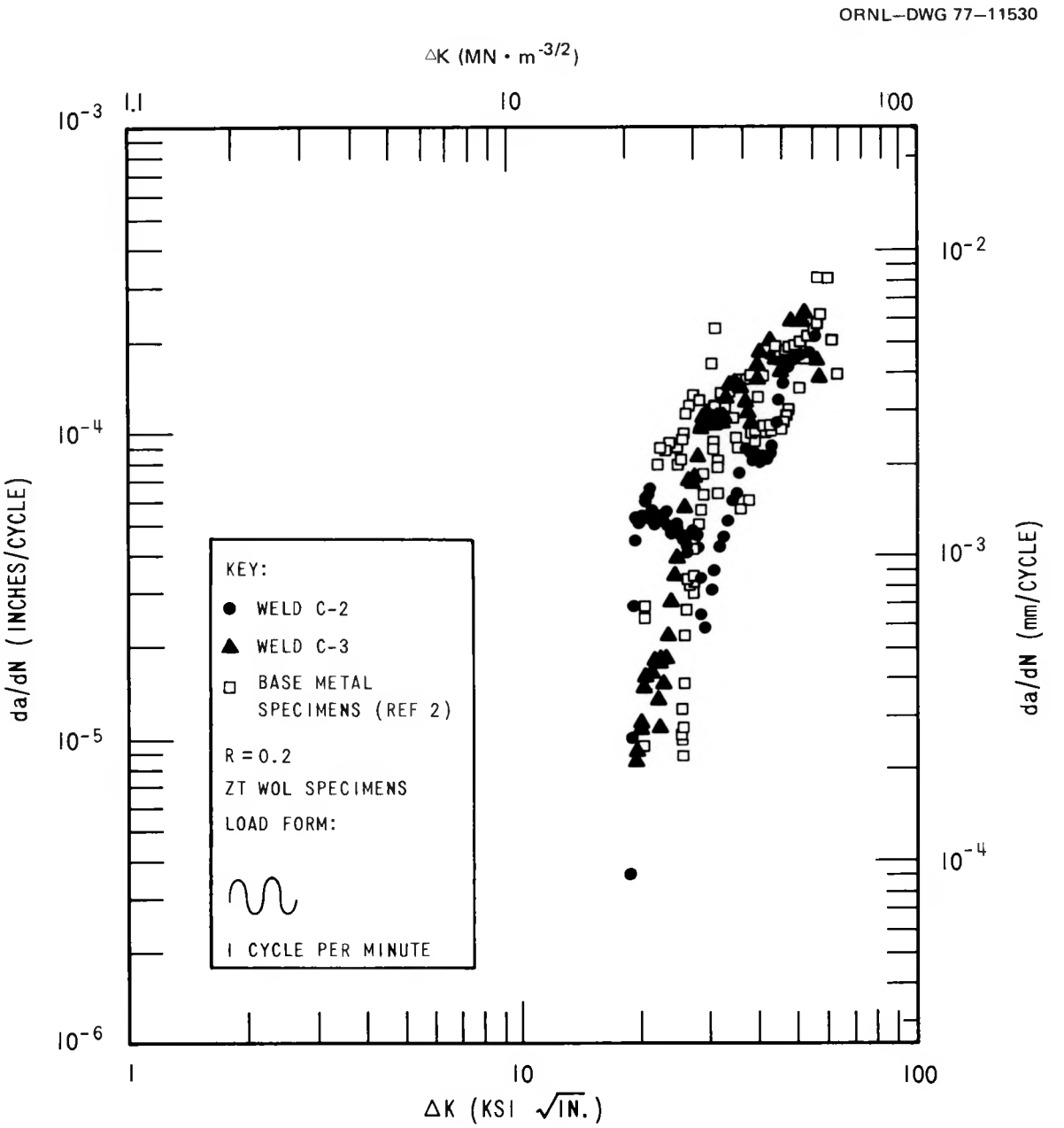

Fig. 3.4. Comparison of weld and base metal crack growth results — low R ratio.

irregular crack growth data obtained. It must be kept in mind that the weld structure is inhomogeneous by design, so irregular crack growth rates are not altogether unexpected. Testing is continuing to study this weld behavior, and at least one different weldment will be tested in the near future.

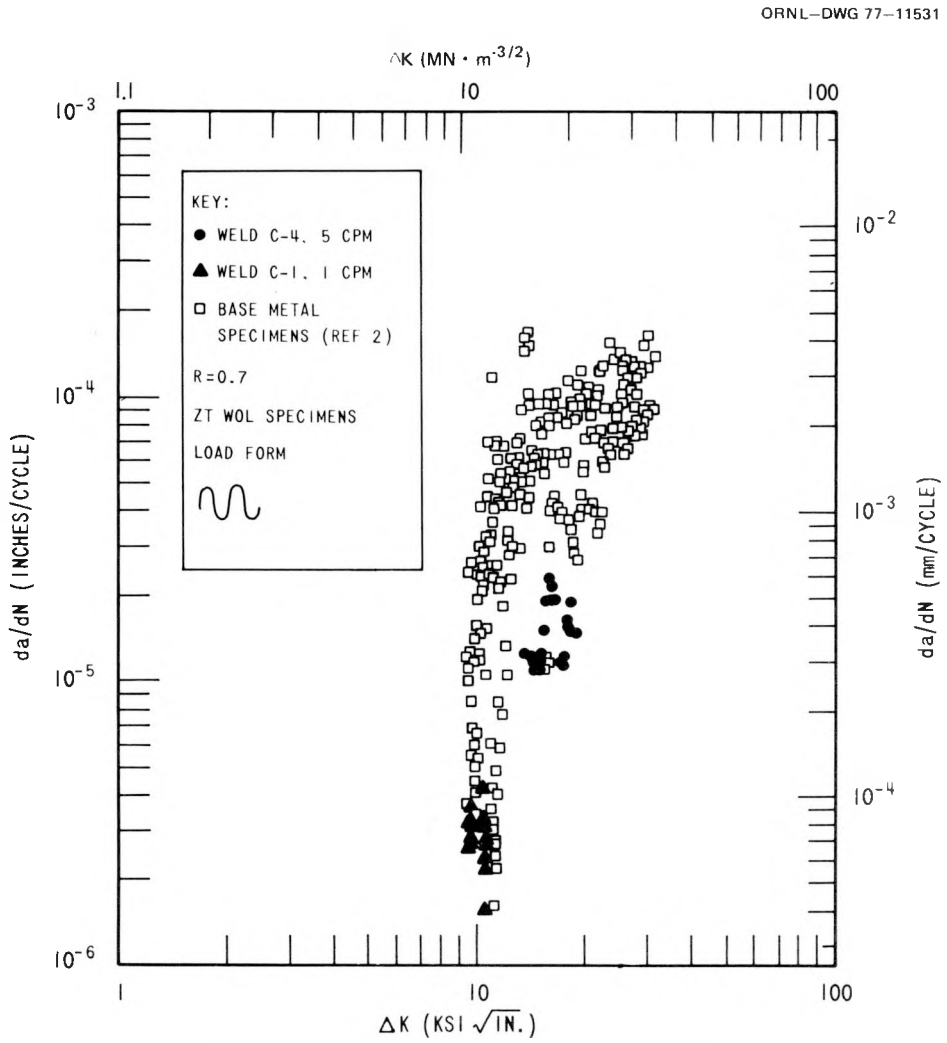

Fig. 3.5. Comparison of weld and base metal crack growth results — high R ratio.

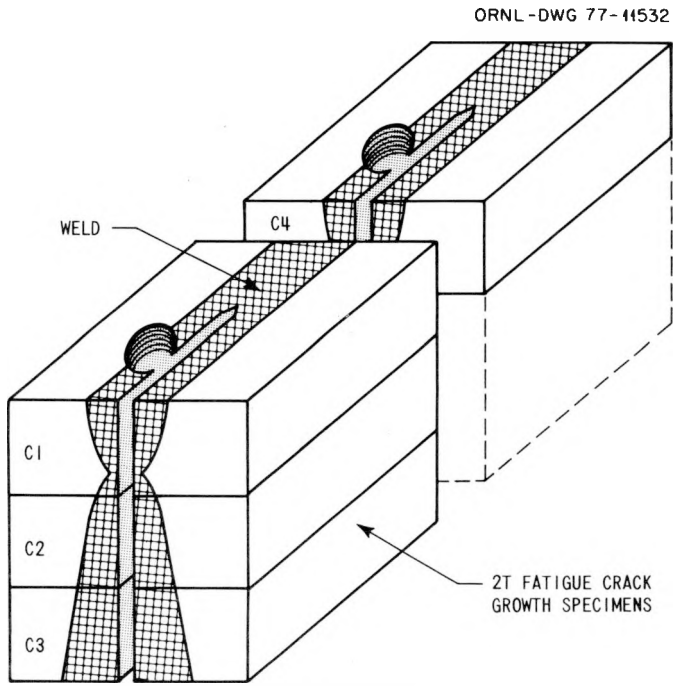

Fig. 3.6. Orientations of weldment specimens.

3.6 Fracture Surface Examination

Since the publication of HSST Technical Report 35, the majority of the specimens tested have produced visually smooth and regular fracture surfaces.[5] Earlier specimens displayed considerable macroscopic as well as microscopic crack branching.[5,6] Several recent specimens have also displayed crack branching and are worthy of discussion.

Unlike in the earlier tests, branching appears to be associated with the beach marks, which were produced several times during each test. (In more recent tests the number of beach marks has been minimized.) These marks are typically produced by increasing the test frequency to 10 cpm while maintaining the same loadings. The branching appears to originate at the beach marks, as seen in Fig. 3.7. Although macrobranching, as evidenced by visual appearance, is present in only a few specimens, all the specimens show some indications of microbranching, as seen in micrographs taken transverse to the fracture surface. In spite of the stress-corrosion-like appearance of these micro- and macrobranches, no evidence was found for other than fatigue-associated crack growth. The fracture surfaces of the macrobranches all contained a striated appearance similar to the main fracture surface. In fact, no evidence of crack propagation was found on any fracture surface other than transgranular fatigue crack growth, producing striations. An example of these striations for specimen F-1 is shown in Fig. 3.8.

When comparing the measured striation spacings with the macroscopic fatigue crack growth rates, excellent agreement was obtained in all cases, confirming again the absence of pure intergranular or cleavage type stress corrosion. This is limited to crack growth rates in excess of $\sim 5 \times 10^{-5}$ in./cycle, however, because below this rate the fine striations are destroyed by the oxidation of the fracture surface which takes place during the test.

The submerged arc weldments produced a fracture surface having a much different texture from the base metal specimens. Metallographic sections were prepared since it was suspected that this unusual surface had microstructural origins. As shown in Fig. 3.9, the microstructure is typical of A533B class 1 plate and A508 class 2 forging microstructures and contains no unusual features which would explain the abnormal fracture surface.

PHOTO 1742-77

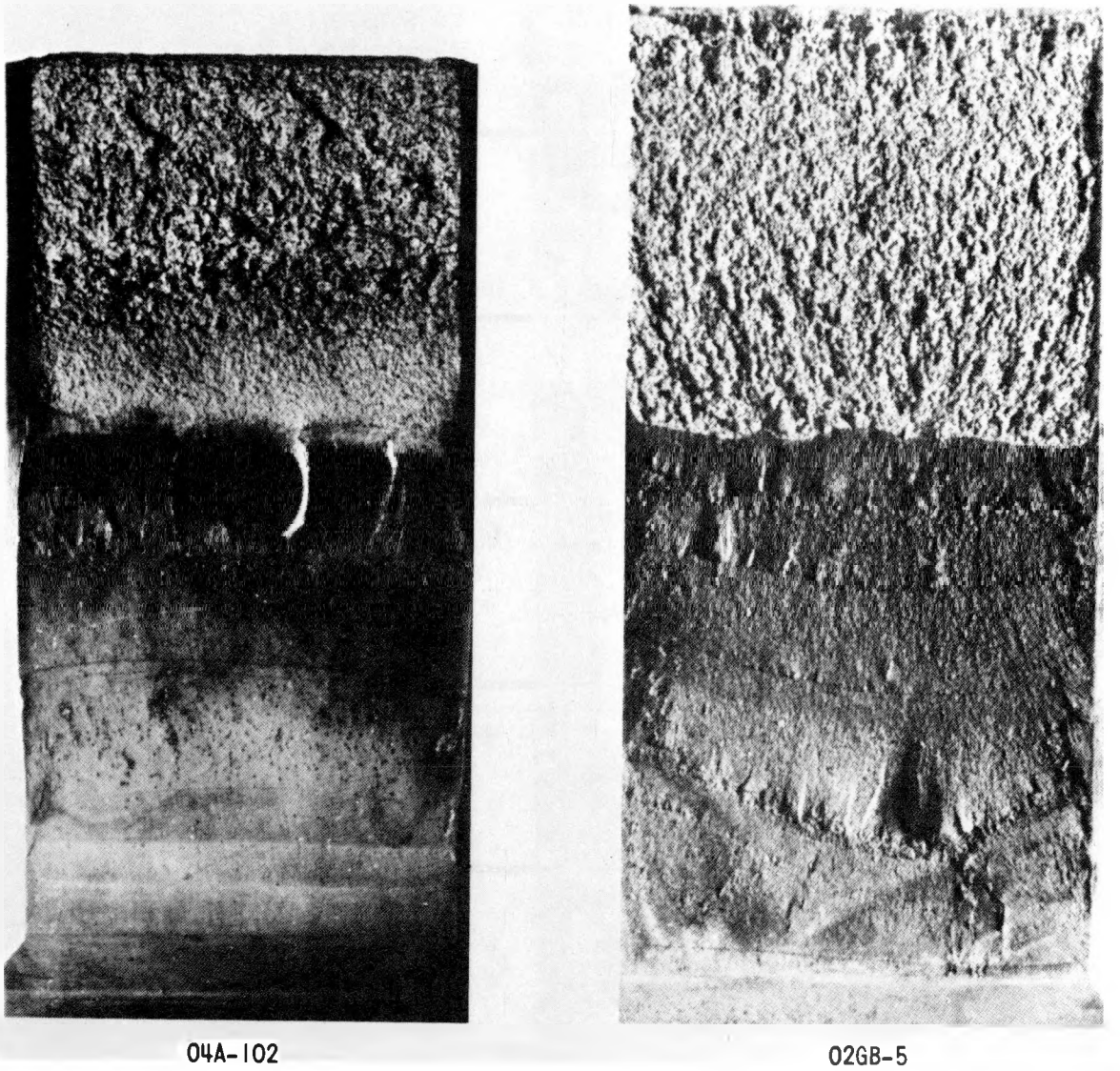

Fig. 3.7. Macrophotograph of fracture surfaces. Original reduced 6%.

Scanning electron micrographs of the weldment specimens indicate that the fatigue surfaces produced in the PWR environment are not typical; they contain a dimpled appearance usually seen in overload fractures, as shown in Figs. 3.10 and 3.11. Examination of the region where the crack was fatigued in air shows a similar fracture morphology. Comparison of Figs. 3.10 and 3.11 shows that these effects occur regardless of

PHOTO 1741-77

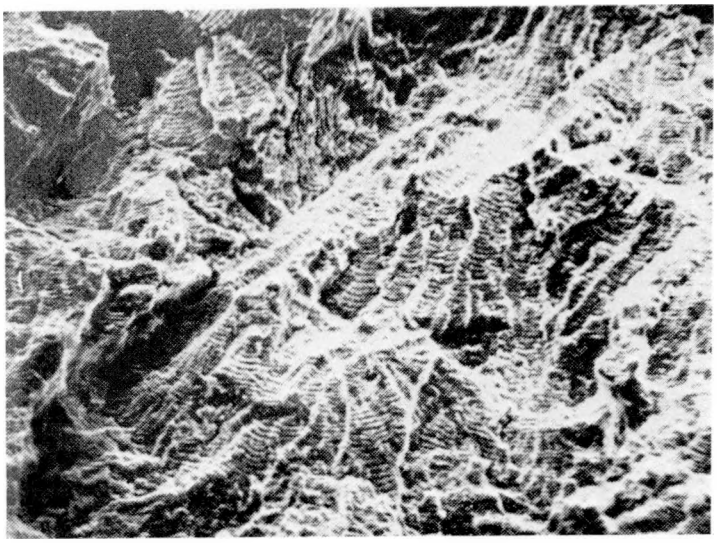

500X

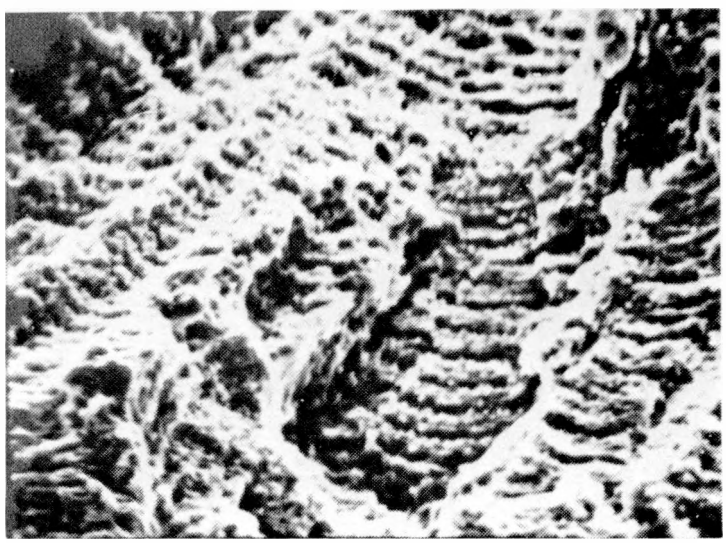

2000X

Fig. 3.8. Striations on fracture surface of specimen F-1 at ΔK = 30 $MN \cdot m^{-3/2}$ (27 ksi $\sqrt{in.}$).

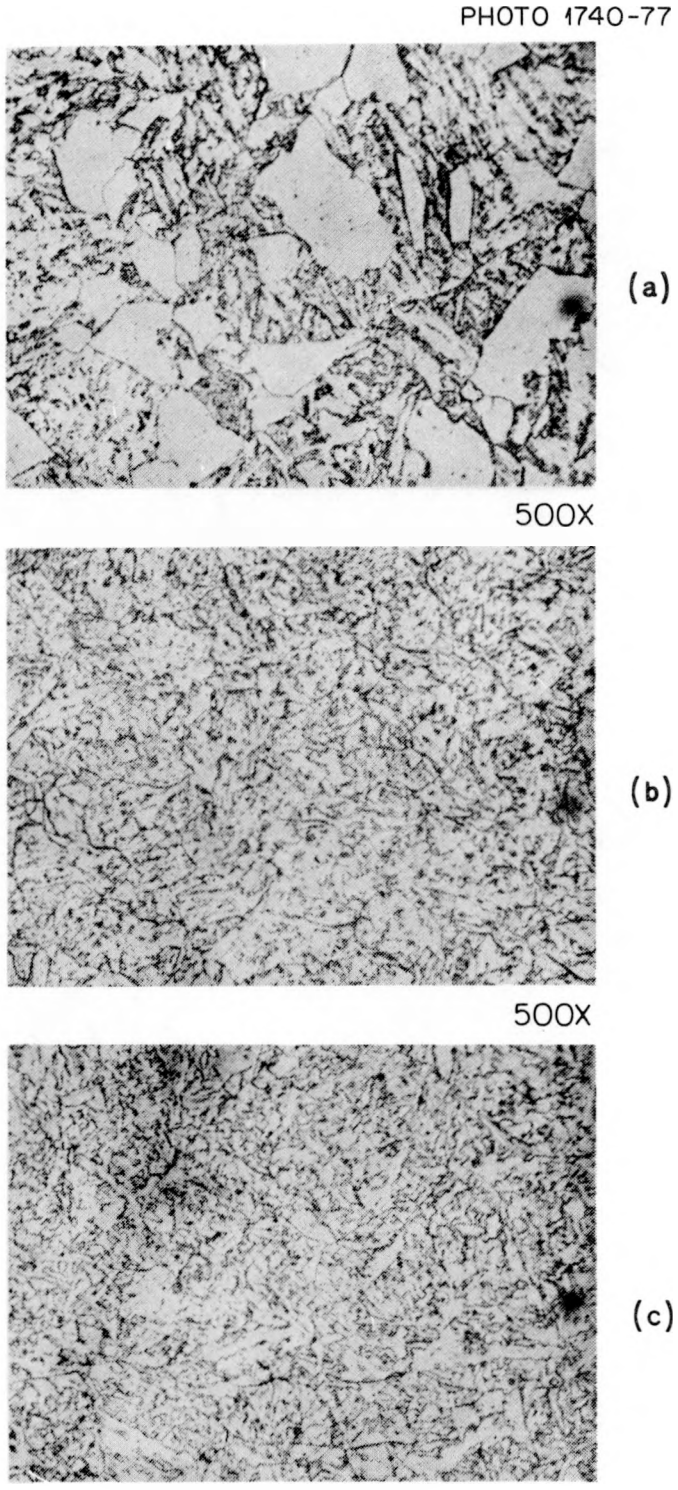

Fig. 3.9. Microstructural comparison of (a) A508 class 2, (b) A533 B class 1, and (c) submerged-arc weld in A533, grade B, class 1 steel. Micrographs reduced to 80% of original.

PHOTO 1739-77

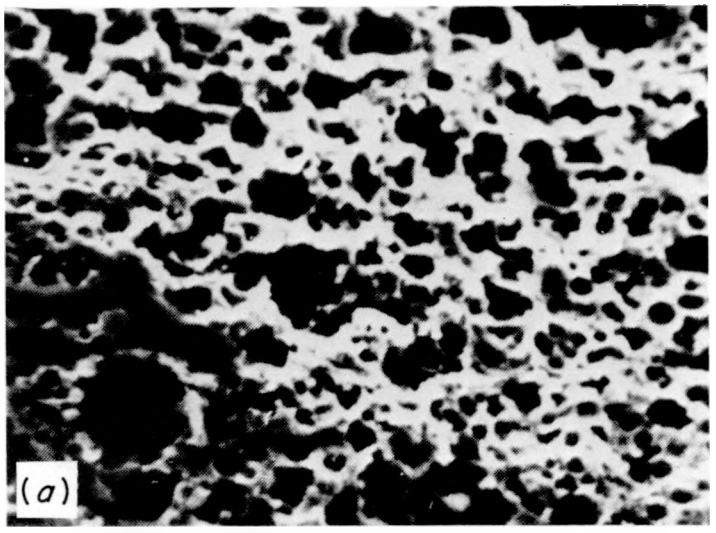

2000X

15.0 mm (0.59 in.) DISPLACEMENT OF MICROGRAPH FROM MACHINED NOTCH

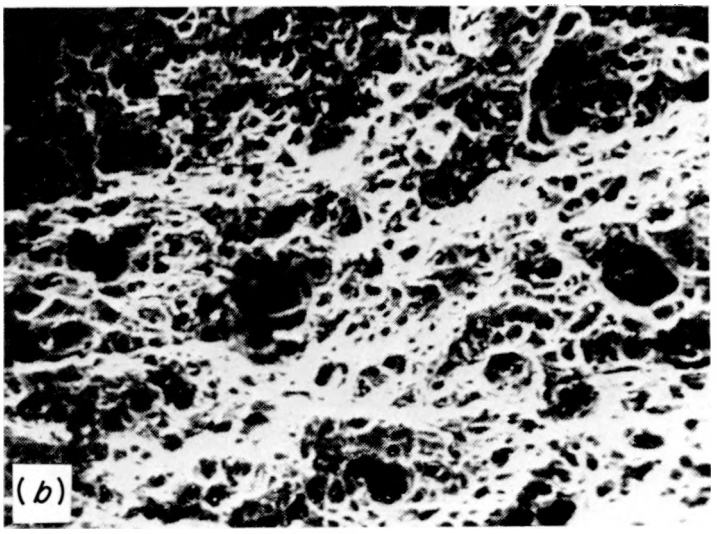

700X

50.0 mm (1.97 in.) DISPLACEMENT OF MICROGRAPH FROM MACHINED NOTCH

Fig. 3.10. Fracture surfaces of specimen C-1 (submerged arc weld) corresponding to fatigue crack growth in (a) water and (b) air. R = 0.7; test frequency = 1 cpm.

PHOTO 1738-77

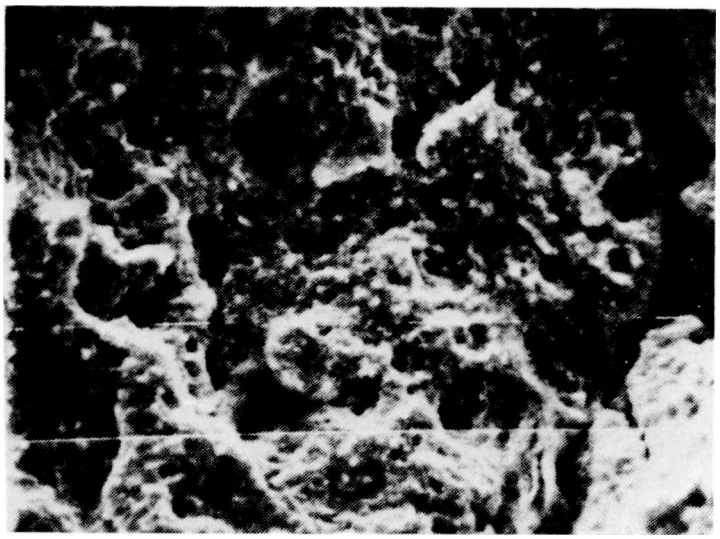

2000X

36.6 mm (1.44 in.) DISPLACEMENT OF MICROGRAPH FROM MACHINED NOTCH

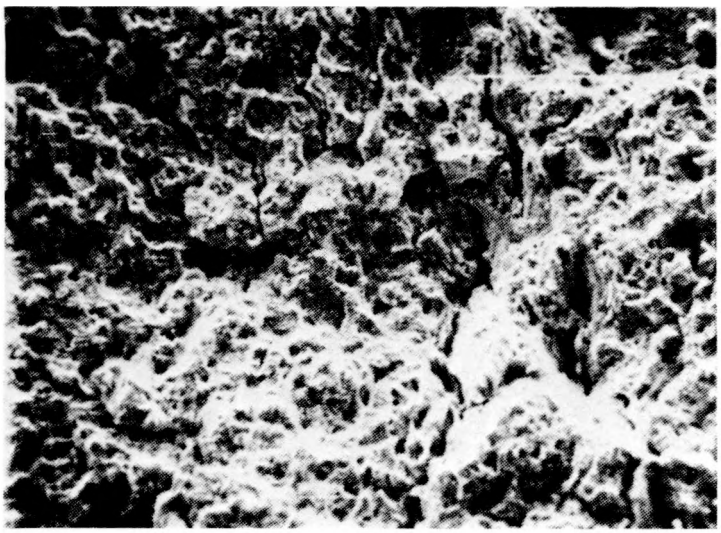

500X

36.6 mm (1.44 in.) DISPLACEMENT OF MICROGRAPH FROM MACHINED NOTCH

Fig. 3.11. Fracture surfaces of specimen C-2 (submerged arc weld) corresponding to fatigue crack growth in PWR water. R = 0.2; test frequency = 1 cpm.

the R ratio used in the test, but the high R-ratio specimen (C-1) shows more severe dimpling, possibly due to the higher loads imposed. Measurement of striations in the weld specimens was difficult because very few striations could be found (Figs. 3.10 and 3.11). Some limited striation measurements made on specimen C-2, however, again confirmed the calculated crack growth rates.

References

1. W. H. Bamford and K. V. Scott, "Effect of High-Temperature Primary Reactor Water on the Subcritical Crack Growth of Reactor Vessel Steel," *Heavy Section Steel Technology Program Quart. Prog. Rep. October–December 1976*, ORNL/NUREG/TM-94, pp. 9–17.

2. W. H. Bamford, K. V. Scott, and D. M. Moon, "Evaluation of Critical Factors in Fatigue Crack Growth Rate Studies of Reactor Vessel Steels," *Proceedings of the Fourth Water Reactor Safety Information Meeting, Gaithersburg, Md., September 1976.*

3. H. E. Watson, "Evaluation of Critical Factors in Fatigue Crack Growth Rate Studies of LWR Steels," *Proceedings of Fourth Water Reactor Safety Information Meeting, Gaithersburg, Md., September 1976.*

4. W. H. Bamford, "The Effect of Pressurized Water Reactor Environment on Fatigue Crack Propagation, Including Hold Times," *Proceedings of the Conference on the Effects of Environment on Fatigue*, Institution of Mechanical Engineers, May 1977.

5. T. R. Mager et al., *The Effect of Low Frequencies on the Fatigue Crack Growth Characteristics of A533B Class 1 Plate in an Environment of High Temperature Primary Grade Nuclear Reactor Water*, HSST Report 35 (December 1973).

6. T. R. Mager, D. M. Moon, and J. D. Landes, "Fatigue Crack Growth Characteristics of A533B Grade B Class 1 Plate in an Environment of High Temperature Primary Grade Nuclear Reactor Water," ASME Paper 76-PVP-3, September 1976.

4. INVESTIGATIONS OF IRRADIATED MATERIALS

4.1 Toughness Investigations of Irradiated Materials

R. G. Berggren T. N. Jones D. A. Canonico

Irradiation of the three capsules containing submerged-arc weldments was completed March 23, 1977, with a total irradiation time of 2397 hr with the reactor at 2 MW. Total irradiation time at lower power levels was less than 0.5% of that at 2 MW. The capsules were exposed in the initial orientation for 32% of the time, exposed rotated 180° for 50% of the time, and rotated back to the original orientation for the remaining 18% of the time. The total fluence in the capsules is symmetrical about the center plane (i.e., the midplane of the 4T-CT specimens). The schedule for the irradiation was based on a fast-neutron flux estimate obtained from a preliminary (dummy capsule) irradiation. Additional flux measurements made with the dummy capsule and analyzed during January and February indicated that the earlier flux estimate was about 50% too low. The irradiation schedule was immediately revised to provide a symmetrical fluence at the lowest possible total fluence. The estimated fast-neutron fluences at the crack tips of the 4T compact tension specimens, given in Table 4.1, are based on results from the two dummy capsule experiments. These fluences are higher than the target fluence of 8×10^{18} neutrons/cm^2 ($E > 1$ MeV) but, based on information in Regulatory Guide 1.99, should result in only a small difference [$\sim$8 to 16 K ($\sim$15 to 30°F) increase] in the transition temperature shift and a small ($\sim$2 to 4%) difference in the decrease in shelf energy. Final fluence values will be obtained when the dosimeters in the specimen capsules are analyzed.

After storage in the BSR pool for about one month to permit decay of the shorter half-life activities, the capsules will be disassembled and Charpy impact tests conducted. The hot-cell Charpy testing facilities have been overhauled, tested, and calibrated in preparation for these tests. Design changes are complete and most parts and specimens are now on hand for the next set of irradiation capsules.

Table 4.1. Estimated fast-neutron fluences[a] at fatigue crack tip of 4T compact tension specimens

	Fluence (neutrons/cm^2, E > 1 MeV)	
	Center of crack	1 in. from surfaces
Weld 61W		
Top specimen	9.4×10^{18}	1.03×10^{19}
Bottom specimen	1.30×10^{19}	1.53×10^{19}
Weld 62W		
Top specimen	1.33×10^{19}	1.43×10^{19}
Bottom specimen	1.86×10^{19}	2.00×10^{19}
Weld 63W		
Top specimen	9.7×10^{18}	1.05×10^{19}
Bottom specimen	1.35×10^{19}	1.49×10^{19}

[a]Based on dosimeter results from "dummy" capsule irradiations.

4.2 Development of Unloading Compliance Method for Testing Irradiated Specimens*

J. A. Williams†

The degree to which small specimens can be employed to assess ductile fracture toughness is of concern in evaluating the properties of irradiated steels in reactor pressure vessels. The available data do not clearly establish the capability of small specimens to predict large structure behavior, and test criteria are in a state of flux. Additional data involving size, geometry, and material as variables are required to determine the validity of elastic-plastic fracture toughness analysis.

*Research performed under Purchase Order 11Y-50917V for the Oak Ridge National Laboratory, operated by Union Carbide Corporation under contract to the U.S. Energy Research and Development Administration.

†Hanford Engineering Development Laboratory.

The HSST program at ORNL has undertaken the task of irradiating 4-in.-thick compact specimens as well as a host of complementary size specimens; however, the preferred method, a single-specimen J_{Ic} fracture test, has not yet been established within the ductile fracture test criteria. Considering the cost and limited number of large irradiated specimens, additional development is planned in listing techniques to assure attainment of project objectives. Since a limited number of large irradiated specimens will be available, it was determined that the best procedures should be merged into the technique development at HEDL.

NRC, ORNL, NRL, and HEDL established a program objective to obtain the ductile fracture toughness property, J_{Ic}, from the R curve by use of the unloading compliance method and to confirm that the toughness so measured meets acceptable test criteria by multiple specimen techniques (heat tint). Using this method, curves for K_{Ic}, K_{Icd}, and K_{Jc} can be obtained as a function of temperature with increasing size specimens to determine a basis for prediction of test needs of large irradiated vessels. Additionally, initiation detection by the load-drop technique and acoustic-emission monitoring would be incorporated into the experimental program as "piggy back" test methods. It was agreed that a material having a C_V upper-shelf energy of $\sim$68 J (50 ft-lb) and a yield strength of $\sim$620 MPa (90 ksi) would be most appropriate for the development study since they would correspond to the expected properties of the irradiated materials.

The unloading compliance method (UCM) as a single-specimen J_{Ic} technique is currently receiving considerable attention for use in ductile fracture toughness material property assessment. The general approach to UCM testing to be used at HEDL was established by a survey of investigators currently involved in technique development.[1] UCM test and analysis techniques at this time should be considered developmental. Work is being done to improve techniques, and interpretive methods are not yet well defined (in terms of expected or proposed standards), but a specific method could be described for standardization. The method requires no special electronics or extensive specimen calibrations beyond a compliance analysis.

Reduction of loading and extensometer hysteresis was identified as the principal experimental objective in development of UCM techniques since the relative contribution of loading and extensometer hysteresis is not clearly defined. Investigators are moving toward bearing type designs for specimen grips. Compact tension (CT) specimen pinholes are being machined on larger centers to provide for bearings to be inserted into the grips. However, specimens already machined, particularly those already irradiated, represent special design problems for incorporation of bearings into grips which must be used on CT specimens with standard hold spacings. HEDL will attempt to develop bearing grips for use with the standard CT hold spacings of irradiated specimens. ASTM flat bottom hole grips will be alternative types of grips.

Hysteresis in displacement measurements is believed to be primarily a result of poor clip gage seating and dullness of the machined centerline-of-load edges. The current tendency is toward use of knife edges attached in the notch at the centerline of loading; it is believed this may provide a solution to the displacement hysteresis observed in clip gages. Specimens already machined and irradiated may require a unique approach or modification. HEDL has developed a load line displacement gage using dual LVDTs; the designs will be adapted for use with specimen sizes of this program.

Real time test analysis of unloading compliance is considered to be the most desirable approach; real time test analysis will be used at HEDL contingent upon obtaining necessary equipment. Obvious advantages are (1) test judgment can be exercised during the test; (2) the quality of the test can be determined at the onset and during the course of the test; and (3) data storage allows for ready access and reanalysis at a future date. As an alternative to real time computer techniques, data storage and post-test computer analysis will be used. Real time analysis is particularly important when large specimens with low crack extension resolution require judgment as to where a test should be terminated at very short crack extensions. In light of the obvious advantages of real time or posttest computer processing, X-Y chart recording will be used as a redundant recording technique and as an on-line visual record of test progress.

Indications are that the resolution of compliance of UCM appears to decrease with increasing specimen size. Sensitivity increases with crack depth. Based on the uncertainty of measured compliance, the sensitivity with which change in crack length can be determined for a 4T CT specimen is around ±0.010 and is ±0.002 for a 0.5T CT specimen. A four-point bend bar yielded approximately ±0.001 in. sensitivity when using load line displacement as compared to approximately ±0.005 in. by crack opening measurements. Values for a/w are 0.6 to 0.7. Irregularities in crack front may cause considerable interpretive problems and contribute to large errors. No current ASTM recommendations relate to interpretation of crack front irregularities; such behavior might be expected in weld materials, and interpretive significance will eventually have to be determined. Absolute accuracies of compliance are said to correlate well with tentatively recommended nine-point crack front measurements, which will be used to confirm UCM determinations.

It is anticipated that the test program will contribute to advancing ductile fracture toughness assessment by supplying additional information about specimen size requirements and allowable crack extension in the development of R curves for measurement of the critical J integral. HEDL interacted in current ASTM deliberations on criteria relative to these points, and it was suggested that additional data will be required to verify their validity.

Reference

1. Private communications of J. A. Williams (HEDL) and F. J. Loss (NRL) with various investigators.

5. PRESSURE VESSEL INVESTIGATIONS

5.1 Preparations for HSST Intermediate Vessel Tests V-7B and V-8

P. P. Holz

Westinghouse Electric Corporation, Tampa Division (WTD), completed the half-bead weld repair of intermediate test vessels V-7B and V-8 in accordance with specifications based upon Section XI of the ASME Boiler and Pressure Vessel Code.[1] The cylindrical prolongation of V-8 was used as a welding procedure qualification piece for the two types of cavities in V-7B and V-8. WTD work also included the preparation of half-bead weld tensile specimen stock and practice blocks for electron-beam flawing studies. The vessels and prolongation at Tampa were instrumented by T. A. King of ORNL for measurement of strain changes. C. E. Childress was the ORNL quality assurance inspector.

The vessels and the prolongation were inspected as outlined in the code. Magnetic particle inspections were limited to alternate pass inspections following the first three layer deposits. In addition, GARD, Inc., a subsidiary of GATX Corporation of Niles, Illinois, monitored acoustic emission during the repair on vessel V-7B. A few acoustic discords were noted, confirming defects which were subsequently found in the specified magnetic particle examinations. Defects were attributed either to weld starts and stops or to excessive heat while attempting to use 4.0-mm-diam (0.15625-in.) rods in vertical runs. Noted defects were always ground out at once. WTD discontinued use of these electrodes and thereafter used 3.2-mm (0.125-in.) electrodes exclusively beyond the half-bead layer deposited with 2.4-mm-diam (0.09375-in.) electrodes.

Severe porosity effects were observed when the backing bars were removed from the interiors of the through-wall repairs in V-7B and the prolongation. The initial layer deposited on the backing bars was not subjected to half-bead grinding, since the bars were to be removed. The defects were shallow and easily ground out with the remaining wall thickness well within code-specified dimensional requirements. Visual and magnetic particle examinations also revealed porosity at the intersection

of the inside surface of vessel V-7B and the lower slope of the repair cavity (i.e., the end toward the open end of the vessel). A volume about 127 mm wide × 25 mm high × 22 mm deep (5 × 1 × 0.875 in.) was ground out and repaired from the inside following code-specified half-bead technique requirements. Preheat was supplied from the outside so that the hot vessel could be entered for the repair welding. Porosity was also observed in final x-ray and ultrasonic examinations. Triangulation shots resolved the porosity as being distributed in various layers rather than conglomerated. Nondestructive testing indicated that the vessels and prolongation were acceptable in accordance with the code.

After welding and nondestructive examination were completed by WTD, the vessels, prolongation, tensile specimen stock, and weld test blocks were returned to ORNL for further work.

The prolongation was sawed into two cylinders as shown in Fig. 5.1. Thirty strain gages were attached to the prolongation prior to cutting, and measurement of strain changes resulting from the sectioning will be used for adjusting residual stresses measured after cutting. The upper half of the prolongation was left intact for residual stress measurement; the lower half was cut as shown in Fig. 5.1 for use in material characterization and for detailed metallographic examination.

Two beam saddle supports were welded to vessel V-7B to index and align it for milling the flaw slot and for electron-beam (EB) flaw-welding operations. The flaw design[2] in vessel V-7B is the same as that in V-7 and V-7A. A large horizontal boring mill was again used for milling a 25-mm-wide (1-in.) trapezoidal slot to a 127-mm (5-in.) maximum depth at one side of the weld repair.[1] Thus the longitudinal center of the V-7B flaw is located 7.5° counterclockwise from the center of the V-7A flaw as the vessel is viewed from its open (flanged) end. Various etching solutions were used in the machining operations to locate drill and mill centers so that the slot would be centered about the heat-affected zone (HAZ) of the repair weld. Position checks and appropriate minor tool centering adjustments were made using 9.5- and 12.7-mm-diam (0.375- and 0.5-in.) cutters at depths of 12.7, 25.4, and 63.5 mm (0.5, 1.0, and 2.5 in.) from the surface. The centers of the heat-affected zone and the finished slot are within 0.25 to 0.89 mm (0.010 to 0.035 in.), both along

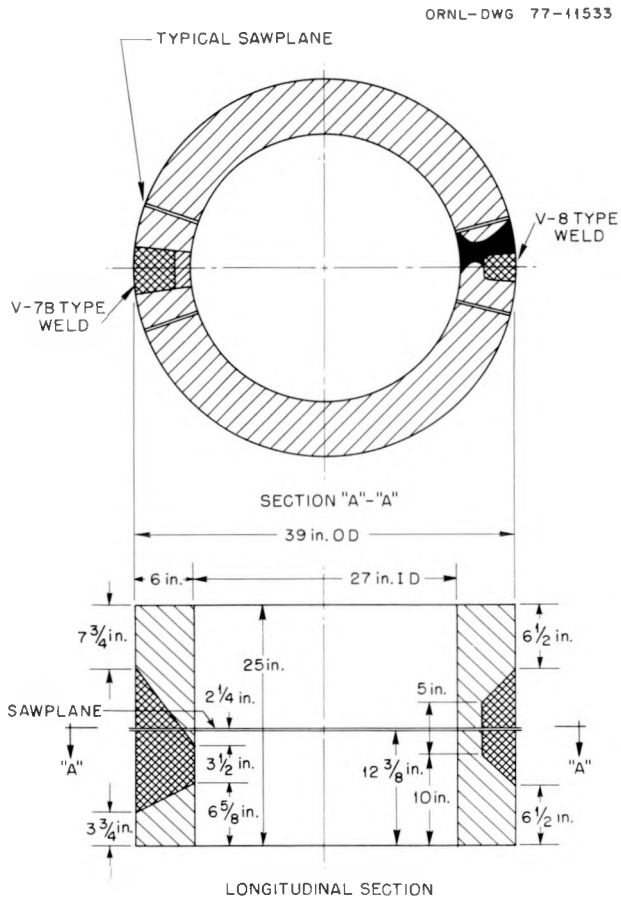

Fig. 5.1. Sawcut layout of prolongation V-8.

the slopes and at the bottom of the trapezoid. The HAZ band width varies from 1.7 to 2.0 mm (0.065 to 0.080 in.). Ten strain gages were attached to the inner surface below the slot to monitor stress changes induced by the machining operations.

Four 50-mm-thick (2-in.) brick-shaped A533 material test blocks with premachined cavities to simulate the vessel cavity geometry were also "repair welded" by WTD to half-bead technique welding standards. These blocks have been ground and etched and will be used to establish EB programming input, to test magnetic beam deflection effects, and to verify hydrogen-charge flawing methods and acoustic-emission crack detection calibrations. A steel model of a trapezoidal notch is also available for final slope programming checkouts.

Electron-beam welding along the bottom of the machined notch in V-7A was complicated by the residual magnetism of the vessel.[3] Gaussmeter checks within the slot of vessel V-7B revealed nonuniform magnetic flux densities, with the highest readings 8×10^{-4} T (8 G) longitudinally and 5×10^{-4} T (5 G) transversely. These readings are about one-tenth the magnitude of the magnetic flux densities encountered with the V-7A repair weld. Planned symmetry for two electrical grounding connections, each located 90° from the longitudinal repair cavity walls and centered about the longitudinal axis of the cavity, may have been effective in minimizing the magnetization of the steel vessel resulting from the stick electrode dc-arc repair weld. An arbitrarily located single ground takeoff was used for V-7A repairs. Two ceramic 0.1-T (1000-G) permamagnets are being machined by electrical discharge to fit within the trapezoidal slot. These magnets should permit flux trimming by varied magnet orientations and locations to further reduce and even out the flux distribution along the EB traverse so as to keep the beam centered within the desired zone. Attemps will be made to trim the flux from 6×10^{-4} to 3×10^{-4} T (6 to 3 G) in order to place the EB weld bead within the vicinity of the heat-affected zone of the repair weld. Practice trials indicate that EB bead positioning can be controlled in fields up to $\sim 3 \times 10^{-4}$ T (3 G).

5.2 Weld Repair of Intermediate Test Vessel V-7B*

S. W. Wismer†

The half-bead temper welding technique was used to repair intermediate test vessels V-7B and V-8 and a cylindrical prolongation of the V-8 test section. The welding and nondestructive examination were performed by WTD. The welding program was similar to that used by Combustion Engineering in the previous repair of vessel V-7.[4] The difference between

*Work performed under Purchase Order 75Y-13494V for ORNL, operated by Union Carbide Corporation under contract to the U.S. Energy Research and Development Administration.

†Westinghouse Electric Corporation, Tampa Division.

the two programs was the position of the vessel; all welding at WTD was done with the axes of the cylinders (and the long axes of the cavities) vertical.

Arc air gouging, followed by grinding, was used for the V-7B-type cavity preparation in the prolongation and for finishing the ends of the cavity in vessel V-7B. These through-wall cavities were designed for additional destructive testing of the heat-affected zone at ORNL. The steep wall preparation specified by ORNL was not the best design for welder access at the root, and visual examination revealed porosity when the backing strip was removed. Figures 5.2 and 5.3 show vessels V-7B and V-8 prior to welding.* All pre- and postweld heating was done with resistance equipment by Cooperheat.

Two recommendations are made: (1) if field repairs of operating vessels are deeper than ∿75 mm (3 in.), a greater angle should be required on the cavity sides to improve welder access; (2) there are variations between the ASME Section III, NB-4640, and Section XI, IWB-4420, regarding the half-bead temper technique. After final testing of the vessels at ORNL, ASME should be requested to consider standardization of these welding techniques in both Sections III and XI.

5.3 Characterization of the V-7B and V-8 Repair Weldments

W. J. Stelzman D. A. Canonico

We are preparing to characterize a half-bead weld qualification test plate and prototype V-7B and V-8 half-bead repair weldments made in the intermediate test vessel V-8 prolongation (Fig. 5.1). All welding was done in the vertical position, from bottom to top. A postweld heat treatment of 232 to 288°C (450 to 550°F) followed the completion of each weldment. Figure 5.4 shows a cross section of the 41.3-mm-thick (1.625-in.) weld qualification test plate, 01MS-C1. Cross sections transverse to the long axis of the welds in prototype V-7B and V-8

*Photographs in this section were provided by Westinghouse Electric Corporation, Tampa Division.

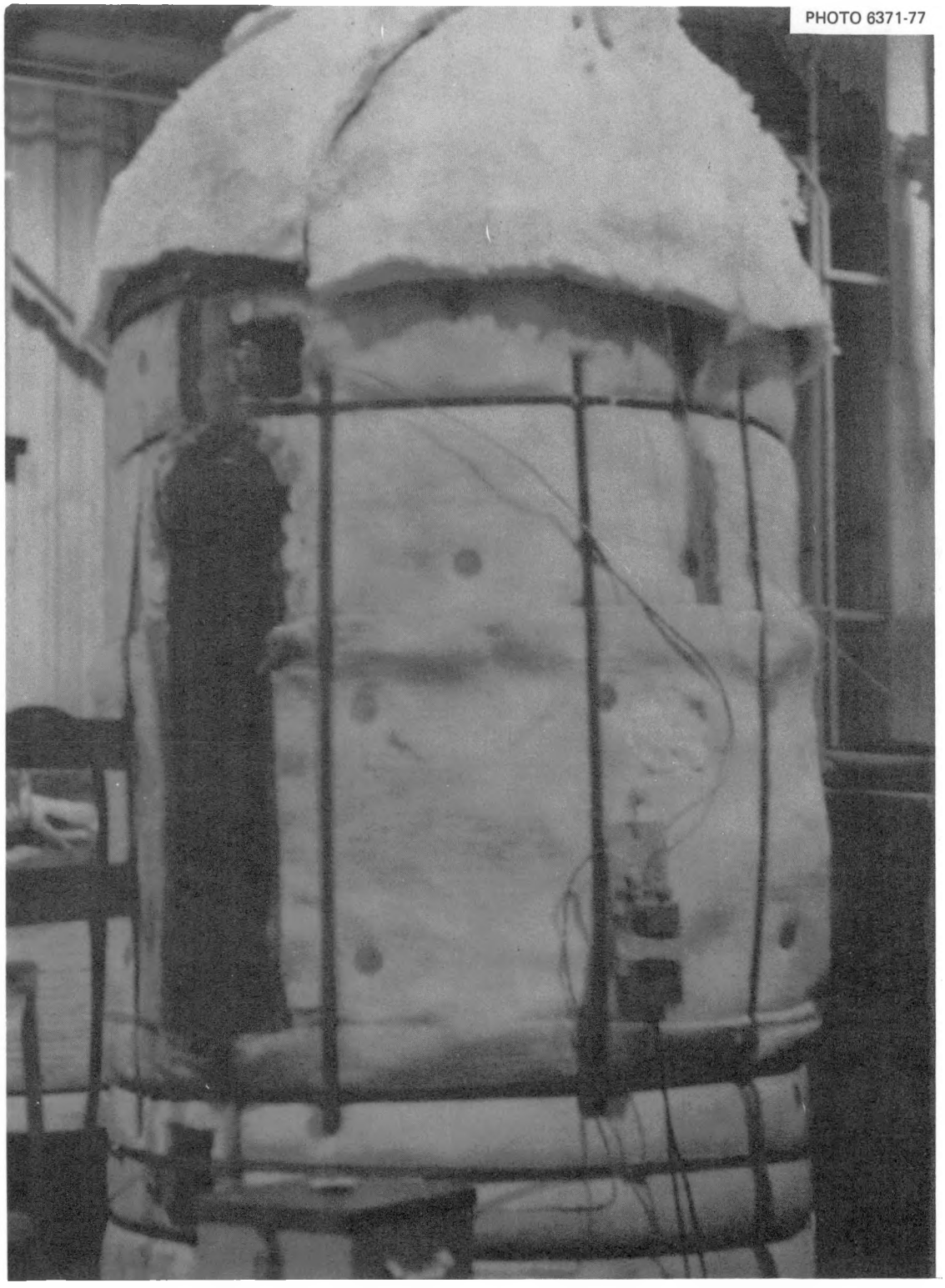

Fig. 5.2. Vessel V-7B prepared for welding.

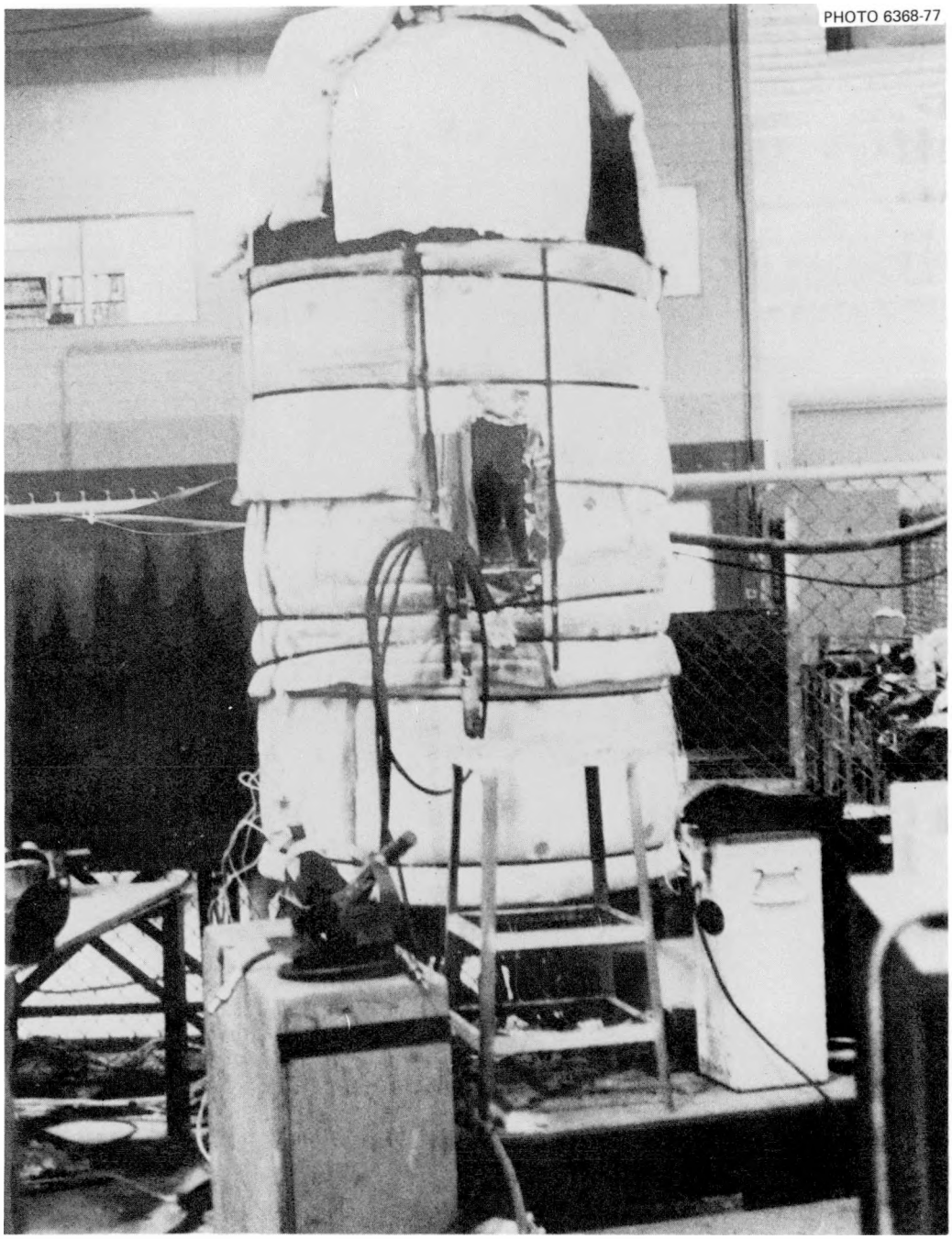

Fig. 5.3. Vessel V-8 prepared for welding.

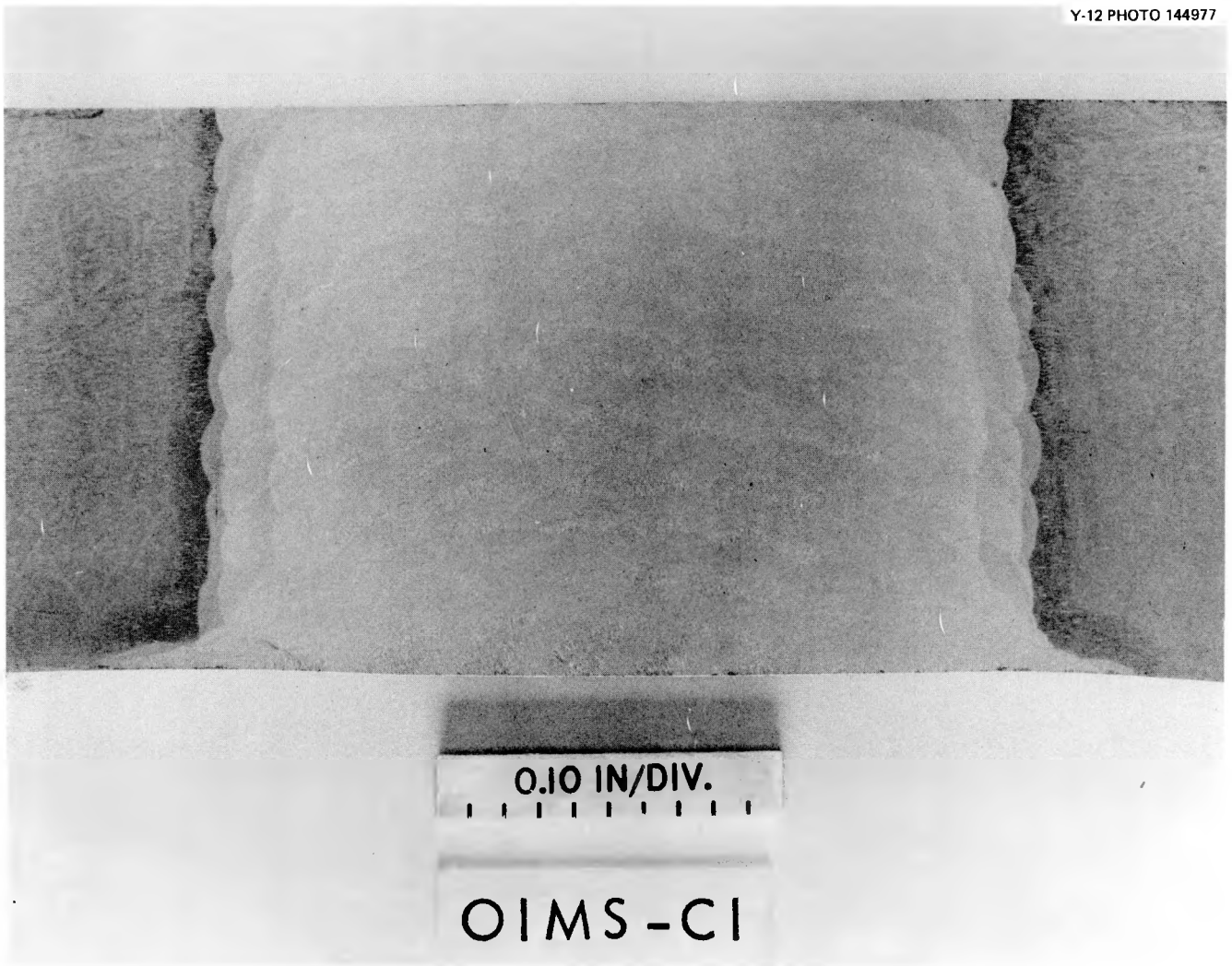

Fig. 5.4. Cross section of the half-bead-technique weldment in test plate 01MS-C1.

repair weldments made in the V-8 prolongation are shown in Figs. 5.5 and 5.6, respectively. All three weldments are being sectioned to obtain HAZ, weld metal, and base metal specimens. Preliminary testing has begun.

5.4 V-7C Crack-Arrest Model Tests

G. C. Smith P. P. Holz

Two small pressure vessel models were tested during the reporting period. The objective was to investigate the feasibility of crack-arrest test involving an intermediate vessel. Although the model tests were successfully completed, the feasibility question remains open until further models can be tested. However, the first two tests did indicate that pressure vessels containing flawed, low-upper-shelf material [e.g., defined by Charpy-V impact energies of 41 J or less (30 ft-lb)] can be highly resistant to catastrophic failure.

5.4.1 Model configuration

The configuration of the tested models is shown schematically in Fig. 5.7. The models consisted of five cylindrical sections (including the two flat-head caps) that were joined by EB welding. The wall thicknesses and diameters of the three central sections were chosen so that the models were approximately 1/4-scale representations of a typical intermediate test vessel; the wall thickness of the models was 38.1 mm (1.5 in.) and the outside diameter of the models was 254.0 mm (10.0 in.).

Axial slots were machined near the center of the models and an electron beam was passed along the periphery of the slot so as to create a sharp flaw. Figure 5.8 is a schematic of the flaw that existed in the first two models. The purpose of the stainless steel liner shown in Fig. 5.7 was to prevent the escape of pressurizing fluid through the flaw.

The modular approach to fabricating the models facilitated the inclusion of a well-defined, brittle starter section (i.e., the centermost cylinder) and the reuse of model components. A preliminary analysis and discussion of the configuration is contained in a previous progress report.

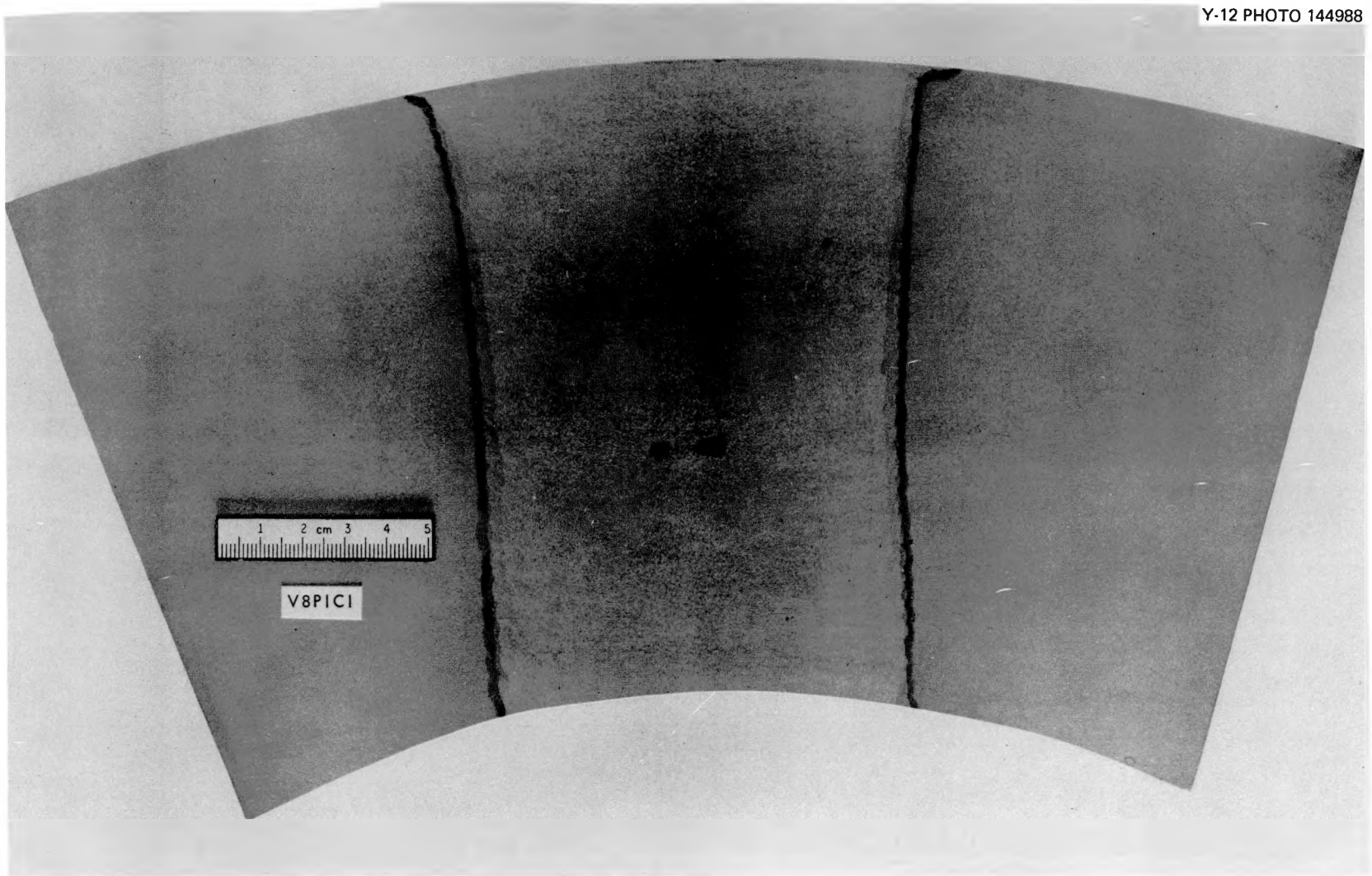

Fig. 5.5. Cross section of the prototype half-bead-technique weld repair to be used in intermediate test vessel V-7B. Section from V-8 prolongation.

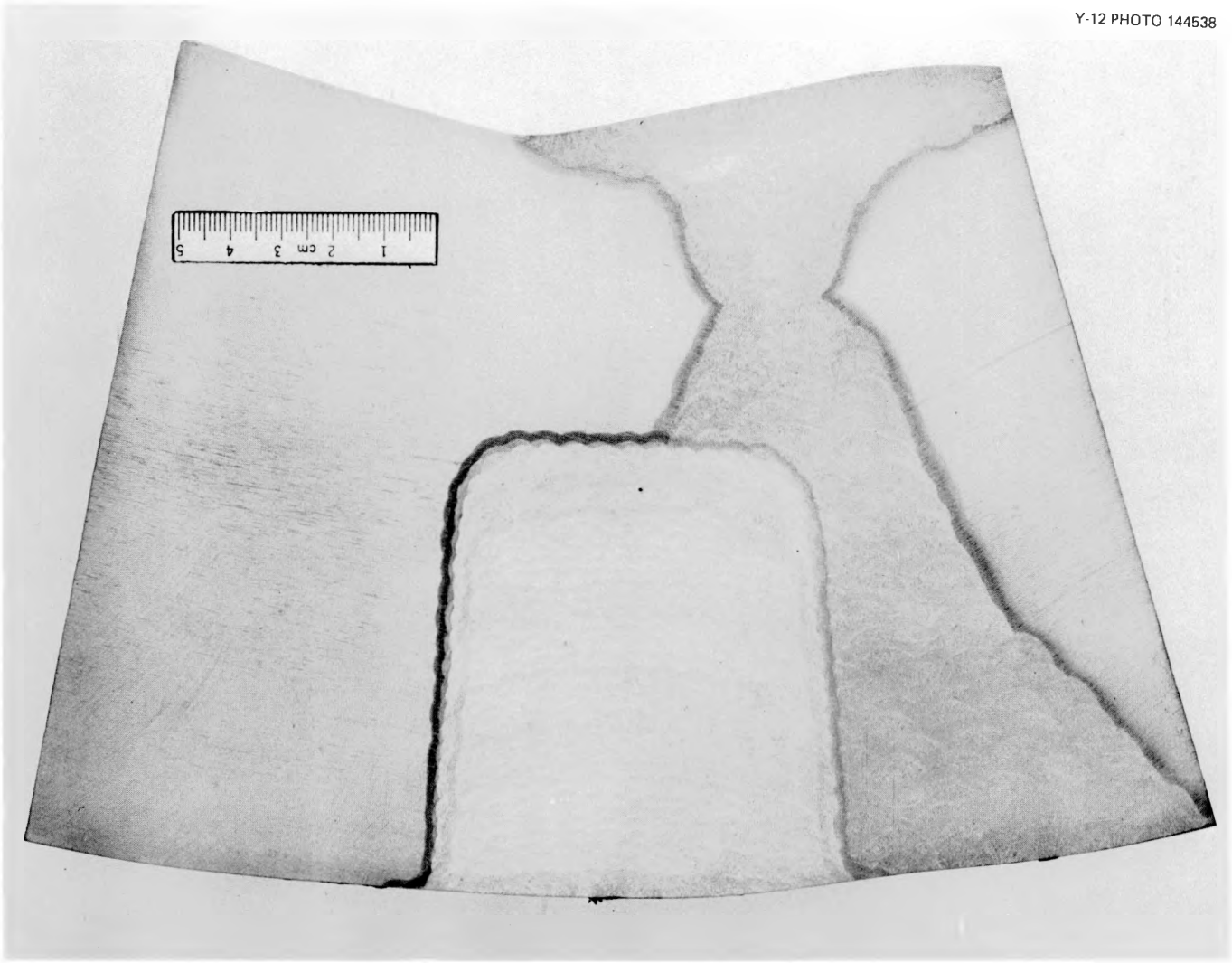

Fig. 5.6. Cross section of the prototype half-bead-technique weld repair to be used in intermediate test vessel V-8. Section from V-8 prolongation.

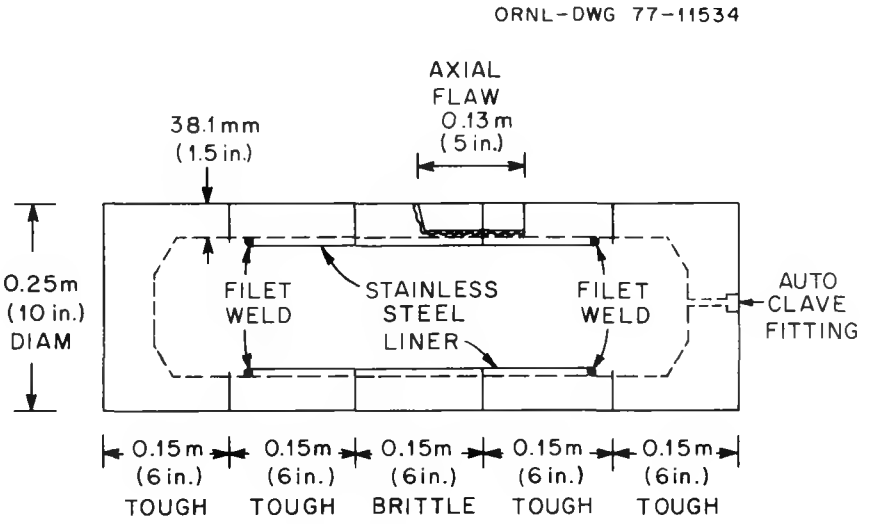

Fig. 5.7. Cross section of the crack-arrest model configuration. The center section was quenched only A533 (plate 03); the other four sections were quenched and tempered A533 (plate 57).

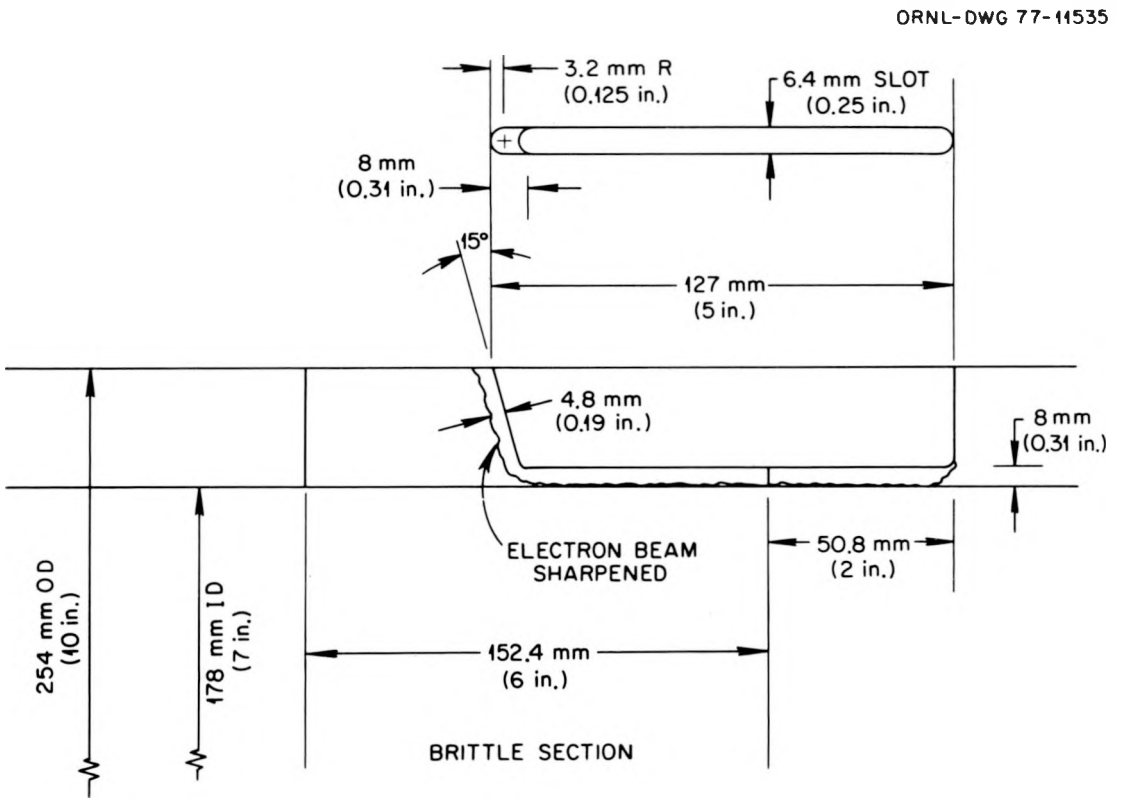

Fig. 5.8. Schematic of the machined slot and electron-beam-sharpened flaw in the first and second crack-arrest models.

5.4.2 Material selection and data

Since intermediate vessel V-7 is currently the candidate for a crack-arrest demonstration, it followed that A533, grade B, class 1 material should be used in the section where the crack was to arrest. Crack-arrest toughnesses for this material have been reported by Battelle Columbus Laboratories[6] ($K_{ID_{min}}$) and Material Research Laboratory, Inc.[7] (K_{Ia}).

Selection of the brittle insert material for the crack-arrest models was based on precracked Charpy-V slow-bend test data (K_{Icd}) for quenched-only A533 (HSST plate 04) that had been generated for HSST thermal shock work.[8] A comparison of K_{Icd} values with the reported $K_{ID_{min}}$ and K_{Ia} values indicated reasonable prospects for successful crack-arrest model tests.

HSST plate 57 had the requisite composition and heat treatments for the tough sections of the models and was available in sufficient quantity for the anticipated model testing.[9] For similar reasons HSST plate 03 was selected for the brittle sections.[10] Material properties of plate 57 and quenched-only plate 03, reported in previous progress reports,[11,12] are summarized here. Charpy-V impact energies and static fracture toughness data from precracked Charpy-V specimens are shown in Figs. 5.9 and 5.10. The machined and sharpened flaws in the model vessels were oriented such that the data for RT-oriented specimens shown in Figs. 5.9 and 5.10 obtain. The drop-weight nil-ductility temperature for plate 57 material is −23°C (−10°F) and the yield stress for plate 57 is 434 MPa (63 ksi) and 1083 MPa (157 ksi) for quenched-only plate 03.

5.4.3 Crack-arrest model fabrication

The crack-arrest model fabrication and assembly involved multitask operations. Cylinders and caps were machined from HSST plate 57 and cylinders from HSST plate 03. The axes of the cylinders were normal to the surfaces of the 152-mm-thick (6-in.) plates. The cylinders were stenciled so that the original plate roll direction could be referenced for subsequent crack orientation. The plate 03 cylinders were reaustenitized for 1.5 hr at 872°C (1602°F) and water quenched. Two cylinders of

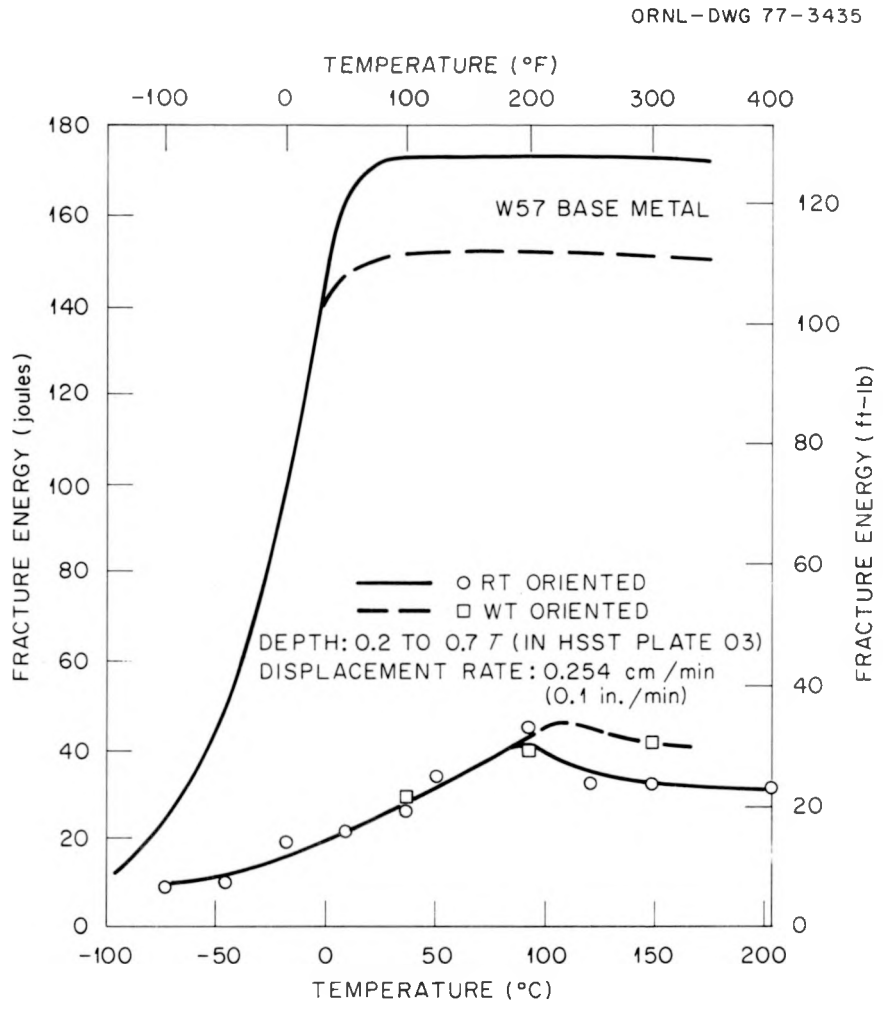

Fig. 5.9. Variation of Charpy-V impact energy with temperature for 44-mm-thick (1 3/4-in.) through-thickness slices from plate section 03JZ after reaustenitizing for 1.5 hr and water quenching. The specimens from AQ03 were all removed from either the 1/3 or 2/3T location in the 44-mm characterization sections.

plate 57 material were then fitted to the ends of a cylinder of 03 material by means of copper alignment and chill rings, placed into a supporting lathe, and EB butt-welded into a subassembly. Practice EB welds on low and high toughness plate stock were used to develop the welding parameters.[11] Electron-beam welds were not postweld tempered or stress relieved, and EB welds of prototypical components of the models were x-ray tested and found to be acceptable full-penetration joints.

The full-penetration welds were made on the cylinders with the EB potential set at 50 kV and beam current at 201 mA with a welding speed of

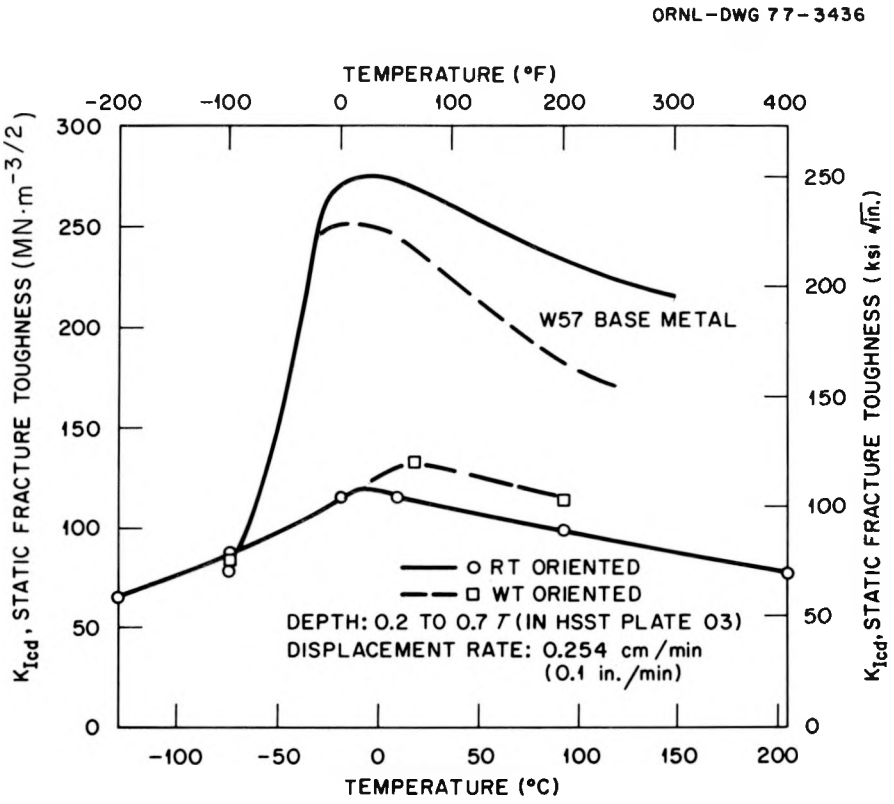

Fig. 5.10. Variation of static fracture toughness with temperature from precracked Charpy-V specimens from 44-mm-thick (1 3/4-in.) through-thickness slices from plate section 03JZ after reaustenitizing for 1.5 hr at 872°C (1602°F) and water quenching.

152 mm/min (6 in./min). Focusing current was set at 25 mA above that for which sharp focus was obtained on the outside surface. The lathe shown in Fig. 5.11 rotated the cylinders under the stationary EB gun, which was mounted to emit electrons vertically down onto the horizontal cylinder joints. The special lathe included aluminum head and tail stock pieces to accommodate the cylinders and/or end caps. End stock restraints included set screws for concentricity alignment and were provided with end hole cutouts to permit the evacuation of specimen interiors while the chamber atmosphere was lowered prior to welding. Attachments to these end holders also supported tungsten target stock for beam emission starters and for sharp weld focus checkouts. The cylindrical specimen components were preset by an indicator for runouts not to exceed 0.76 mm (0.030 in.).

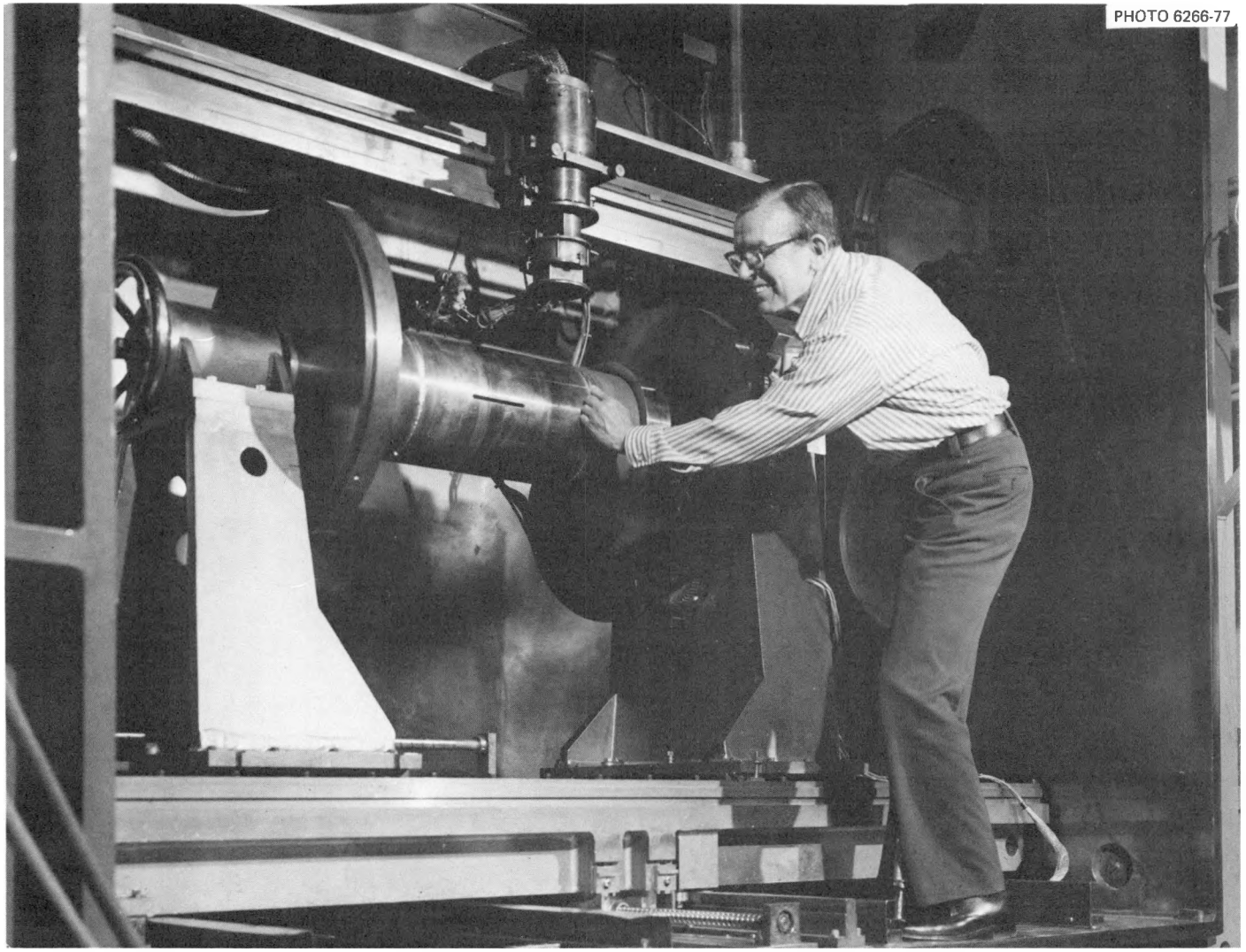

Fig. 5.11. Crack-arrest model in lathe in electron-beam weld chamber.

A highly defocused beam (focusing current set 25 mA above that required to obtain a sharp focus on the outside surface of the cylinder) was used for welding to assure full penetration with a single pass weld without preheating. This defocus setting provided sharp focus approximately one-third of the way through the cylinder wall. The copper rings prevented interior "suckback" and served to blend the interior contours with minimal pushthrough. Defocus parameters were developed to result in a uniform, slightly tapered bead of minimum width with minimum top surface crowning. Every effort was made to limit heat during welding in order to minimize tempering of the low-toughness material. Typical specimen components and jig accessories are shown in Fig. 5.12.

The subassembly was transferred back to the machine shop for removal of the copper chill rings and for machining of the outside surface in the weld-joint region. The cylinder subassembly was then transferred to a shop milling cutter for slot milling to a depth of 30.2 mm (1.1875 in.) as described in Section 5.4.1. The slotted subassembly was returned to the weld chamber for a two-step EB weld flawing operation — first on the 15° slope with the subassembly placed onto the table jig (Fig. 5.12) and then on a lathe with the slot placed horizontally and aligned below the gun. The EB flawing welds were placed along the slot bottom with sharp surface focus. Power and speed selections were programmed for a weld of pear-shaped contour and 8 mm (0.3125 in.) depth so that upon hydrogen charging the bead would crack and form a through-ligament flaw below the bottom of the slot as well as a flaw of equal depth on the slope. The EB was adjusted to 40 kV and 176 mA, to a sharp focus at the surface, and to a traverse speed of 2280 mm/min (90 in./min).

A prefabricated 1.6-mm-thick (0.0625-in.) 304L stainless steel cylinder was cut 76 mm (3 in.) shorter than the three-cylinder subassembly length and slipped into the subassembly with about 0.76 mm (0.030 in.) diametral clearance. The carbon steel cylinders were then preheated to 177°C (350°F) and the stainless steel liner was heliarc tacked, followed by gas-tungsten arc seam welding to UCN welding specification W501 using 1.6-mm-diam INCO 82 filler. Visual weld inspection and a mass spectrometer helium leak check were employed to assure seal integrity.

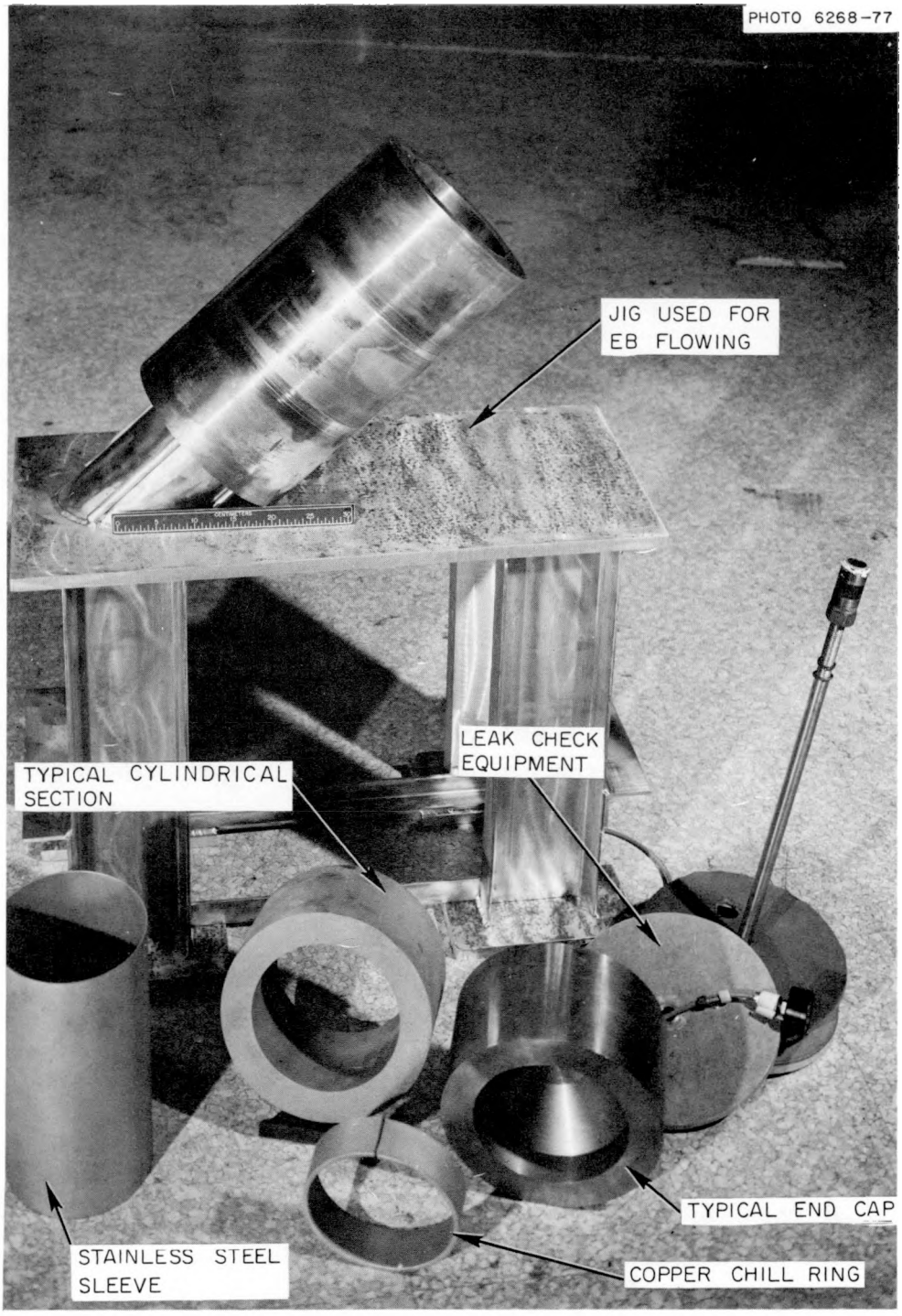

Fig. 5.12. Crack-arrest model assembly parts.

End caps were fitted to the lined subassembly via copper chill rings, and the complete test specimen was reinserted into the lathe for transfer into the weld chamber.

5.4.4 Test results

The first and second crack-arrest models were tested March 3 and 31, 1977, in a specially designed concrete and steel enclosed pit that had been used for previous ORNL pressure vessel model tests. The two models, including the flaw size and flaw location, were identical. The only significant difference in the tests was that the first model was tested at 91°C (196°F) and the second at 4°C (39°F).

The models were instrumented with several thermocouples, two pressure transducers (plus a dial pressure gage at the control panel), two crack extension ladders, and either three or four strain gages. The crack extension indicators consisted of individual foil gages (Micro Measurement TK-06-19CDK-350) connected in parallel along the path of expected crack propagation. Figure 5.13, a photograph of the first crack-arrest model, shows the arrangement of the 11 crack extension gages, 8 of which were connected in parallel to form one of the ladders. The three remaining gages (the third, seventh, and ninth from the crack tip) formed an independent ladder that was used to trigger the high-speed recording equipment. Strip charts, oscilloscopes, and fast digital memory units were used to record experimental data. The vessels were pressurized hydraulically.

Plots of pressure and crack extension (indications from the 8-gage ladder) are shown in Fig. 5.14 as functions of time for the first model test. Also shown in the figure, as an intermittent horizontal line, are the periods when the pump was actually being used to pressurize the vessel. The first indication of crack extension was recorded at approximately 10 min into the test and at a pressure of 93 MPa (13,400 psi). The pressure was increased uniformly over the next 80 sec to 102 MPa (14,750 psi). Slow, stable crack growth accompanied the increase in pressure. Figure 5.15 shows the period of initial crack extension on an expanded time scale. Pumping was discontinued at that point for approximately 18 min. Pressure and crack length remained nearly constant over this period. When pumping

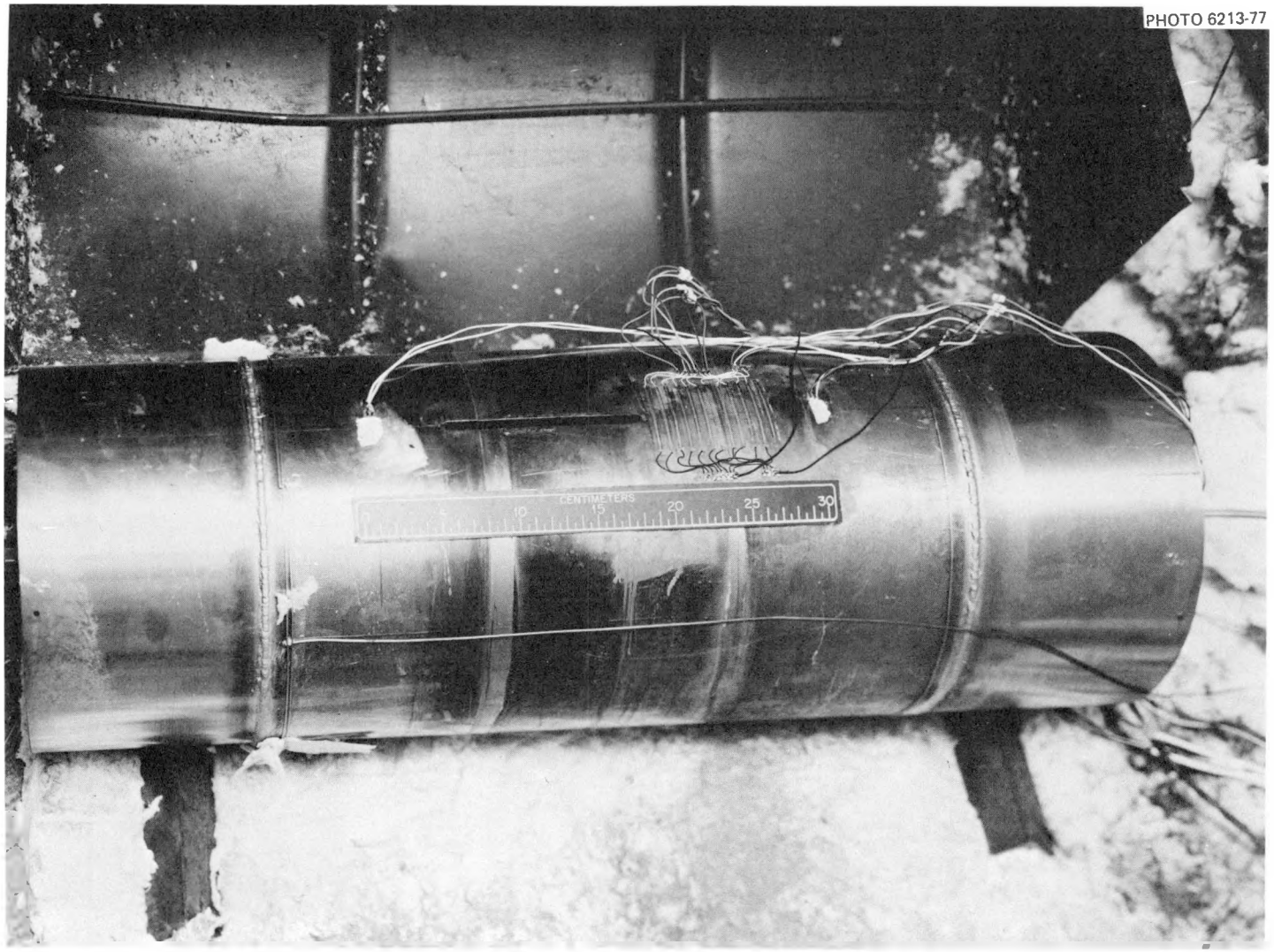

Fig. 5.13. First crack-arrest model with instrumentation.

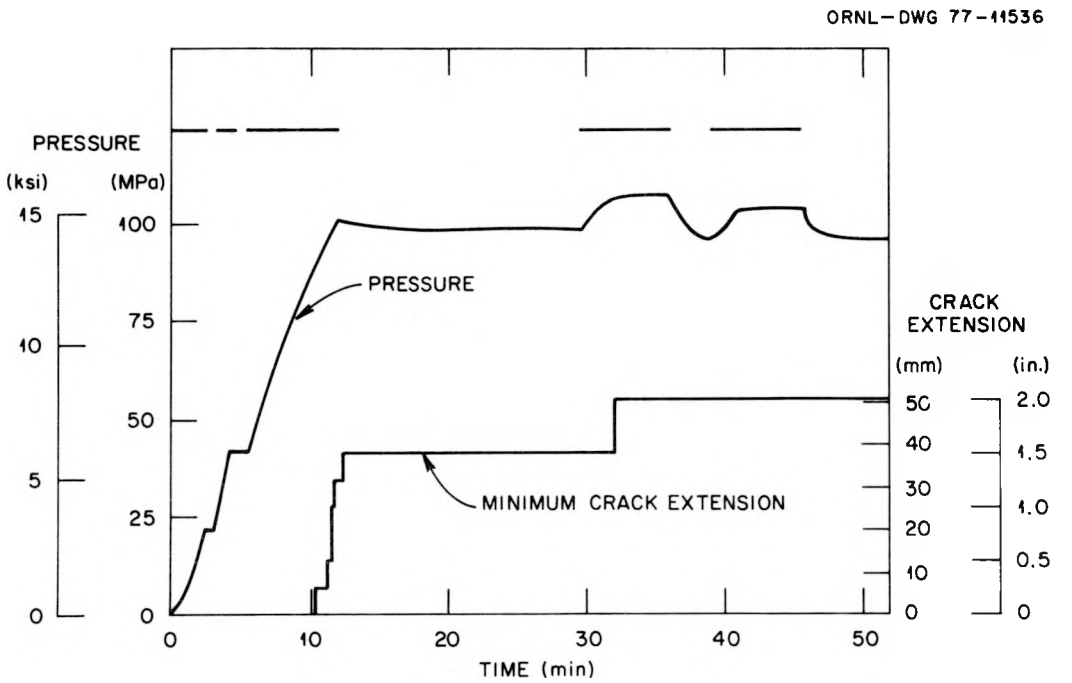

Fig. 5.14. Pressure and minimum indicated crack extension vs time for the first model test at 91°C (196°F). The solid horizontal line indicates periods when pumping occurred.

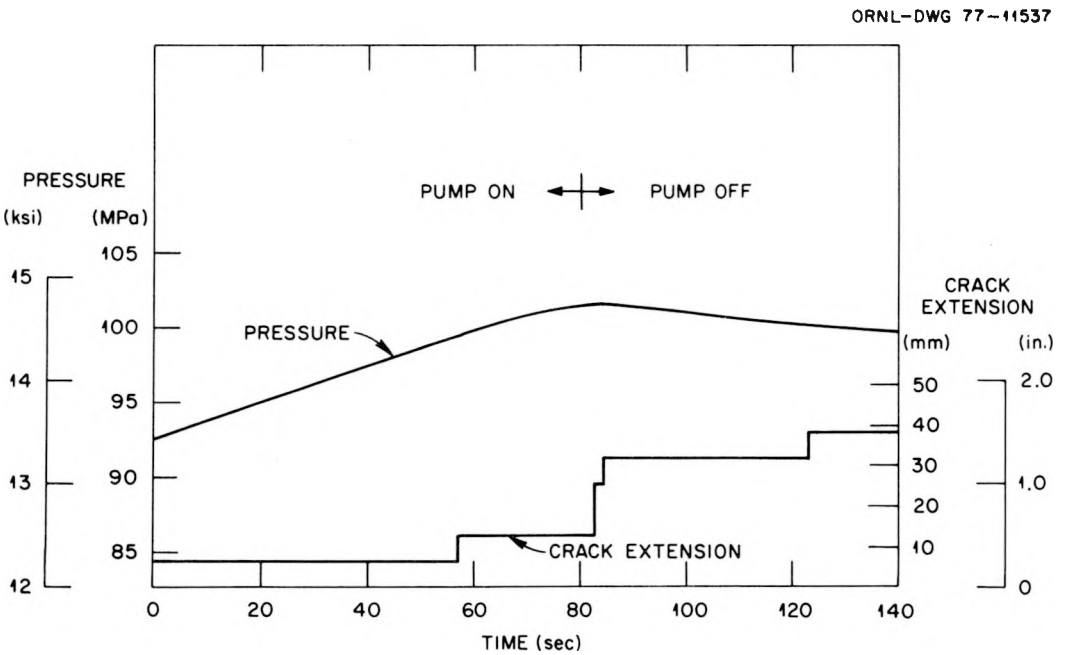

Fig. 5.15. Expanded pressure and crack extension history from the first crack-arrest model test.

was resumed, further crack extension was detected at 107 MPa (15,500 psi). At that point, the stainless steel liner began to leak and an increase in pressure above 108 MPa (15,600 psi) was not possible. Preliminary post-test evaluation of the flawed region indicated that flat fracture was the predominant mode of failure. The crack did propagate through the EB weld into plate 57 material. The vessel is currently being sectioned for further study of the crack surfaces.

Figure 5.16 shows the crack extension, pressure, and pumping periods for the second model test. The long "hold period" that occurred 10 min into the test was necessitated because of difficulties with a strip-chart recorder and is not indicative of any peculiar vessel behavior. As in the first test, increasing pressure was needed to extend the crack after it had started. The first indication of crack extension occurred at 76 MPa (11 ksi). Pressurization was continued up to 103 MPa (15 ksi), held constant for 5 min, and the test terminated. The crack had extended nearly 51 mm (2 in.). At two times, indicated by the asterisks in Fig. 5.16, a very loud "ping" was heard. Figure 5.17 is a photograph of an oscilloscope trace that occurred during the first "ping". The horizontal scale

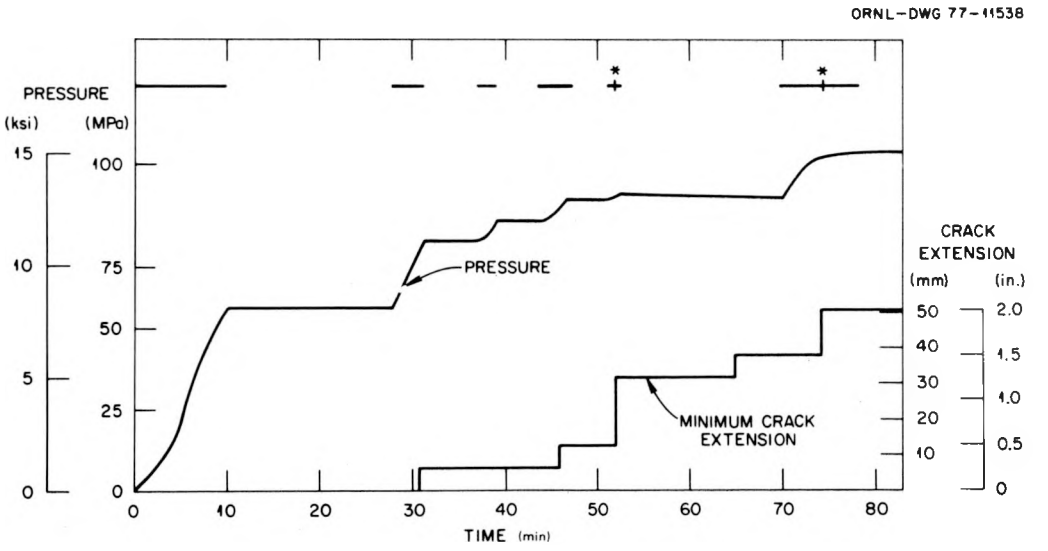

Fig. 5.16. Pressure and mimimum indicated crack extension vs time for the second model test at 4°C (39°F). The solid horizontal line indicates periods when pumping occurred; the asterisks indicate the times when loud "pings" were heard.

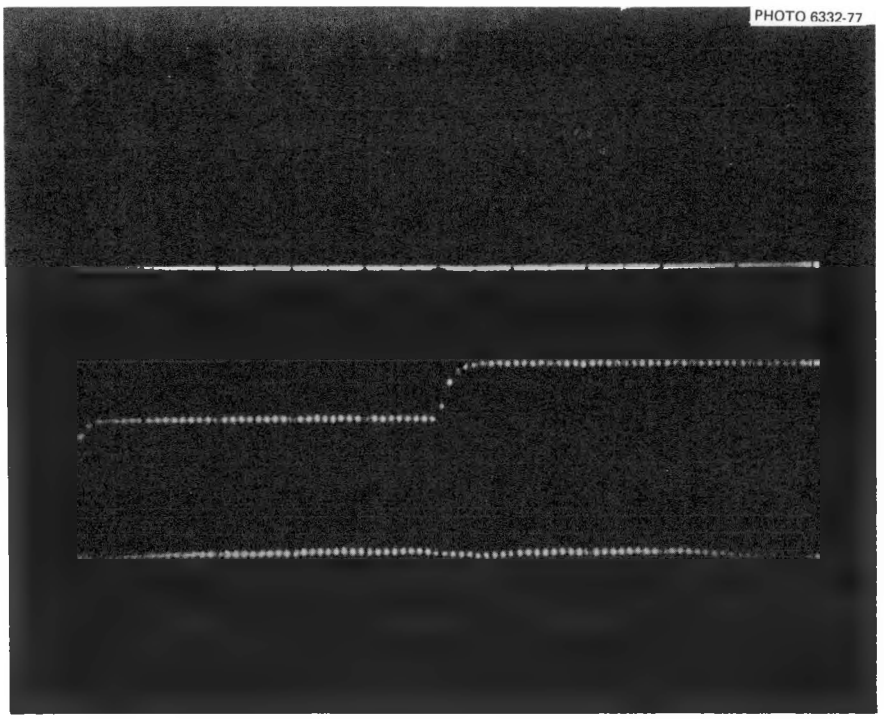

Fig. 5.17. Photograph of an oscilloscope trace at the time of the first audible crack extension. Horizontal scale is 20 μsec per major division. From top to bottom, the traces are pressure, eight-gage ladder, and axial strain gage 180° from the flaw.

is 20 μsec per major division. The top and bottom traces are the outputs of a pressure transducer and an axial strain gage, 180° from the flaw. The center trace is the output of the 8-gage ladder. The oscilloscope was triggered by the breaking of the third leg of the 8-gage ladder. The step change in ladder output approximately 100 μsec after the breaking of the third leg is the change in output due to the breaking of the fourth leg. The fifth leg broke approximately 5 min later. From the oscilloscope trace, one can estimate that the average crack velocity associated with the noise was approximately 63.5 m/sec (2500 in./sec). Comparable data were not obtained for the second "ping," which apparently accompanied fast fracture across the heat-affected zone of the EB weld and subsequent arrest in plate 57.

5.4.5 Conclusions

As the material property data in Figs. 5.9 and 5.10 indicate, at the two model test temperatures, the quenched-only material is quite inferior to normal reactor pressure vessel steel represented by plate 57. The inferior material was, however, able to withstand extensive stable crack extension, which for a pressure vessel implies an increasing stress-intensity factor, without catastrophic rupture. In fact, an increase in pressure was normally required to cause crack extension.

It should be noted that the very high yield stress [i.e., 1083 MPa, (157 ksi)] of the brittle material implies that considerable constraint exists near the crack tip. According to the ASTM E-399 thickness criterion, a 38.1-mm-thick (1.5-in.) specimen made from the brittle material could develop a valid K_{Ic} up to 134 $MN \cdot m^{-3/2}$ (122 ksi $\sqrt{in.}$). If the pressure and crack length at each break in the ladder gage are used to calculate a stress-intensity factor according to the method suggested by Hahn, Sarrate, and Rosenfield[13] for low to medium toughness vessels with relatively long axial cracks, the results presented in Fig. 5.18 are found. Since the cracks grew stably, except for the two short run-arrest events in the second model tests, it can be concluded from the figure that the resistance to crack extension of these two vessels increased as the cracks grew.

The design pressure for the models, if they were made for quenched and tempered A533, would be 67 MPa (9700 psi) (i.e., the same as that for an intermediate test vessel). Both model tests had through-wall flaws with lengths exceeding the vessel radius and with their initial crack tips in highly degraded material. The Charpy-V impact energy for the brittle material was 41 J (30 ft-lb) at the test temperature of the first model test and 22 J (16 ft-lb) at the test temperature for the second. Even with the large flaw and degraded material, the pressure at which crack extension was initially detected exceeded the vessel design pressure.

The two crack run and arrest events characterized by the loud "pings" during the second model test produced some unexpected results. The first

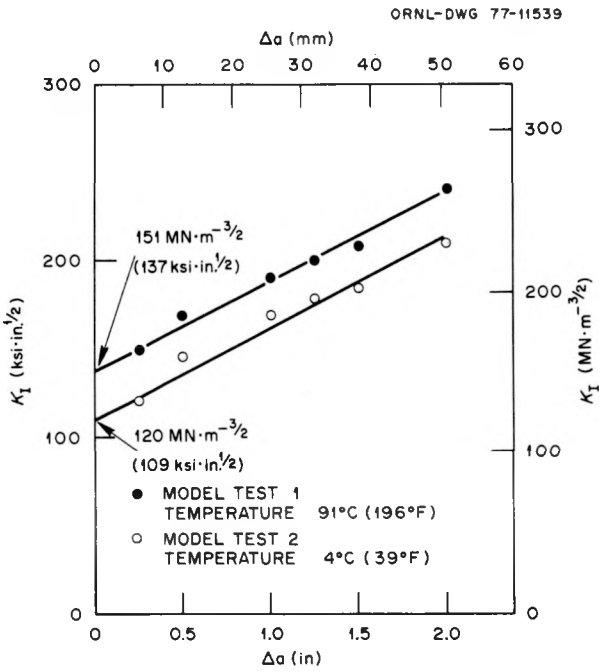

Fig. 5.18. Statically calculated stress-intensity factors based on instantaneous crack length and pressure during crack extension for crack-arrest model tests 1 and 2.

initiated and arrested in macroscopically homogeneous material. The pressure was essentially constant and the stress-intensity factor thus increased during propagation. The crack extension was small relative to the dimensions of the vessel, and it would therefore be likely that the dynamic stress-intensity factor would not differ significantly from the static value. The same observations apply to the second run-arrest event except that the crack apparently arrested in the tough material. The stress-intensity factor at arrest, however, far exceeded the published values of toughness. This can be seen in Fig. 5.19, which shows the BCL data,[6] the MRL data[7] for A533, the dynamic precracked Charpy data $(K_{Idd})^{12}$ for plate 57, and the statically determined stress-intensity factor for the second run-arrest event in the second model test. The K_{Idd} was included merely for comparison with generally accepted crack-arrest values. The very high arrest value suggested by the crack-arrest model data point could be a result of shear lip formation in the model test, which does not occur in standard crack-arrest specimens employing side grooves. Thus the

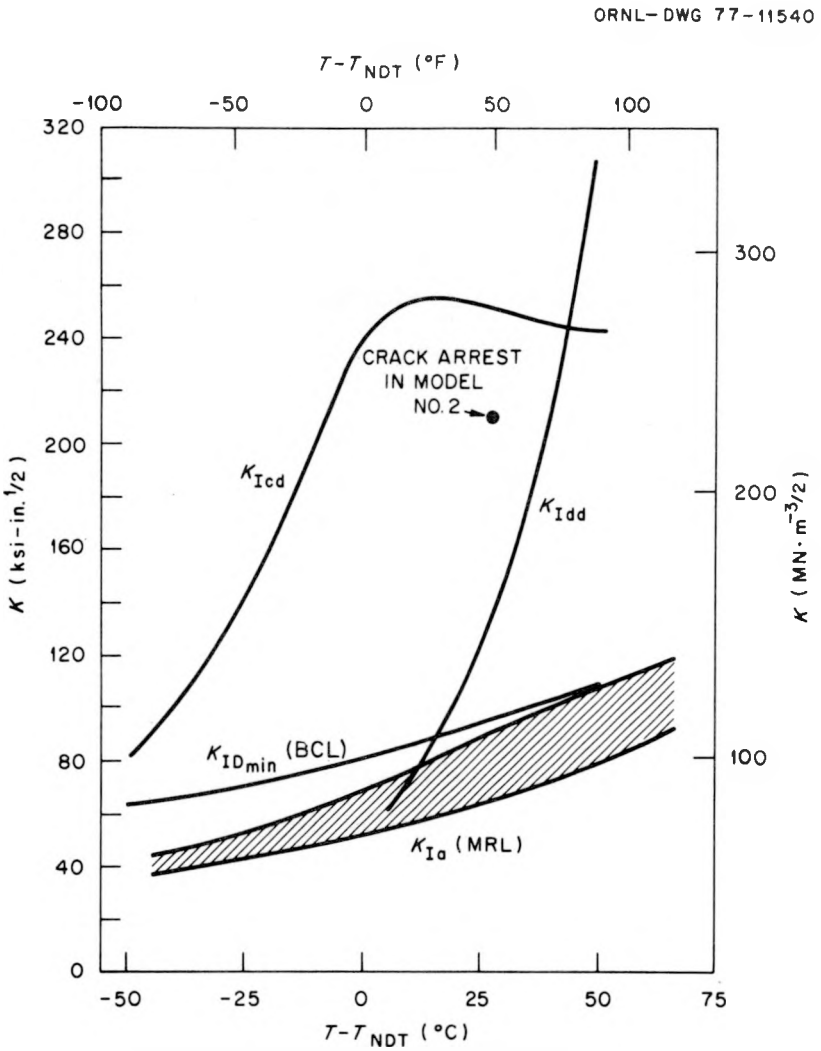

Fig. 5.19. Crack-arrest data vs temperature for A533B. The crack-arrest point indicates the value of K subsequent to the second "ping".

resistance to fast fracture by the crack-arrest model material could be much greater than the values reported by BCL and MRL. The velocity at which the crack arrested could also be a reason for the high apparent crack-arrest value in the model test. It has been shown[6] that the resistance to crack propagation is dependent on crack velocity. Thus, if the crack did not attain the velocity associated with the minimum on a K_{Id} vs crack velocity curve, the appropriate crack-arrest stress intensity could be much larger than the minimum values that appear in the literature.

5.5 Parametric Study of Crack Velocity Influence on the Crack-Arrest Capability of a Pressure Vessel

G. C. Smith

The objective of the work reported here was to assess the influence of crack velocity on the crack-arrest potential of a pressure vessel. Since this work is in support of the crack-arrest model tests, the configuration studied had dimensions equal to the model shown schematically in Fig. 5.5 (with the exception of the flaw geometry). For all the results reported here, the flaw was assumed to be 76.2 mm long (3.0 in.) and was assumed to propagate from a single crack front with one of three constant crack front velocities for a distance of 76.2 mm, at which point it abruptly arrested. Results are also presented for the postarrest stress-intensity factor.

Reference 14 contains a discussion of a two-dimensional finite-element analysis of a plate containing a rapidly propagating crack. The method used there, which employed stiff "breakable" bars along the crack propagation path, was also used for this work. The displacement basis method of calculating stress-intensity factors (i.e., relating the stress-intensity factor to the near-tip crack-opening displacement) was used for the present work. The displacements of the three nodes closest to the crack front were averaged in this calculation.

The finite-element grid used for this work is shown in Fig. 5.20. Because of the one plane of symmetry, only half of the model had to be analyzed. The model consisted of 105 sixteen-node isoparametric bricks and 54 massless, stiff bars. Eighteen of these bars break in sequential order and at prescribed times corresponding to the imposed crack front velocity. Three crack front velocities were studied. For convenience, 90 time integration intervals were used for each of the three problems, and crack extension (i.e., the breaking of a row of three bars) occurred every 10th interval at six different times. The end caps were not included in the model. However, axial loads consistent with the internal pressure of the vessel were applied to the ends of the model. The vessel behavior was assumed to be linear elastic.

The time integration intervals were taken to be 0.64, 1.27, and 1.90 μsec, which correspond to crack velocities of 500 m/sec (19,685 in./sec),

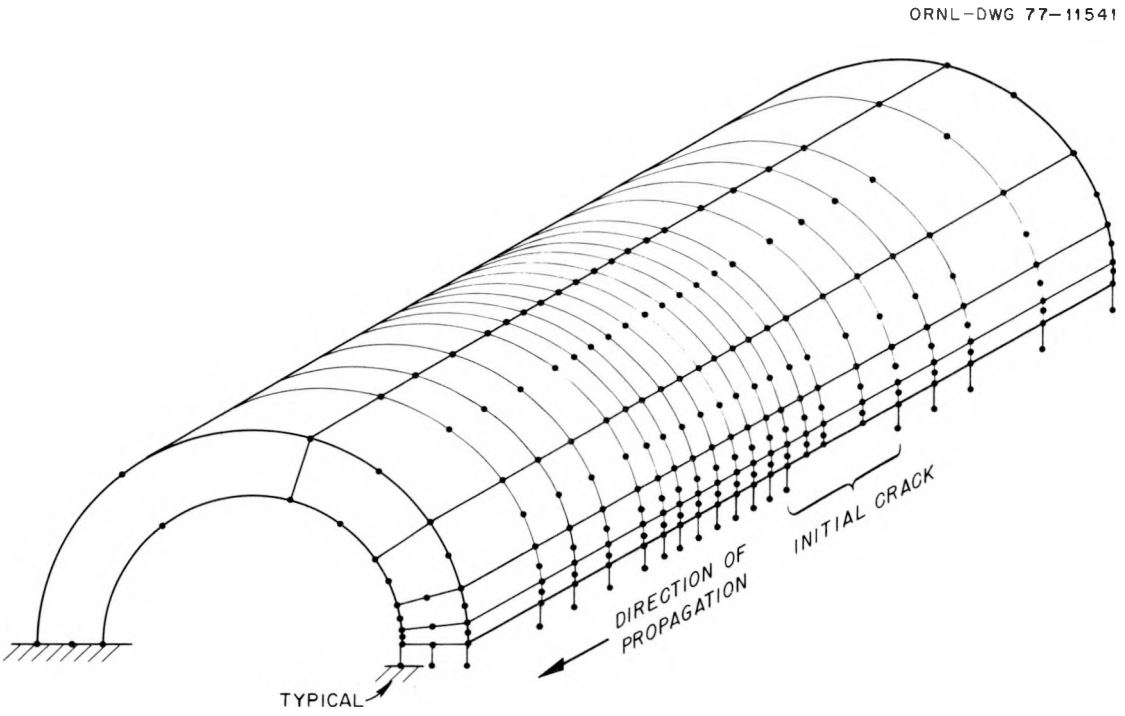

Fig. 5.20. Finite-element grid used to study the effect of velocity on the dynamic stress-intensity factor during crack propagation and after arrest.

1000 m/sec (39,370 in./sec), and 1500 m/sec (59,055 in./sec). The stress-intensity factor normalized by the vessel internal pressure, which was assumed to be constant (variable pressure can be handled) during crack propagation, is shown in Fig. 5.21 for three crack front velocities as a function of time normalized by the time integration step size. The results indicate that the effect of crack velocity is quite large for the range of crack front velocities expected during unstable crack extention in the crack-arrest models. The figure also shows that the stress-intensity factor tends to decrease with increased velocities for a given crack length, as predicted by a previously published simplified method.[5] However, these results also suggest that the use of a static solution for the determination of crack arrest may not always be conservative for geometries that exhibit increasing static stress intensities with increased crack length (as opposed to the double cantilever beam where the static stress-intensity factor tends to decrease with crack extension). Finally,

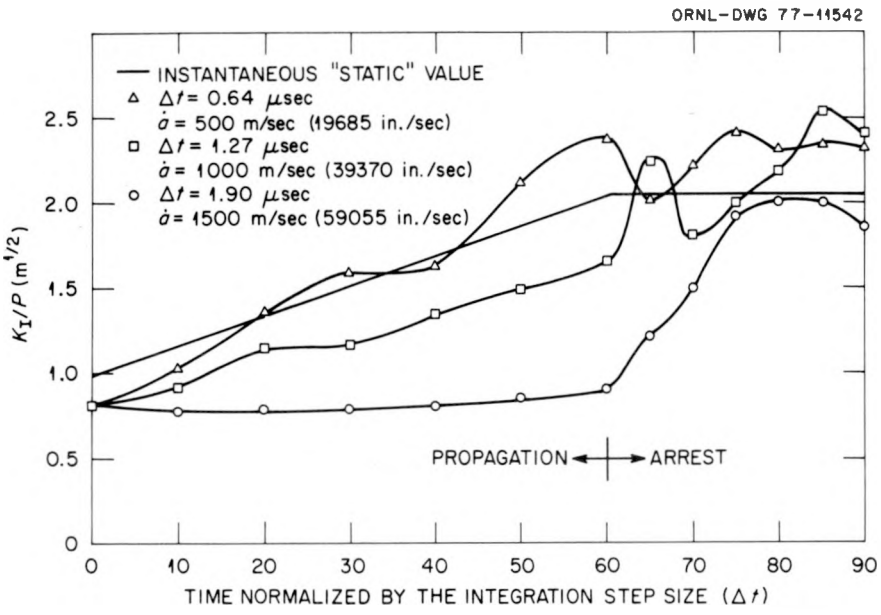

Fig. 5.21. Dynamic stress-intensity factor K_I normalized by the crack-arrest model internal pressure plotted vs the number of time integration steps (time normalized by step size, Δt) for three imposed crack velocities, å.

the results shown in Fig. 5.21 indicate that the postarrest stress-intensity factor can exhibit an overshoot of approximately 25%, which is about that predicted by Sih, Embley, and Ravera[15] in their exact solution of a suddenly appearing crack in an infinite solid. Further studies involving grid-size effects are planned.

5.6 Material Tests for Small Crack-Arrest Test Vessels

W. J. Stelzman D. A. Canonico

We have continued characterization of both the high (57W) and low (03JZ) toughness materials which will be used to fabricate the model crack-arrest test vessels. Charpy-V impact data and static fracture toughness data from precracked Charpy specimens have been presented for both materials.[11,12] Dynamic fracture toughness data from precracked Charpy specimens have been presented[12] for the high toughness material

only. Tensile results for both materials using R- and W-oriented specimens tested at 20 and 93.3°C (68 and 200°F) are listed in Table 5.1. Large differences exist between the tensile properties of 03JZ and 57W. The use of the lower case t and the upper case T to identify the through-the-thickness depth location in the 44.5- and 152-mm-thick (1.75- and 6-in.) sections is consistent with previous reporting.[11]

At room temperature, the average yield and ultimate stresses for 03JZ (1139 and 1386 MPa, respectively) were 2 1/2 times higher than the 57W values. The total elongation (6.9%) and the reduction of area (36.8%) were one-third and one-half, respectively, of the values received from the 57W base material. Increasing the test temperature to 93.3°C resulted in small decreases in the yield and ultimate stresses and total elongation but no significant change in the reduction of area of 57W. No significant changes in tensile properties were observed at the higher temperature for 03JZ. A comparison of the tensile results from the R and W orientations at room temperature indicated slightly lower stresses and reduction of areas and slightly higher total elongations in both materials.

The nil ductility transition temperature (NDTT) for 57W was also determined using RT- and WT-oriented type P-2 drop weight specimens.[16] At the 1/4 and 3/4T locations, an NDTT between −23.3 and −28.9°C (−10 and −20°F) was obtained from both the RT- and WT-oriented specimens. The number of WT specimens was limited.

In addition to using the water-quenched 03JZ for the "low" toughness material, we are considering the properties of 152-mm-thick (6-in.) plate section 04B.[10] A section of 304-mm-thick (12-in.) HSST plate 04B was split into 152-mm-thick sections and subsequently cut into 254-mm-OD × 178-mm-ID × 152-mm-long (10 × 7 × 6 in.) cylinders and 38.1-mm-thick (1.5-in.) sections where the 38.1-mm dimension is parallel to the plate-rolling direction (R). The cylinders and plates were then reaustenitized for 1.5 hr at 872°C (1600°F) and quenched in chilled, agitated water. Due to the limited amount of material and dimensional problems, only W-oriented specimens were prepared. Fracture toughness data from precracked Charpy and Charpy-V impact specimens are being obtained.

Table 5.1. Tensile properties of 152-mm-thick (6-in.) HSST plate section 57W and 44.5-mm-thick (1.75-in.) through-thickness slices from HSST plate section 03JZ

Depth	Test temperature [°C (°F)]	Strength properties		Total elongation[a] (%)	Reduction of area (%)
		Lower yield [MPa (ksi)]	Ultimate tensile [MPa (ksi)]		
		57W (R orientation)			
0.40T	20.0 (68)	461 (66.9)	618 (89.7)	18.9	70.9
0.59T	20.0 (68)	462 (67.0)	614 (89.1)	20.3	72.1
0.31T	93.3 (200)	441 (63.9)	578 (83.9)	17.4	72.1
0.49T	93.3 (200)	435 (63.1)	576 (83.6)	17.3	71.7
		57W (W orientation)			
0.40T	20.0 (68)	453 (65.7)	601 (87.2)	20.1	67.1
0.31T	93.3 (200)	427 (62.0)	561 (81.3)	17.9	72.0
		03JZ (R orientation)			
0.7t (0.2T)	20.0 (68)	1041 (151)	1338 (194)	6.2	29.0
0.7t (0.5T)	20.0 (68)	1138 (165)	1434 (208)	7.6	44.7
0.3t (0.2T)	93.3 (200)	1027 (149)	1289 (187)	6.6	42.3
0.3t (0.5T)	93.3 (200)	1138 (165)	1496 (217)	6.3	29.1
		03JZ (W orientation)			
0.3t (0.5T)	20.0 (68)	1069 (155)	1400 (203)	8.0	35.3
0.3t (0.2T)	93.3 (200)	1082 (157)	1358 (197)	3.7	13.5

[a]Ratio of gage length to gage diameter = 7; strain rate = 0.016 min^{-1}.

5.7 Fractographic Examination of ITV-7A

D. A. Canonico R. S. Crouse

A fractographic examination employing both light microscopy and scanning electron microscopy (SEM) of the fracture surface from intermediate test vessel V-7A was completed during this quarter. Figure 5.22 is an approximately half-size photograph of the fracture from V-7A. The goal of the fractographic examination was to determine the mode of fracture that occurred during testing. Of particular interest were the region in the main section of the vessel wall beneath the EB crack starter (areas 1 and 5 in Fig. 5.22) and the ligament region beneath the deepest part of the flaw, where rupture resulted in the termination of the test. The latter region is typified by areas 2, 3, and 4 in the figure.

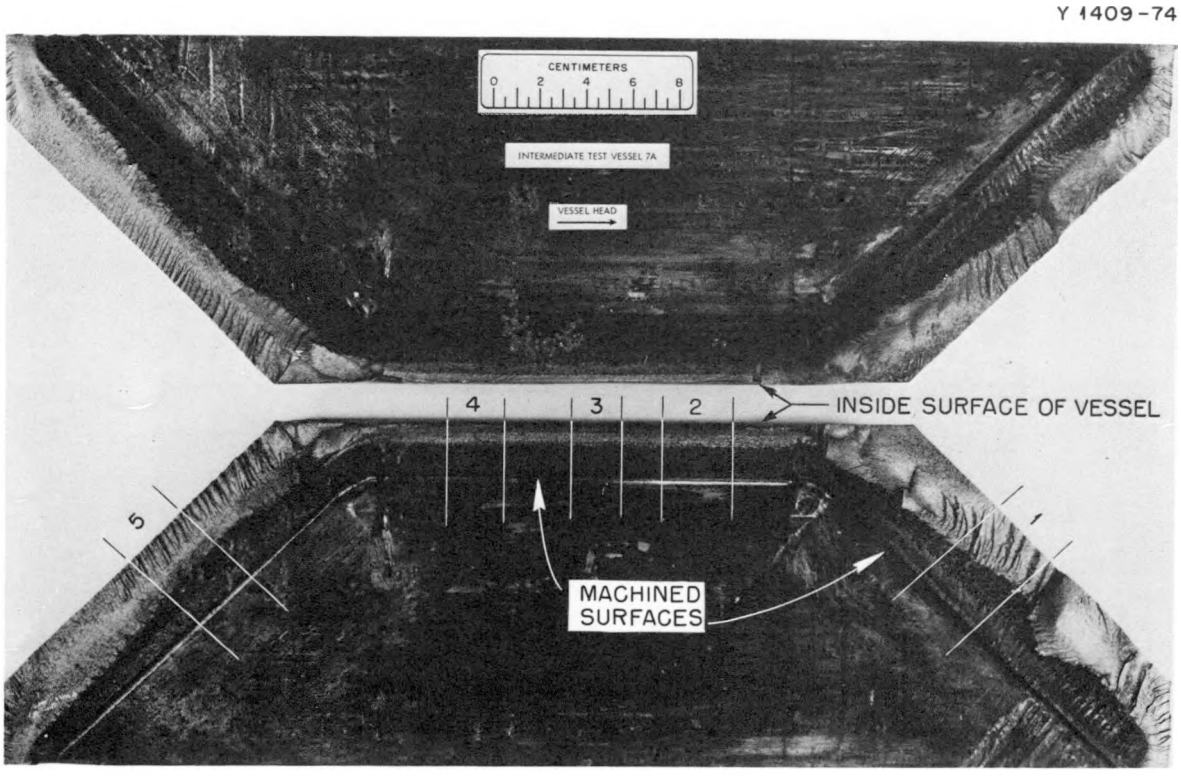

Fig. 5.22. Photograph of the fractured surfaces from intermediate test vessel V-7A. The regions of the fracture that were examined by scanning electron microscopy are areas 1 to 5.

The fractured zone was removed from the vessel, chilled, and separated. The bright portions of areas 1 and 5 are the areas that were fractured at low temperature in order to separate the two surfaces. Figure 5.23 contains SEM photomicrographs of the bright fracture areas. The fractures in this area, as expected, are cleavage. Although not the area of principal interest in this study, Fig. 5.23 provides an example of a frangible fracture.

The region that leaked in V-7A, between areas 2 and 4 in Fig. 5.22, was examined to determine the mode of cracking and to estimate the length of the ruptured surface. Previous estimates of the length of the crack were based on visual examination with the naked eye of the inside surface of the vessel before the fractured zone was chilled and separated.[17] In the earlier examination the inside surface rupture could not be seen until the zone was cut from the vessel; the relief of restraint during removal

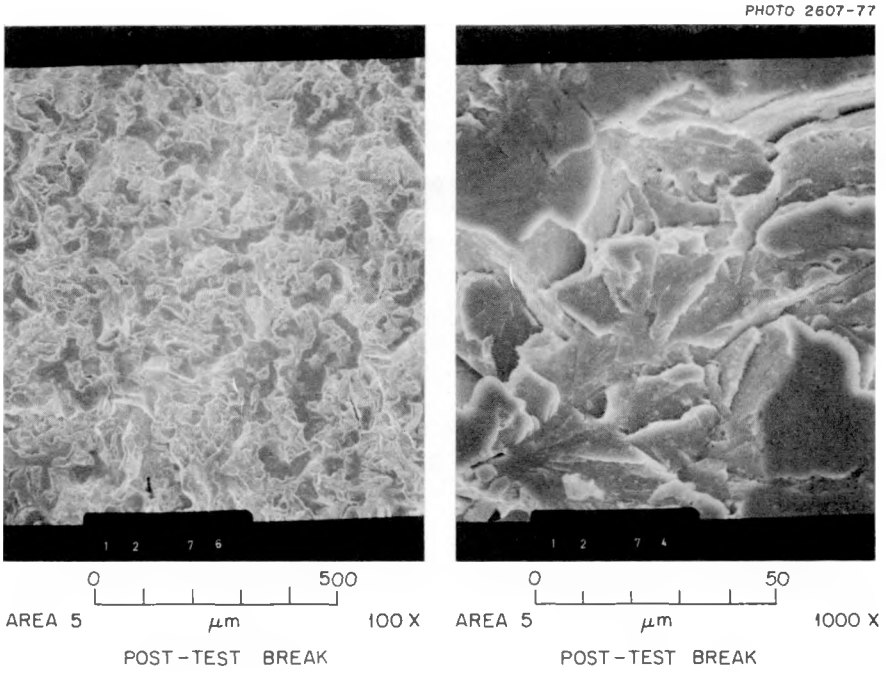

Fig. 5. 23. Scanning electron microscopy photomicrographs of the area of the V-7A fracture surface that was separated after the test at extremely low temperatures. The fracture occurred at low temperature by the cleavage mode. These photomicrographs are representative of the SEM appearance of brittle fracture in this A533, grade B, class 1 material. Original reduced 37%.

allowed the rupture to open and possibly allowed additional tearing. The fractographic examination of the ligament region between areas 2 and 4 shows a length of about 73 mm (2.9 in.) of plastically deformed fracture surface bounded at each end by a thin, pointed fracture area along the inside surface of the vessel. These thin areas have an appearance similar to that of the cleavage in areas 1 and 5, which was formed when the specimen was separated for examination. We conclude that during the test the ligament must have ruptured to the inside surface over a distance of at least 73 mm and, from fractographic evidence, no more than this amount.

An SEM examination of the region that breached the inner wall was completed. Figure 5.24 shows that the fracture surface near the inside is essentially featureless. The surfaces that evolved as a consequence of the crack extension during testing subsequently came into intimate contact when the pressure was relieved and were then plastically deformed.

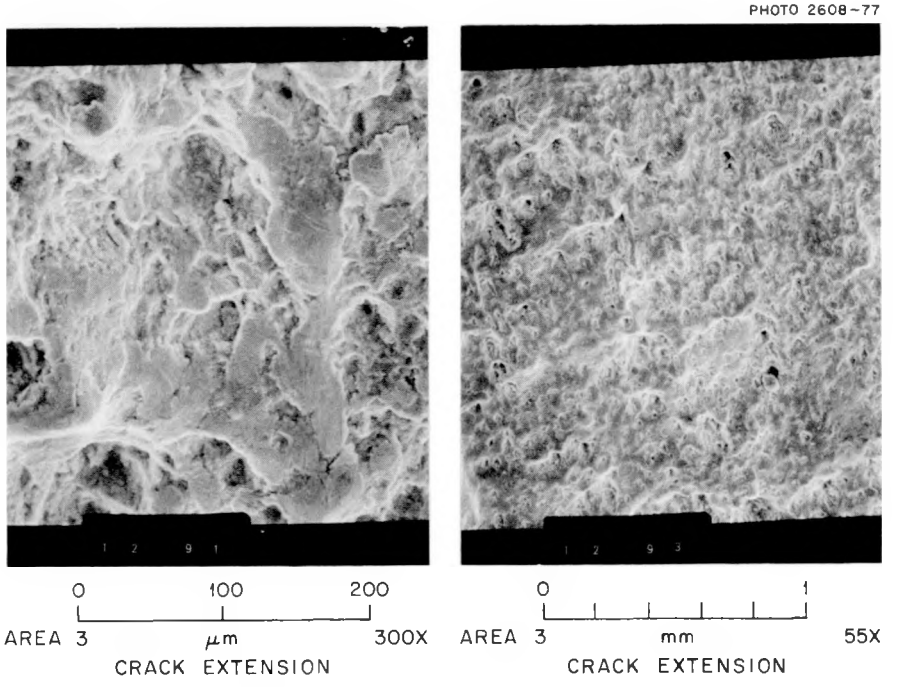

Fig. 5.24. Scanning electron microscopy photomicrographs of the region of the crack in V-7A that breached the inner wall (area 3 in Fig. 5.22). The fracture surface was flat facets, indicative of an area that was plastically deformed. This deformation undoubtedly occurred when the internal pressure was released and the two surfaces were brought into intimate contact. Original reduced 37%.

The flat facets in Fig. 5.24 are the result of this deformation. There is evidence that the fracture surface has a dimple morphology; however, this could not be uncontestably confirmed. Rather, it can be inferred from the morphology of the fracture surface at areas 1 and 5 in Fig. 5-22, both of which exhibited a dimple fracture mode below the EB weld crack. Figure 5.25 contains SEM photomicrographs of the areas below the EB weld that fractured during the V-7A test. The surfaces exhibit a dimple mode of fracture indicative of ductile tearing.

In summary, the crack in V-7A extended by ductile tearing until the inner wall was breached by the propagating crack front. The final crack extension that breached the inner wall was about 73 mm long. When the pressure was released, the fracture surfaces came into contact and were plastically deformed, resulting in the flat facets in the fracture surfaces evident in Figs. 5.24 and 5.25.

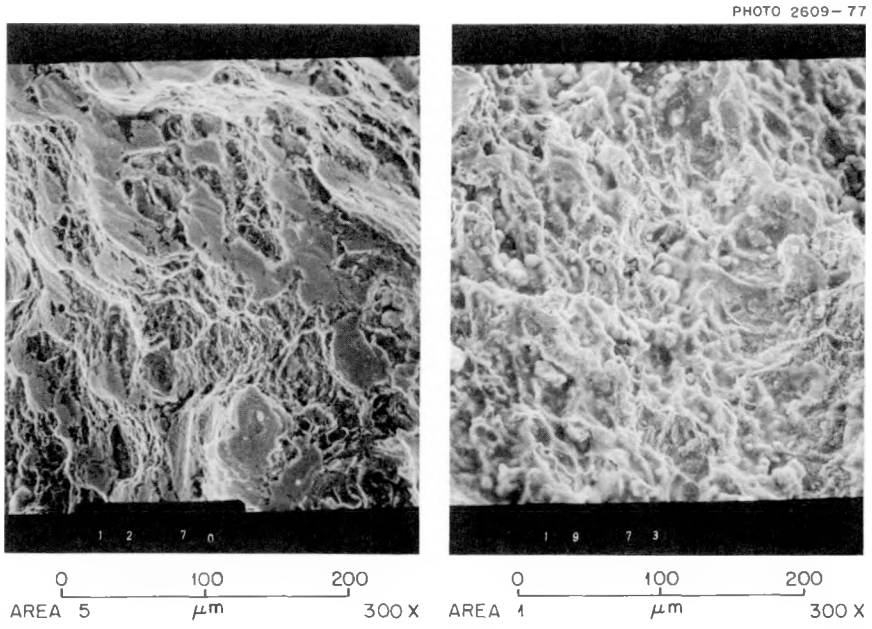

Fig. 5.25. Scanning electron microscopy photomicrographs representative of the regions within the wall of the V-7A vessel where the cracks extended and arrested (areas 1 and 5 in Fig. 5.22). The dimpled appearance of the fracture surface is indicative of ductile tearing. The flat facets are undoubtedly due to the plastic deformation that occurred when the pressure was released and the fracture surfaces were brought into intimate contact. Original reduced 38%.

References

1. P. P. Holz, "Preparations for HSST Intermediate Vessel Tests V-7B and V-8," *Heavy-Section Steel Technology Program Quart. Prog. Rep. October–December 1976*, ORNL/NUREG/TM-94, pp. 32–38.

2. J. G. Merkle et al., *Test of 6-Inch-Thick Pressure Vessels. Series 3: Intermediate Test Vessel V-7*, ORNL/NUREG/TM-1 (August 1976).

3. P. P. Holz, "Flaw Preparation in Intermediate Test Vessel V-7A," *Quarterly Progress Report on the Heavy-Section Steel Technology Program for October–December 1975*, ORNL/NUREG/TM-3, pp. 56–59.

4. Richard Smith, *Weld Repair of Heavy Section Steel Technology Program Vessel V-7*, EPRI NP-179 (ORNL/Sub/88242-76/1) (August 1976).

5. G. C. Smith, "A Simple Method for Analyzing the Dynamic Propagation and Arrest of Axial Through-Thickness Cracks in Cylinders," *Quarterly Progress Report on the Heavy-Section Steel Technology Program for October–December 1975*, ORNL/NUREG/TM-3, pp. 66–84.

6. G. T. Hahn et al., *Critical Experiments, Measurements and Analyses to Establish a Crack Arrest Methodology for Nuclear Pressure Vessel Steels*, BMI-NUREG-1959, pp. 5–14 (October 1976).

7. P. B. Crosley and E. J. Ripling, "Plane Strain Crack Arrest Characterization of Steels," *Journal of Pressure Vessel Technology*, pp. 291–298 (November 1975).

8. D. A. Canonico, "Metallurgical Simulation of Irradiation Effects on the Toughness of Pressure Vessel Steels," *Quarterly Progress Report on Reactor Safety Programs Sponsored by the Division of Reactor Safety Research for July–September 1974*, ORNL/TM-4729, Vol. II, pp. 91–95.

9. C. E. Childress, *Fabrication Procedures and Acceptance Data for ASTM A533 Welds and a 10-in.-thick ASTM A543 Plate of the Heavy-Section Steel Technology Program*, Documentary Report 3, ORNL-4313-3, pp. 64–73 (January 1971).

10. C. E. Childress, *Fabrication History of the Third and Fourth ASTM A533 Steel Plates of the Heavy-Section Steel Technology Program*, ORNL-4313-2 (February 1970).

11. W. J. Stelzman and D. A. Canonico, "Material Tests for Small Crack-Arrest Test Vessels," *Heavy-Section Steel Technology Program Quart. Prog. Rep. October–December 1976*, ORNL/NUREG/TM-94, pp. 51–58.

12. W. J. Stelzman and D. A. Canonico, "Material Tests for Small Crack-Arrest Test Vessels," *Heavy-Section Steel Technology Program Quart. Prog. Rep. April–June 1976*, ORNL/NUREG/TM-49, pp. 76–81.

13. G. T. Hahn, M. Sarrate, and A. R. Rosenfield, "Criteria for Crack Extension in Cylinder Pressure Vessels," *Int. J. Fract. Mech.* 5, 187–210 (1969).

14. G. C. Smith, "A Finite Element Analysis of Dynamic Crack Propagation," *Heavy-Section Steel Technology Program Quart. Prog. Rep. October–December 1976*, ORNL/NUREG/TM-94, pp. 46–50.

15. G. C. Sih, G. T. Embley, and R. S. Ravera, "Impact Response of a Thin Crack in Plane Extension," *Int. J. Solids Struct.* 8, 977–93 (1972).

16. American Society for Testing and Materials, Philadelphia, *1975 Annual Book of ASTM Standards, Pt. 10,* E208-69, pp. 307–326, November 1975.

17. R. H. Bryan, "Results of Sustained-Load Test of Vessel V-7A," *Heavy-Section Steel Technology Program Quart. Prog. Rep. July–September 1976,* ORNL/NUREG/TM-64, pp. 31–40.

6. THERMAL SHOCK INVESTIGATIONS

R. D. Cheverton S. E. Bolt

6.1 Introduction

During this reporting period for the LOCA-ECC Thermal Shock Program, the fourth thermal shock experiment (TSE-4) was conducted, metallographic examination of the TSE-1 and TSE-3 fracture surfaces was completed, the possibility of demonstrating warm prestressing using cryogenic quenching was investigated, an experimental program for determining heat transfer coefficients associated with cryogenic quenching was commenced, and progress was made in the development of a three-dimensional finite-element code for calculating stress-intensity factors.

6.2 TSE-4

The fourth thermal shock experiment (TSE-4) was conducted on January 19, 1977, at ORNL. Conditions for the experiment are summarized in Table 6.1. The test was a repeat of TSE-3 to the extent that the flaw was a long axial crack with a depth of ∿0.4 in., and the intended thermal shock was the most severe possible in the present test facility. The flaw in TSE-3 was prepared by machining a groove and then applying the EB weld; the test specimen was TSV-1, which had previously been used in TSE-1 and contained two plugged core holes at the time of TSE-3; and as a result of equipment malfunction the thermal shock was not as severe as desired. The TSE-4 test specimen, TSV-2, had been used previously in TSE-2. Following TSE-2, the 152-mm-long (6-in.) flawed region was removed by electrical discharge machining (EDM) and plugged. The long axial flaw for TSE-4 was placed 180° from the plug and was generated as for TSE-3 by means of the EB-weld technique but without the machined groove.

The purpose of TSE-4 was (1) to determine whether a long axial flaw will propagate under the specified thermal shock conditions, when the maximum K ratio is ∿1.2, (2) if the crack does propagate, to determine what the nominal calculated K ratio was at the time of initiation; and (3) to obtain a measurement of the arrest toughness.

Table 6.1. Test conditions for TSE-4

Experiment	TSE-4
Test specimen	TSV-2
Test specimen dimensions, m (in.)	
OD	0.53 (21)
ID	0.24 (9.5)
Length	0.91 (36)
Test specimen material	A508 class 2
Heat treatment	Quench only from 871 °C (1600°F)
Flaw	Long axial crack, a = 11 mm (0.42 in.)
Temperature, °C (°F)	
Wall (initial)	291 (555)
Sink (initial)	−25 (−13)
Sink (final)	−19 (−2)
Coolant	40 wt % methyl alcohol, 60 wt % water
Coolant flow rate m^3/hr (gpm)	114 (500)
Coolant pressure in test section, kPa (psi)	1020 (148)
Back pressure orifice diameter, mm (in.)	43.18 (1.700)
Heat transfer coefficient, $W \cdot m^{-2} \cdot K^{-1}$ (Btu hr^{-1} ft^{-2} $°F^{-1}$)	∿5700 (∿10^3)
$(K_I/K_{Ic})_{max}$	1.29
Time of occurrence of $(K_I/K_{Ic})_{max}$, min	∿5
Duration of experiment, min	30

Based on calculated transient temperature distributions, an estimated initial flaw depth, and crack-arrest data deduced from TSE-2, it was predicted that crack initiation would take place at 1.7 min into the transient and that arrest would take place at a fractional wall depth of 0.23. A single step, exclusive of subcritical crack growth and possible unstable crack growth associated with EB-weld residual stresses, would take place

and reinitiation would not be possible because $(K_I/K_{Ic})_{max} < 1$ for the arrested crack depth.

Acoustic-emission (AE) and crack opening displacement (COD) strain gages placed across the flaw were used to detect crack propagation. The AE measurements were made independently by Southwest Research Institute and Battelle Northwest. The COD gage locations along the length of the crack are shown in Fig. 6.1.

The AE and COD data collected during TSE-4 indicated that crack initiation and arrest took place. Output from the COD gages is summarized in Fig. 6.2 and Table 6.2. The initial event (0 to 6 sec) is the result of thermal effects on the gages, thermal stress, and perhaps subcritical crack growth. In the time range 60 to 80 sec, there were small step changes indicated by gages XE-31, -32, and -33; XE-32 indicated a second step that was considerably larger. At 150 sec, all five COD gages indicated relatively large steps, the three in the midregion being considerably larger than those near the ends.

Acoustic-emission data obtained by SwRI indicated that there were several "high-level" emissions in the time period 40 to 90 sec and again at ∿150 sec. Several events occurred from 160 to 240 sec but were of lower magnitude. It is possible that some of the acoustic emissions emanated from the core-hole plug that was located 180° from the long axial crack; it was not possible to differentiate between the two locations.

Very little AE data were collected by Battelle Northwest because a necessary "last-minute" relocation of waveguides apparently resulted in one of their two waveguides not seating properly against the test specimen. No AE data were recorded, but visual observation of the scope indicated events at ∿154, 224, and 235 sec, the first emission being much greater than the other two.

One other acoustic emission was detected during the thermal transient. At approximately 150 sec into the transient, several observers within 5 m (15 ft) of the test specimen heard a single loud "ping," similar to but louder than those heard during TSE-3.

After removal of the test specimen from the test facility, it was observed that all COD gages were buckled along their unbonded length

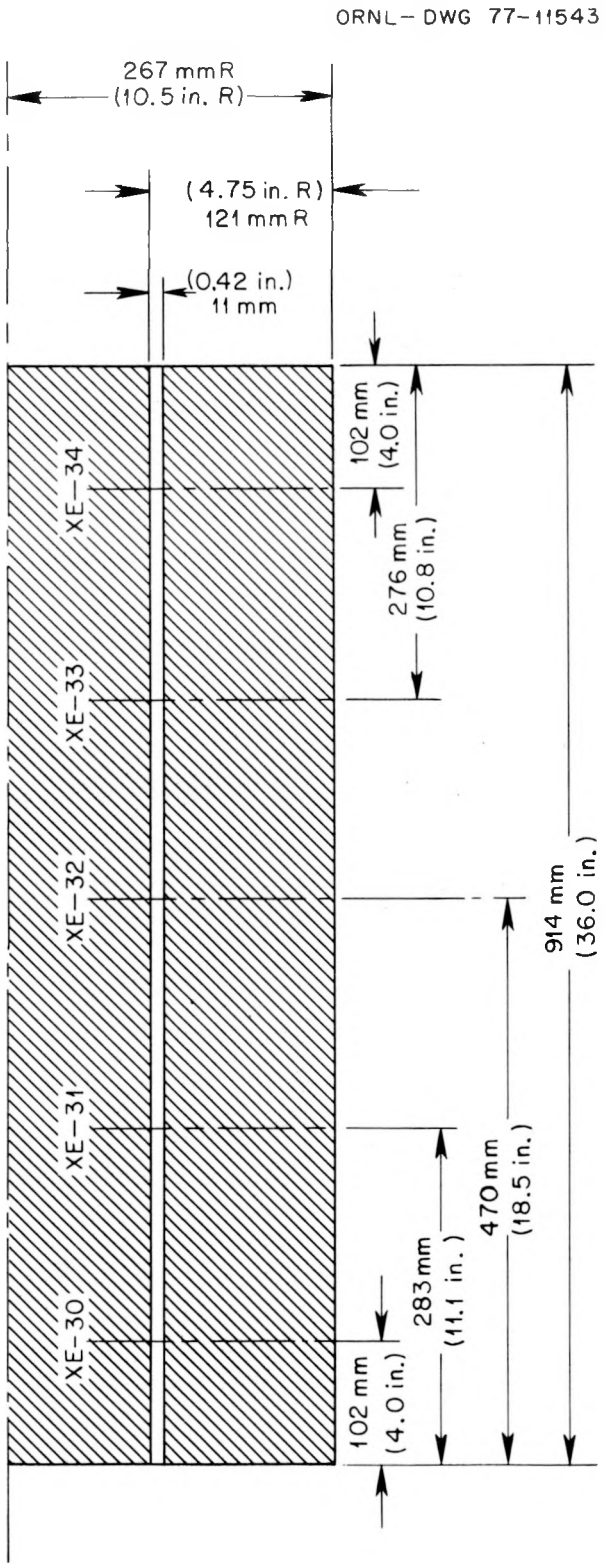

Fig. 6.1. Location of COD gages on TSV-2 for TSE-4.

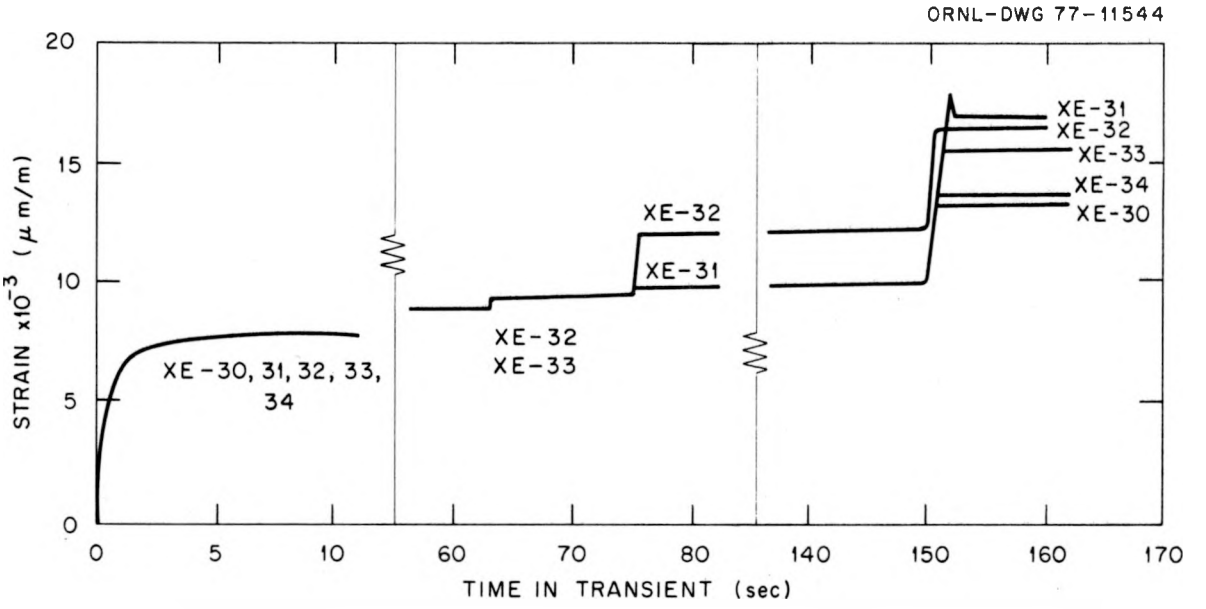

Fig. 6.2. Illustration of changes in strain from COD gages during TSE-4 (not quantitatively precise).

Table 6.2. Step changes in COD output during TSE-4

COD gage	Change in strain (μm/m) at time (sec)			
	0–6	64–68	74–76	150–152
XE-30	6400			3700
XE-31	7000		280	6600
XE-32	6700	150	2000	4800
XE-33	7000	380		5700
XE-34	6500			3700

(see Figs. 6.3 and 6.4). This would be expected because of the large indicated local strain (1.7%). This does not imply that the strain measurements during the transient were inaccurate; laboratory tests have shown that while under tension the partially bonded gage has good accuracy to 2% strain and is a satisfactory event indicator to 5% strain.[1]

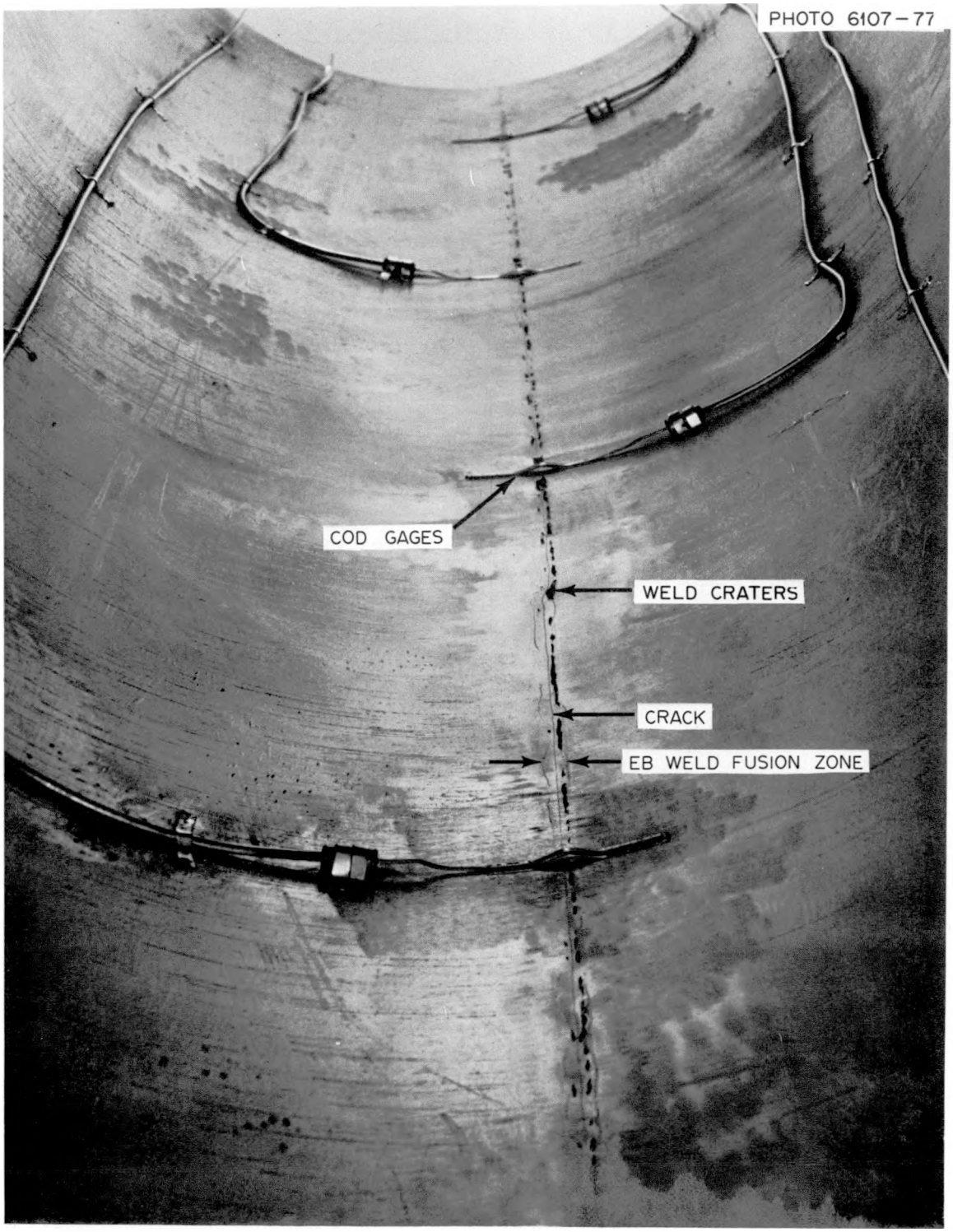

Fig. 6.3. View of inner surface of TSV-2 following TSE-4, showing EB-weld flaw and COD gages. Gages buckled during experiment.

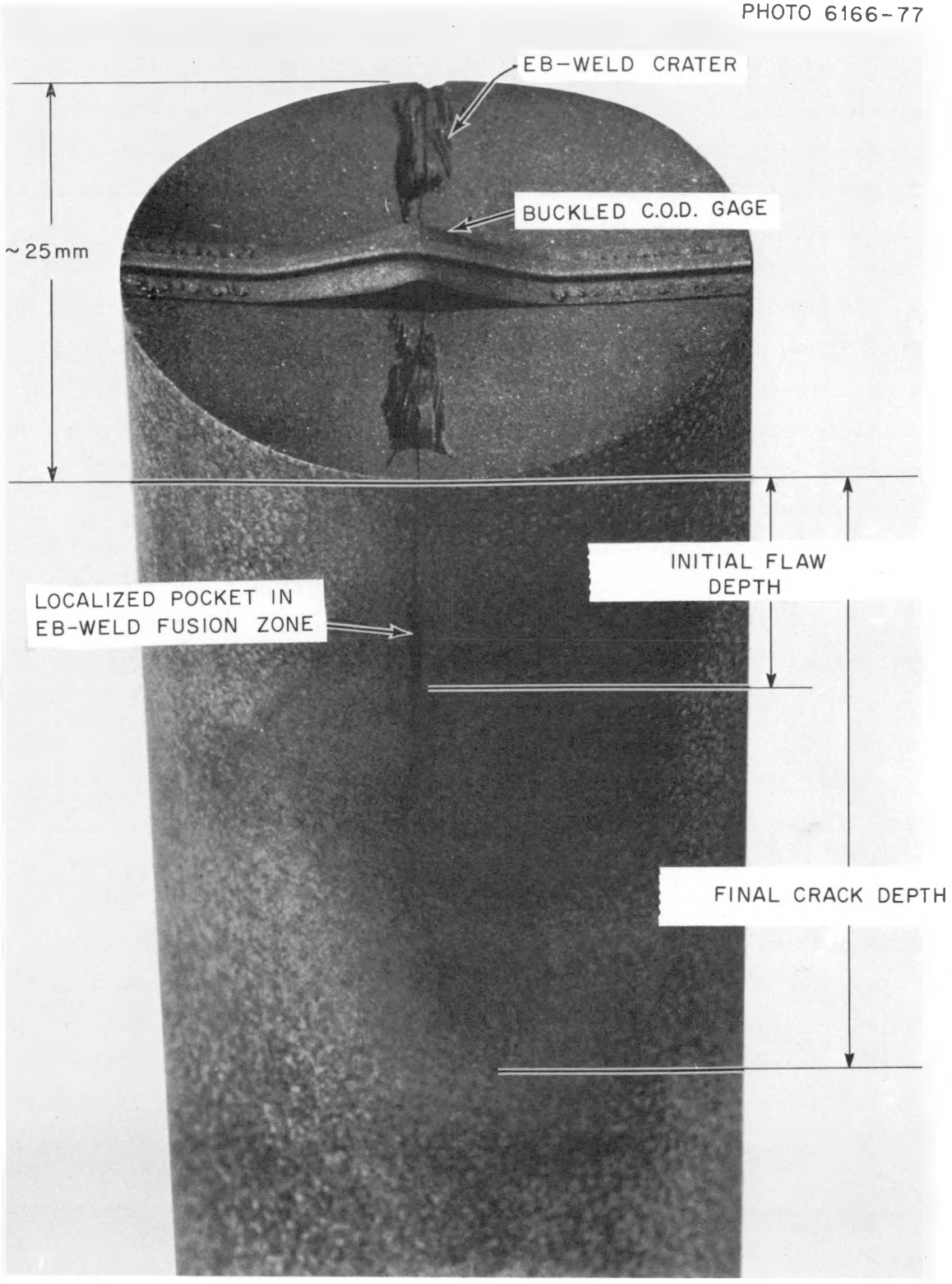

Fig. 6.4. Core trepanned from TSV-2 following TSE-4, showing initial and final crack depth and a buckled COD gage. Location at midlength of test specimen.

In order to permit examination of the fracture surfaces, three 26-mm-diam (∿1 in.) cores were trepanned from the flawed area following the thermal shock experiment. As shown in Fig. 6.5, the cores were taken from the central region of the test specimen close to COD gages XE-31, -32, and -33. The core closest to the center of the specimen was located directly under COD gage XE-32 and is shown in Fig. 6.4. A short section of the core containing the extended crack was removed from the rest of the core and split at cryogenic temperatures to reveal the fracture surfaces. These surfaces for the three cores are shown in Fig. 6.6. It was determined from an examination of these exposed surfaces that the initial fractional flaw depth was as expected (0.076) and that the final fractional crack depth was 0.15 to 0.17 in the central portion of the test specimen.

Calculations made using the measured transient temperature distributions (see Figs. 6.7 to 6.9 for typical distributions) and the nominal K_{Ic} vs T curve in Fig. 6.10 indicate a K ratio of ∿1.10 at 150 sec for a/w = 0.076. The fractional crack depth corresponding to a K ratio of 1.00 at 150 sec is ∿0.090, and the calculated time at which $K_I/K_{Ic} = 1$ for a/w = 0.076 is ∿125 sec. At 75 sec into the transient, the K ratio for a/w = 0.076 is ∿0.6 and the maximum K ratio at that time is ∿0.8, corresponding to $a/w \cong 0.03$.

The test specimen temperature corresponding to a/w = 0.076 and t = 150 sec is ∿74°C (165°F). At this temperature, a 10% variation in K_{Ic} corresponds to an 8°C (15°F) change in temperature. Everything considered, the accuracy of the temperature measurement is not much better than this. Thus, inaccuracies in temperature measurements could account for the apparent 10% "error" in the above calculated K ratio ($K_I/K_{Ic} = 1.10$ for a/w = 0.076 and t = 150 sec). However, it is more likely that most of the error is associated with the scatter in the K_{Ic} vs temperature data.

Before the three cores were removed from the test specimen, an indication of final crack depth was obtained by combining the COD output with the calculated (finite-element) crack openings for various crack depths. By this process the final fractional crack depth near the central portion of the test specimen was estimated to be 0.15, assuming an initial crack

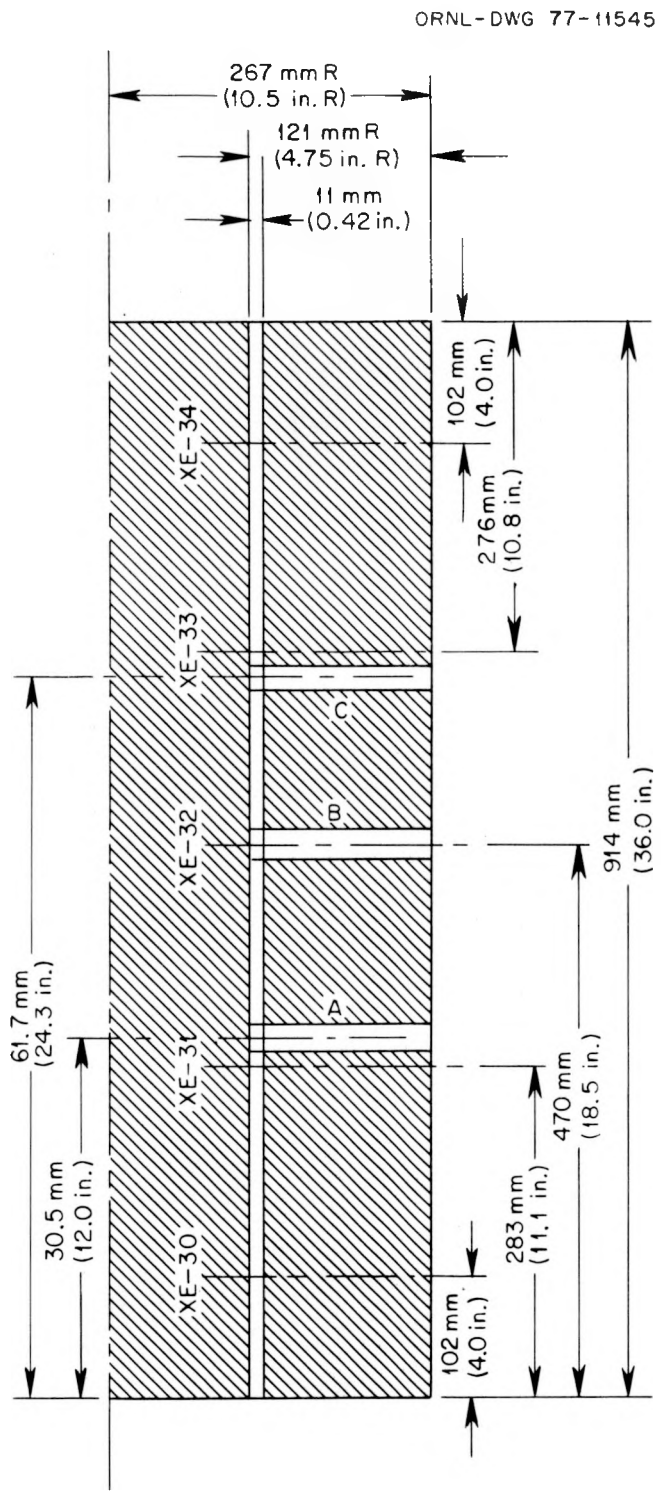

Fig. 6.5. Location of 26-mm-diam cores trepanned from TSV-2 following TSE-4.

PHOTO 6292-77

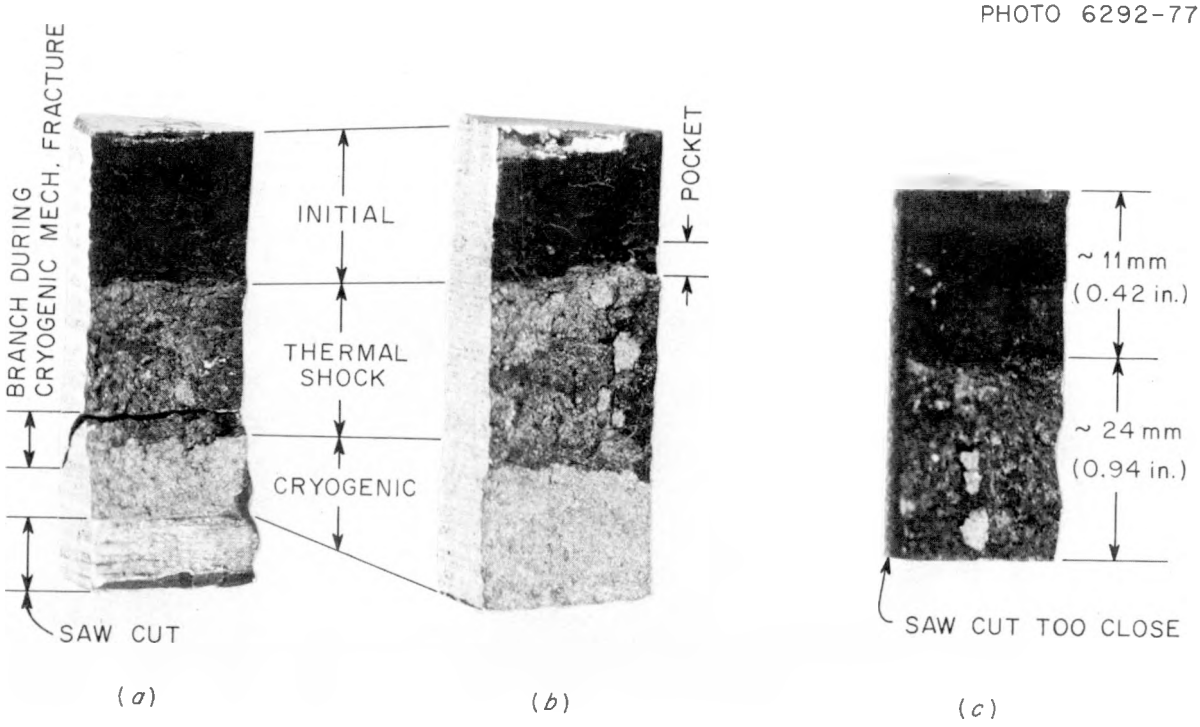

Fig. 6.6. Fracture surfaces revealed by splitting short sections of 26-mm-diam cores at cryogenic temperatures. Cores trepanned from TSV-2 following TSE-4. Refer to Fig. 6.5.

depth of 0.076. The total calculated crack opening from initiation of the transient to t $\cong$ 150 sec for a/w = 0.15 is 0.30 mm (12×10^{-3} in.), and the COD output also indicates a value of 0.30 mm without making corrections for thermal effects to the gages. The thermal effects are unknown but are believed to be relatively small.

Once the actual final crack depth was known, it was possible to obtain an estimate of the arrest toughness for a specific value of the temperature. For a/w = 0.15 and t = 150 sec, the temperature was 126°C (258°F) and K_I = 127 MN•m$^{-3/2}$(116 ksi $\sqrt{\text{in.}}$) = K_{Ia}. This value of K_{Ia} is about 25% greater than the value deduced from TSE-2.

Based upon these results and considering only nominal values of the various parameters involved, it would appear that the predictive methods of analysis used in connection with TSE-4 are quite accurate.

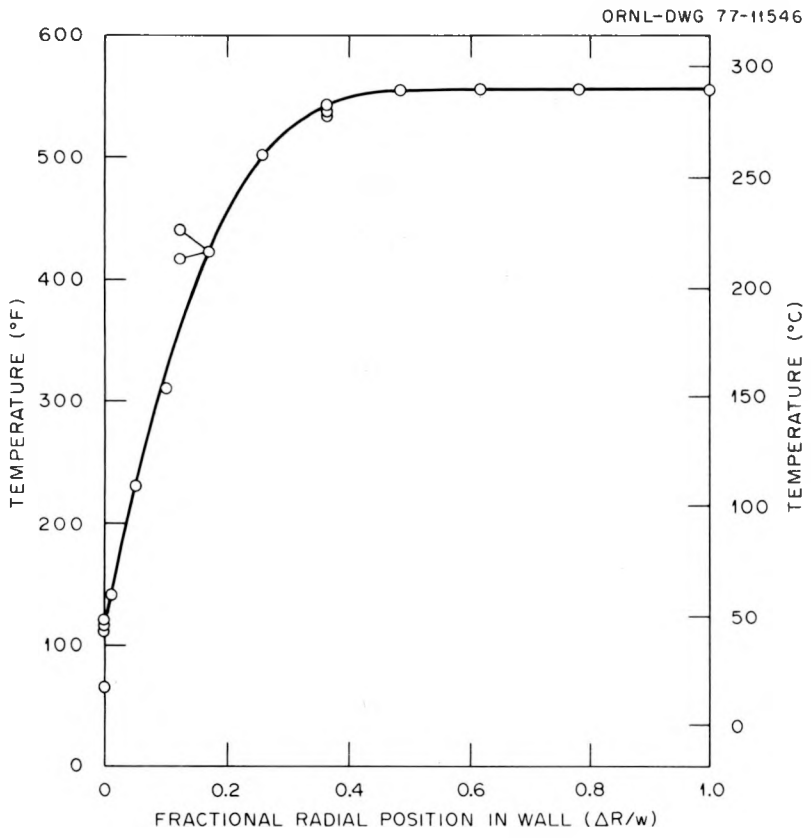

Fig. 6.7. Radial temperature distribution measured during TSE-4 at 40 sec into the transient.

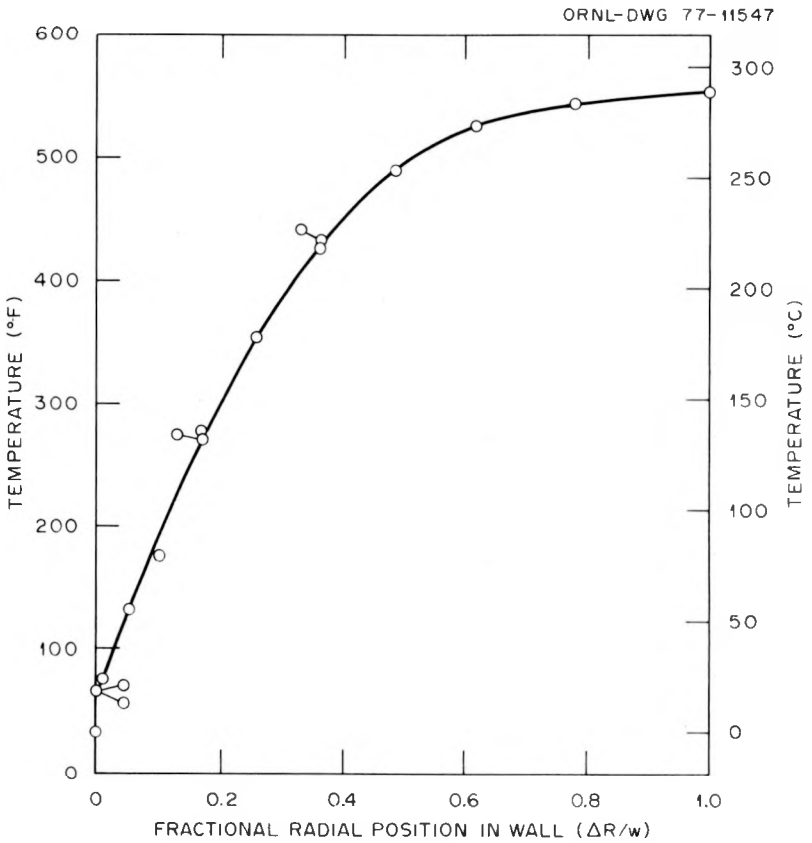

Fig. 6.8. Radial temperature distribution measured during TSE-4 at 162 sec into the transient.

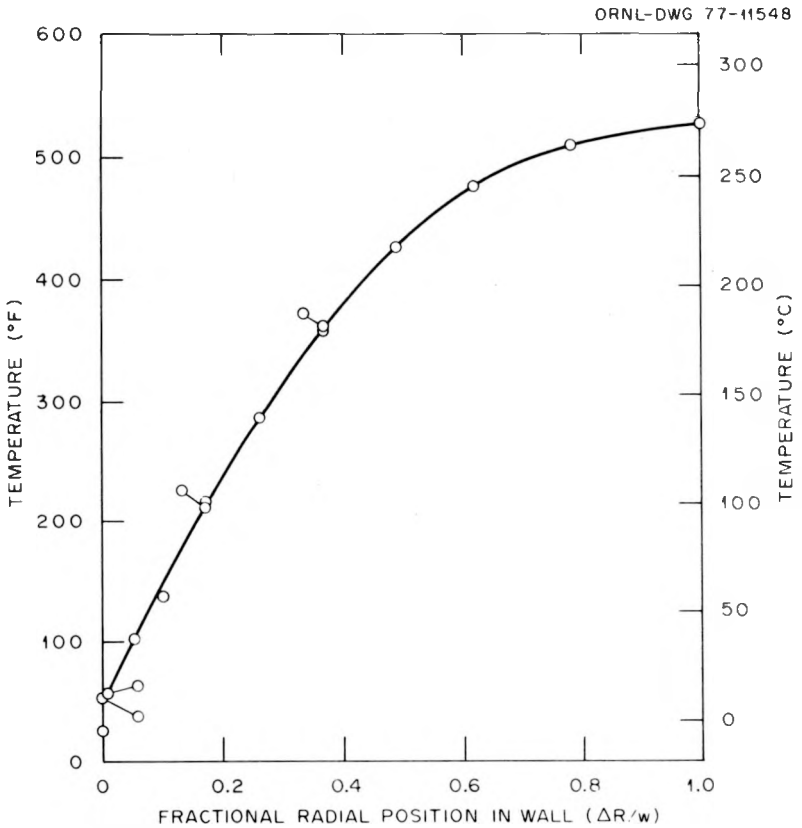

Fig. 6.9. Radial temperature distribution measured during TSE-4 at 302 sec into the transient.

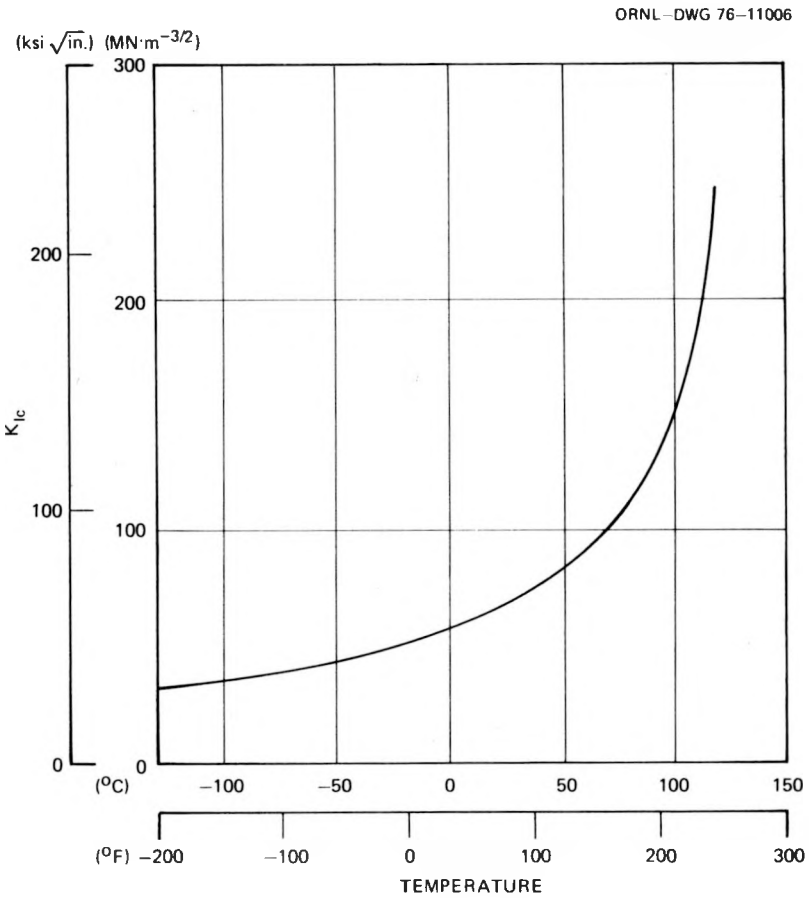

Fig. 6.10. Static fracture toughness curve used for analysis of 533-mm-OD (21-in.) thermal shock specimens TSV-1 and TSV-2. Curve based on data from A533, A508 (V-1 prolongation), and A508 (TSV-1 and TSV-2 prolongations), all in the as-quenched condition [quenched in water from 871°C (1600°F)].

6.3 Metallographic Examination of TSV-1 Thermal Shock Specimen Following TSE-3

D. A. Canonico R. S. Crouse

The third thermal shock experiment (TSE-3) was conducted with the same test specimen used in TSE-1, and the initial flaw for TSE-3 was the slightly extended flaw that existed following TSE-1. The thermal shock in TSE-3 was more severe than that in TSE-1 and resulted in additional crack extension. Based on the nature of the experiment and related calculations, it was tentatively concluded that the first extension was ductile (subcritical crack growth) and the second brittle.

Recent scanning electron microscopy (SEM) examinations of the TSE-1 and TSE-3 fracture surfaces have been completed. One specimen was removed from TSV-1 following TSE-3, and the results of the SEM examination confirmed the above conclusion. Additional proof regarding the fracture mode for TSE-1 was obtained by examining a cored specimen that had been removed from TSV-1 following TSE-1 and that had been mounted in epoxy for polishing and viewing of the crack line. This well-preserved specimen was demounted recently and the fracture surfaces were exposed by completing the fracture mechanically at cryogenic temperatures. A SEM examination revealed that the extension that took place during TSE-1 was ductile. These recent findings are contrary to SEM results reported earlier[2] which indicated brittle fracture. However, the fracture surfaces examined at that time were partially obscured by a protective film, and a final conclusion was deferred until the recent examinations could be completed.

The crack extension that occurred during TSE-3 was approximately 27 mm (1.1 in.) long. Figure 6.11 contains SEM photomicrographs of two regions representative of the fracture surface that developed during TSE-3. As indicated, the fracture surfaces are predominantly cleavage but with small regions that exhibit a dimple mode of fracture. Figure 6.12 contains a sequence of SEM photomicrographs of the area at increasingly higher magnifications. The purpose of this sequence is to confirm the presence of the small areas of ductile fracture in the predominately frangible (cleavage) fracture. These observations substantiate the irregular crack path observed in the light microscopy metallographic examinations of the cracks which showed regions where that crack was "bridged."

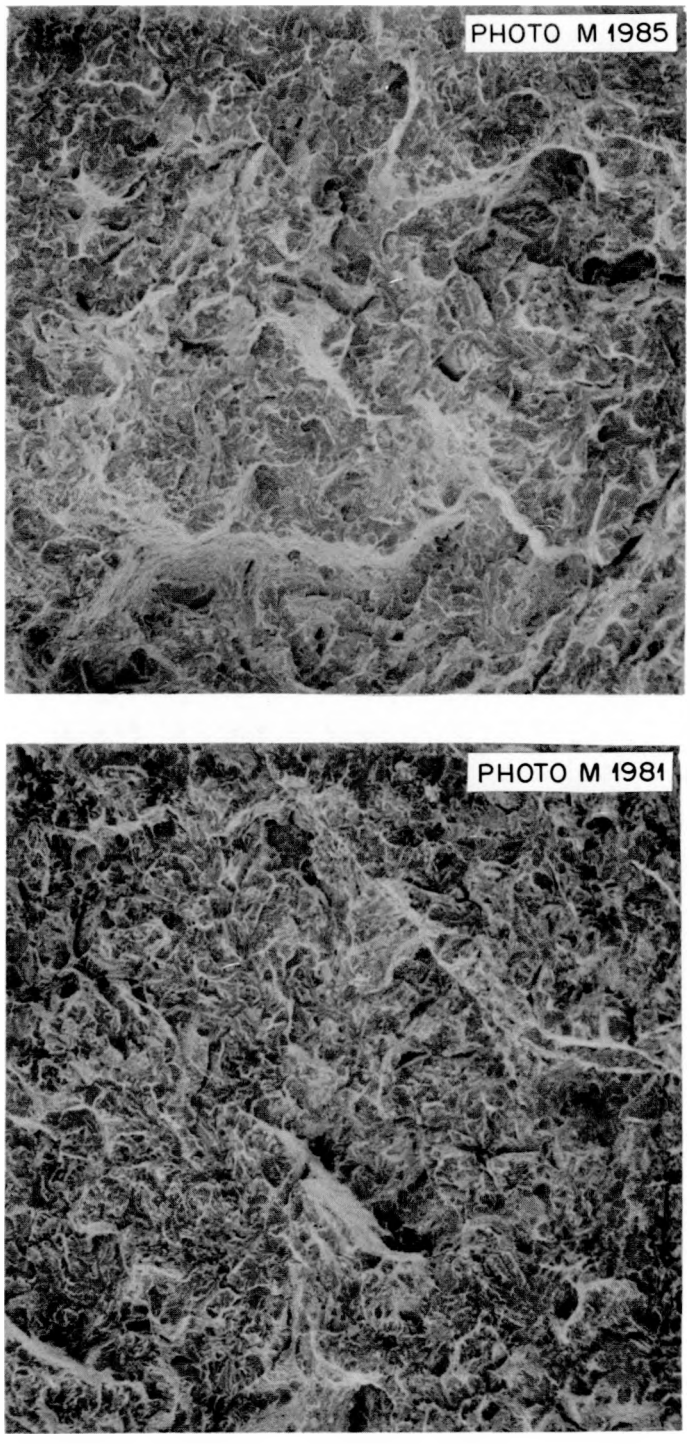

Fig. 6.11. Scanning electron microscopy photomicrographs of representative areas from the fracture surface that occurred as a consequence of TSE-3. The fracture exhibits a predominately cleavage mode with small areas of dimple fracture.

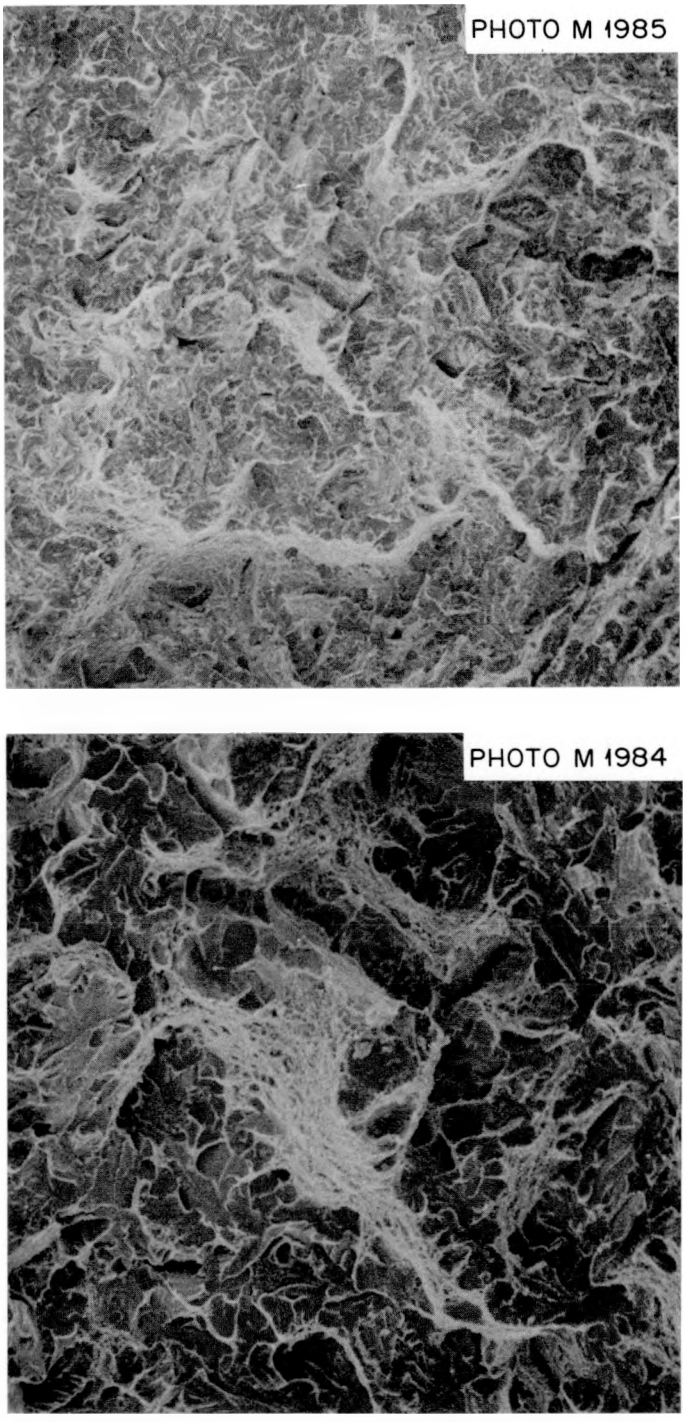

Fig. 6.12. Sequence of scanning electron photomicrographs of the same fracture area from TSE-3. The fracture surface exhibits a predominately cleavage mode of crack extension. The sequence confirms the presence of small areas of dimple fracture.

It is probably these "bridged" regions that exhibit the dimple mode of fracture.

6.4 Cryogenic Quenching

The results of a study[3] reported on previously indicate that warm prestressing cannot be adequately demonstrated in the present ORNL thermal shock test facility. A possible alternative thermal shock scheme that may produce the desired characteristics is to quench a cylindrical test specimen from near room temperature with liquid nitrogen. Under normal conditions, liquid nitrogen is not a very good quench medium for our purposes because a vapor blanket forms and prevents a rapid quench. However, experiments conducted by the French in connection with their LOCA-ECC thermal shock program indicate that the addition of a thin insulating layer to the surface will increase the overall heat transfer coefficient by a large factor. Presumably, the increase occurs because a large drop in temperature across the insulation tends to result in a much smaller temperature difference between the liquid nitrogen and the nitrogen-insulation interface. This reduction in temperature difference results in a shift from the vapor-blanket regime to the transitional-nucleate-boiling portion of the boiling curve (heat flux vs ΔT). In this latter regime the heat transfer coefficient is much greater than that corresponding to a vapor blanket. Also, the number of nucleation sites is important, and thus an insulating coating that provides a high density of nucleation sites will result in even higher heat transfer coefficients. The French included a number of insulating materials in their experiments and found 3M-brand spray adhesive 77 (Minnesota Mining and Mfg. Co.) to be the most effective.

Thus far, the French heat transfer experiments have been limited to an initial temperature of 30°C and to specimen geometries that may not properly simulate pressure vessel thermal-hydraulic conditions. Since the French results looked promising, we initiated our own cryogenic-quench heat transfer experimental program and are covering a broad range of parameters so as to obtain data that are directly applicable to the demonstration of warm prestressing in one of our 991-mm-OD (39-in.) thermal shock test specimens.

Prior to launching the cryogenic experimental program, fracture mechanics calculations were made for the 991-mm-OD specimens using cryogenic-quench-enhanced heat transfer coefficients obtained by the French. The purpose was to determine whether suitable conditions could be achieved for demonstrating warm prestressing. The calculations were made for a long axial flaw using an initial temperature of 30°C, consistent with the French data, and the heat transfer coefficient vs surface temperature curve shown in Fig. 6.13. Results in terms of K_I vs time for several values of fractional crack depth (a/w) are shown in Fig. 6.14. Included

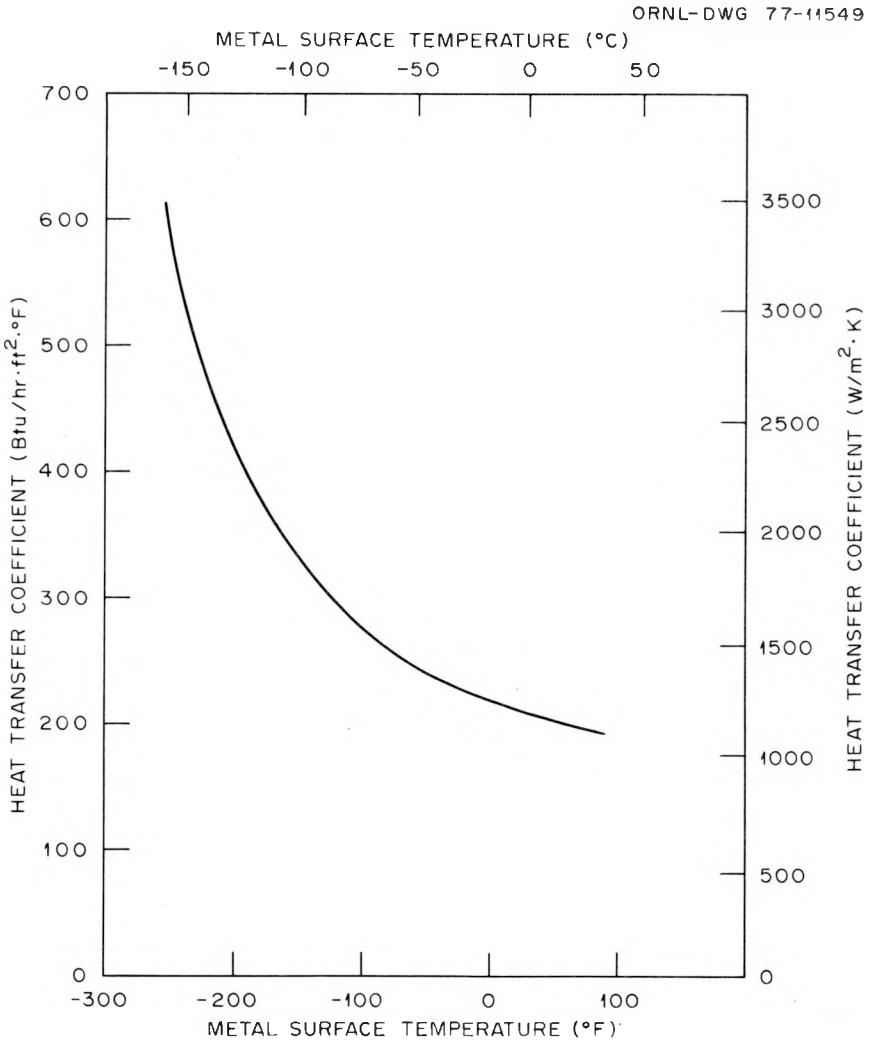

Fig. 6.13. Heat transfer coefficient for 13-mm-diam (0.5-in.) rod with coating of 3M-brand spray 77 when quenched in liquid nitrogen from 30°C (French data).

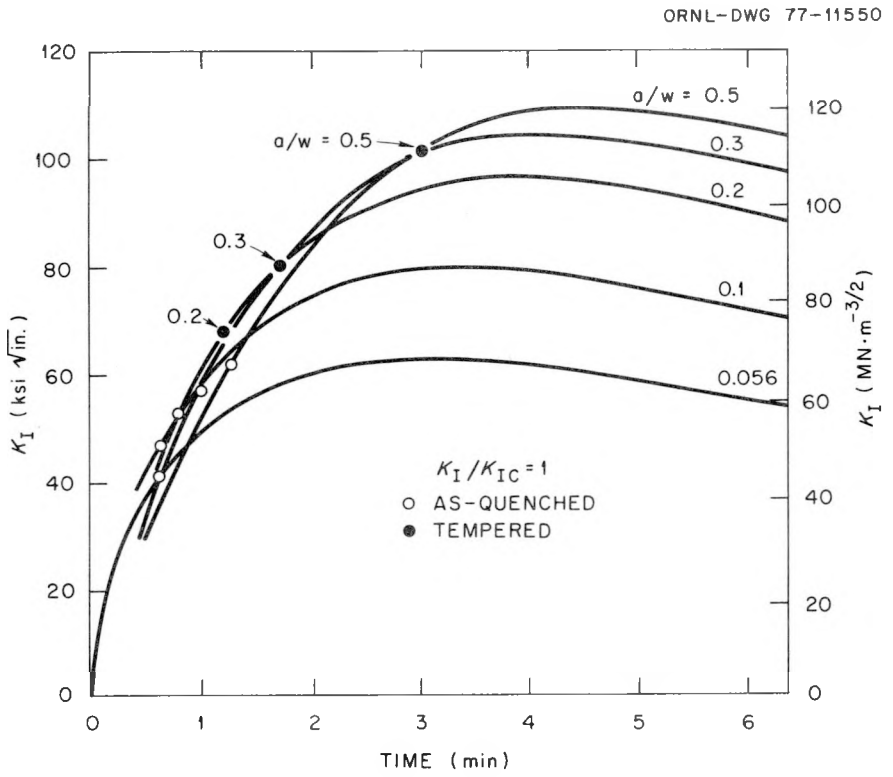

Fig. 6.14. Stress-intensity factor for a long axial flaw in the 991-mm-OD × 686-mm-ID (39-in. × 27-in.) test specimen when subjected to liquid nitrogen quench with T_i = 30°C (based on French heat transfer coefficient data).

on these curves are the points for K_I/K_{Ic} = 1 corresponding to both tempered material and quench-only material. It is observed that warm prestressing does not take place because, even for the tempered material, temperatures are too low too soon.

The above results imply that a higher initial temperature may result in warm prestressing. A higher temperature will affect the heat transfer coefficient and will also reduce the K ratio (K_I/K_{Ic}), which tends to reduce the chances of an adequate demonstration of warm prestressing. However, as shown in Table 6.3, the maximum K ratios achieved with an initial temperature of 30°C are high enough to permit some reduction.

Two factors being considered in our cryogenic-quench experimental program that were not included in the French studies are the effects of initial temperature and hydrodynamics on the heat transfer coefficient. The first set of our experiments was performed with a 13-mm-diam steel

rod similar to that used by the French. Two different insulating materials were used: rubber cement (American Writing Ink Co., Spec. 8040-291-8625) and 3M-brand spray adhesive 77. Typical quench curves for a clean specimen and for the same specimen with different thicknesses of the two coatings are shown in Fig. 6.15. As indicated, the coatings reduced the quenching time by a factor as large as 5. Spray 77 is more

Table 6.3. Maximum K ratios obtained for tempered and quenched-only material during cryogenic quench (long axial flow, t_0 = 30°C)

a/w	$(K_I/K_{Ic})_{max}$	
	Tempered	Quenched only
0.056	1.5	2.2
0.10	1.9	2.6
0.20	2.1	3.0
0.30	2.2	2.9
0.50	1.9	2.5

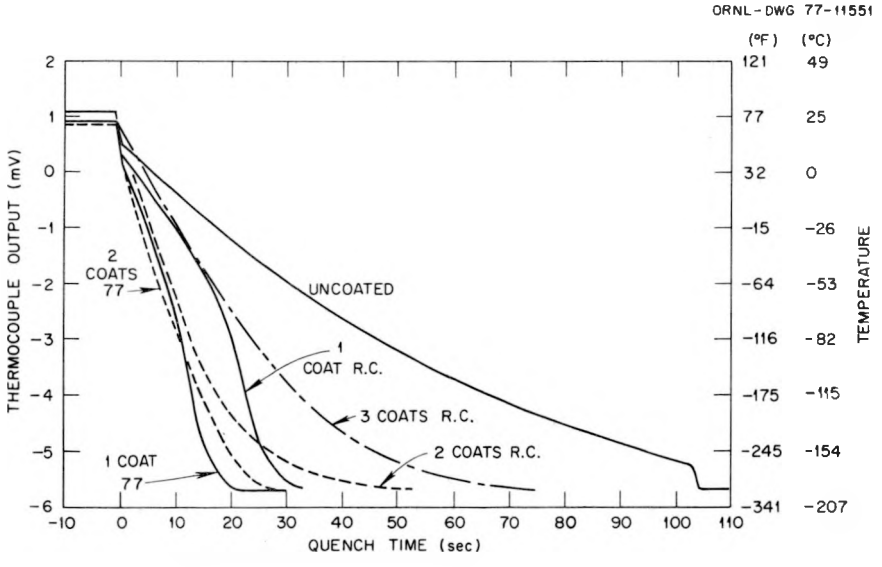

Fig. 6.15. Indicated metal surface temperatures during liquid nitrogen quench of 13-mm-diam (0.5-in.) rod with various coatings.

effective than the rubber cement and, as would be expected, there is an optimum thickness. Although not shown in Fig. 6.15, the shortest quench time achieved by optimizing the thickness of spray 77 was about 10 sec.

Some of the characteristics of the quench curves are of interest. When a specimen is initially submerged in liquid nitrogen, liquid contacts the surface until the vapor blanket or some transitional nucleate boiling regime has been established. During this initial time period, the heat transfer coefficient is quite large, as indicated by the sudden drop in surface temperature. For the uncoated specimen, a vapor blanket is established and remains until the superheat decreases to about 22 K (40°F), whereupon nucleate boiling once again results in a sudden quench. In the case of the coated specimen, following the initial fast quench, transitional nucleate boiling is in existence from the outset and the knee in the curve moves up the curve with increasing coating thickness. The rate of cooling below the knee corresponds to fully developed nucleate boiling but is reduced as the thickness of the insulating coating increases.

The next step in the experimental program was to investigate the effect of elevated initial temperatures, using the same coating materials and the 13-mm-diam (0.5-in.) specimen. The results are shown in Figs. 6.16 and 6.17 for rubber-cement and spray 77 coatings, respectively. Increasing the initial temperature results in essentially no change in the heat transfer coefficient for the rubber cement, but there appears to be some reduction for spray 77. Changes in the coefficients are deduced from a comparison of slopes of the temperature vs time curves at specific surface temperatures.

To achieve hydrodynamic conditions that more nearly simulate those that would occur in the thermal shock test specimens [991 mm OD (39 in.) × 686 mm ID (27 in.) × 1.37 m long (54 in.)], cryogenic-quench tests were conducted next with a cylindrical test specimen [146 mm ID (5.75 in.), 168 mm OD (6.625 in.), 152 mm long (6.0 in.)] quenched on the inner surface and insulated on the outer surface. The specimen was suspended in a tank of liquid nitrogen so that a convective loop up through the middle and down the outside would be established. The apparatus is shown schematically in Fig. 6.18.

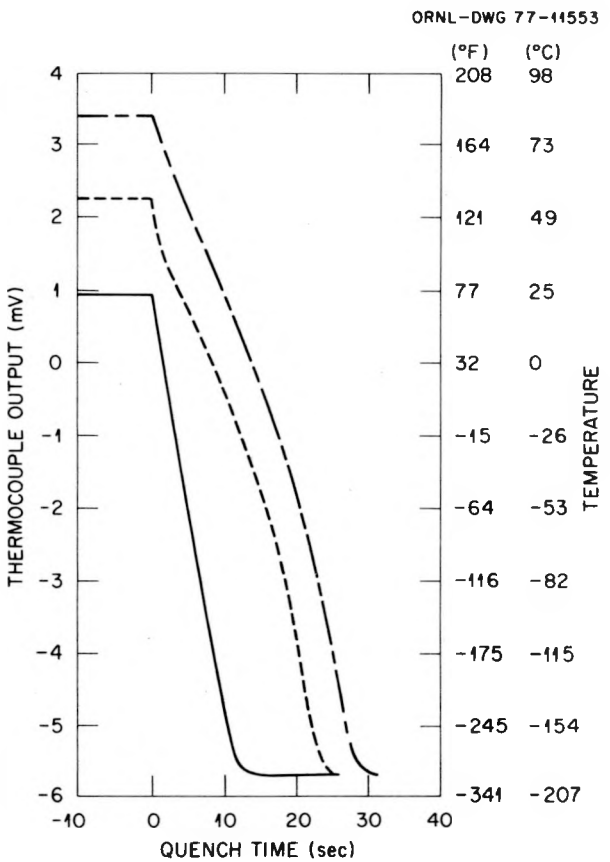

Fig. 6.16. Indicated metal surface temperature vs quench time for 13-mm-diam rod (0.5-in.) specimen with one and two coats of rubber cement using different initial temperatures.

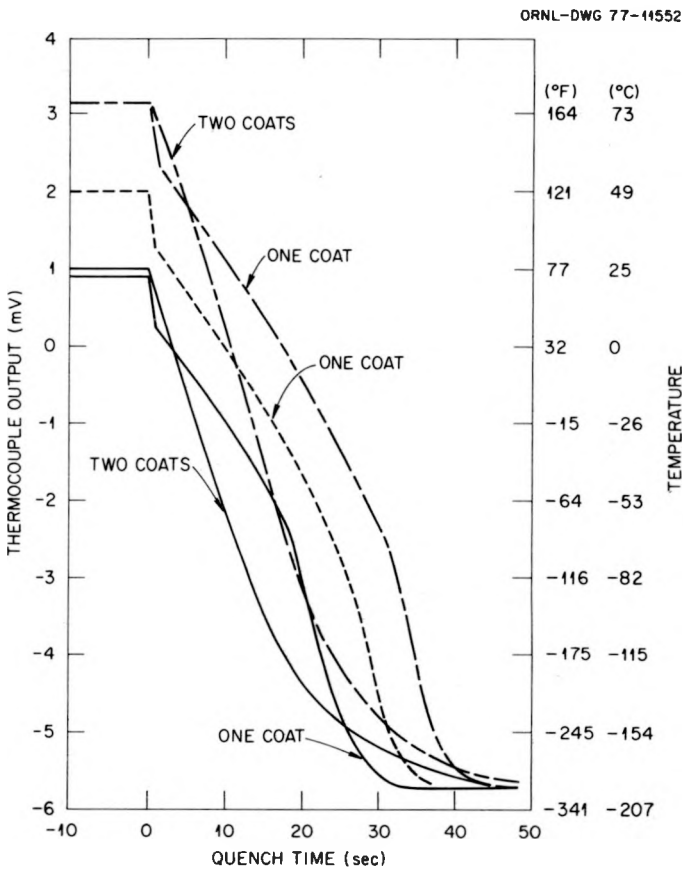

Fig. 6.17. Indicated metal surface temperature vs quench time for 13-mm-diam-rod (0.5-in.) specimen with two coats of 3M-brand spray 77 using different initial temperatures.

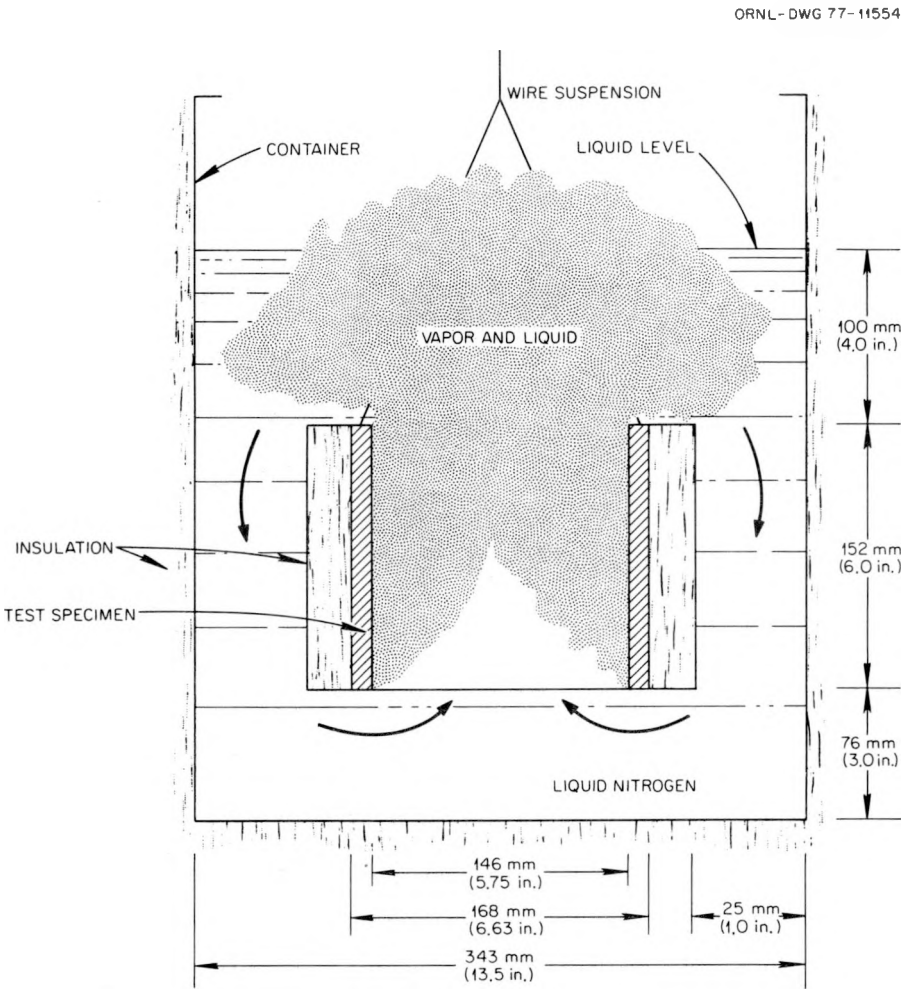

Fig. 6.18. System used for quenching 150-mm cylindrical specimen in liquid nitrogen.

Temperature-time results obtained with the 150-mm (6-in.) specimen are shown in Fig. 6.19 for various surface conditions and initial temperatures. It may be observed that, even under film blanketing conditions (uncoated surface), the surface finish has an appreciable effect on quench time. Spray 77 was applied to the smooth surface, and two coats reduced the quench time by a factor of 8. Tests were conducted with initial temperatures of ∿24°C (75°F) and ∿66°C (150°F); as indicated by a comparison of the slopes of the curves, there is not much difference in the heat transfer coefficients.

After a number of preliminary experiments were conducted, additional thermocouples were added to the 150-mm (6-in.) test specimen. These were

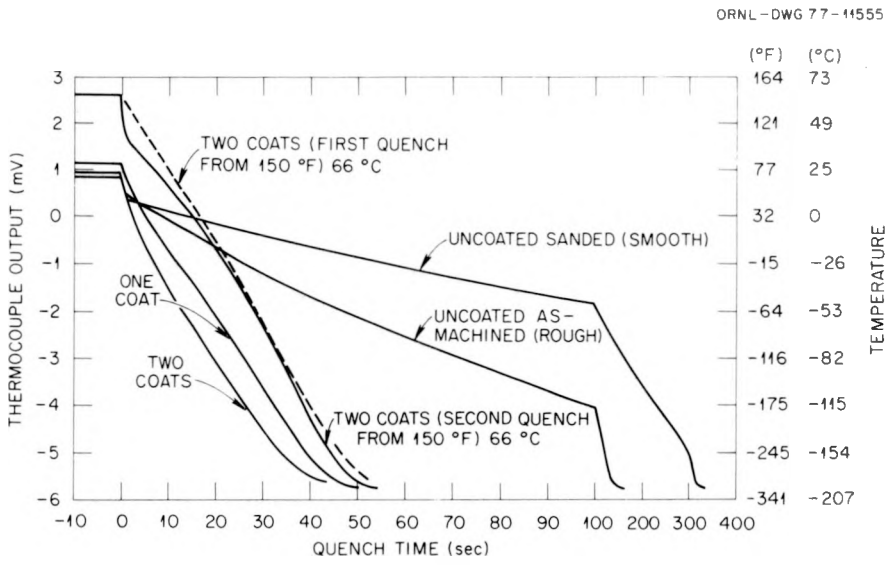

Fig. 6.19. Indicated metal surface temperature vs quench time for 146-mm-ID × 168-mm-OD × 152-mm-long (5.75-in.-ID × 6.625-in.-OD × 6-in.-long) cylinder quenched on inner surface with liquid nitrogen. Surface bare or coated with 3M-brand spray 77.

located in the wall close to the inner surface so that the instantaneous heat flux and metal surface temperature could be obtained by extrapolation. With this information the heat transfer coefficient as a function of metal surface temperature could be determined from

$$h = \frac{k(dT/dr)_{a=0}}{T_s + 196°C} ,$$

where

h = combined heat transfer coefficient for fluid film and coating,

k = thermal conductivity of specimen material,

$(dT/dr)_{a=0}$ = slope of temperature vs radius curve at inner surface,

T_s = metal surface temperature (°C).

The surface temperature must be obtained by extrapolation because actual surface temperature measurements during a transient are not very reliable, particularly under liquid nitrogen quenching conditions.

Heat transfer coefficients obtained from the 150-mm cylinder liquid nitrogen quench tests are shown in Fig. 6.20. As indicated, there is

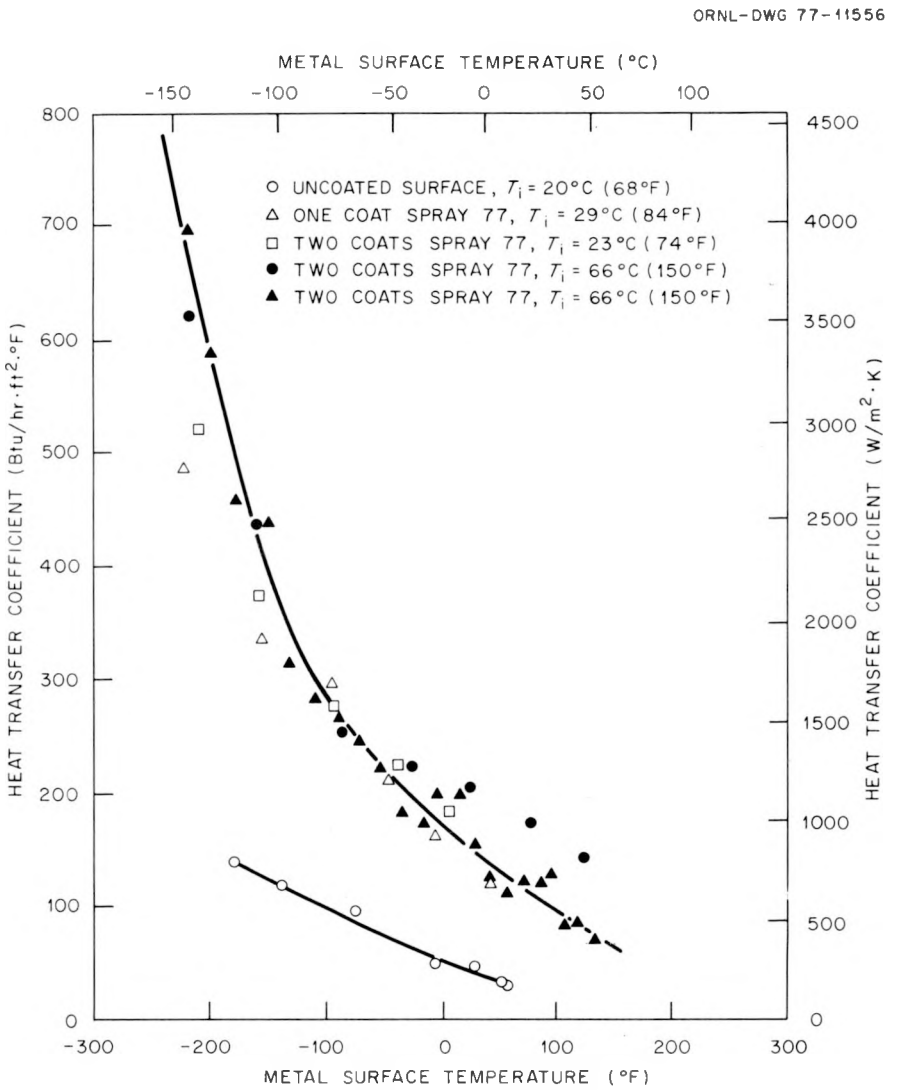

Fig. 6.20. Heat transfer coefficients determined with 150- × 150-mm cylinder when inner surface is quenched in liquid nitrogen.

an increase in coefficient with decreasing metal surface temperature, and it is much more pronounced with the surface coated. It is also observed that for a given surface temperature the coefficients corresponding to initial temperatures of 23°C (74°F) and 66°C (150°F) are essentially the same, although in one high-temperature run the coefficients for the higher temperature end of the curve were somewhat higher.

The above heat transfer coefficient curve corresponding to an initial temperature of 66°C (150°F) will be used in a fracture mechanics

calculation to determine if warm prestressing can be demonstrated in the 991-mm-OD (39-in.) test specimen under cryogenic-quench conditions.

6.5 Implementation of Procedures for Calculating Stress-Intensity Factors for Three-Dimensional Problems

S. K. Iskander

In the two-dimensional studies previously reported,[4] the computational algorithm relied on the strain energy release rate concept. The calculation of stress-intensity factors for three-dimensional problems is considerably more complicated. Apart from the difficulties in generating a sufficiently fine mesh in the crack region, the stress-intensity factor is now a function of position on the crack front.

The problem of computational efficiency is of prime importance. Of the many methods reported in the literature recently, those based upon singular integral equations,[5] special crack tip elements,[6-10] influence function methods,[11] and refined energy release-rate methods combined with special crack-tip elements[12] are notable.

One of the special crack tip elements[9,10] is particularly useful in that it can be simply evolved from any quadratic isoparametric element. By placing the "midside" nodes at the one-quarter point adjacent to the crack front, a $1/\sqrt{r}$ singularity in the stresses is simulated.

In order to evaluate this element, the ADINA code[13] has been used. There are several areas that need to be explored. The minimum level of mesh refinement to give reasonably accurate results needs to be established. Other items that also need study are methods for calculating K_I from the results and the optimum number of Gaussian integration points. Wedge-shaped elements also appear to give better results than brick-shaped ones.[14]

Many of these questions can be partially resolved on the two-dimensional level at greatly reduced costs by solving problems with known solutions. A centrally cracked strip with an a/w = 0.10 and a length-to-width ratio of 3 has been analyzed using the mesh shown in Fig. 6.21. There are 14 elements in the model. The displacement method[15] for extracting K_I has been used. As Henshell[9] notes, although the singularity

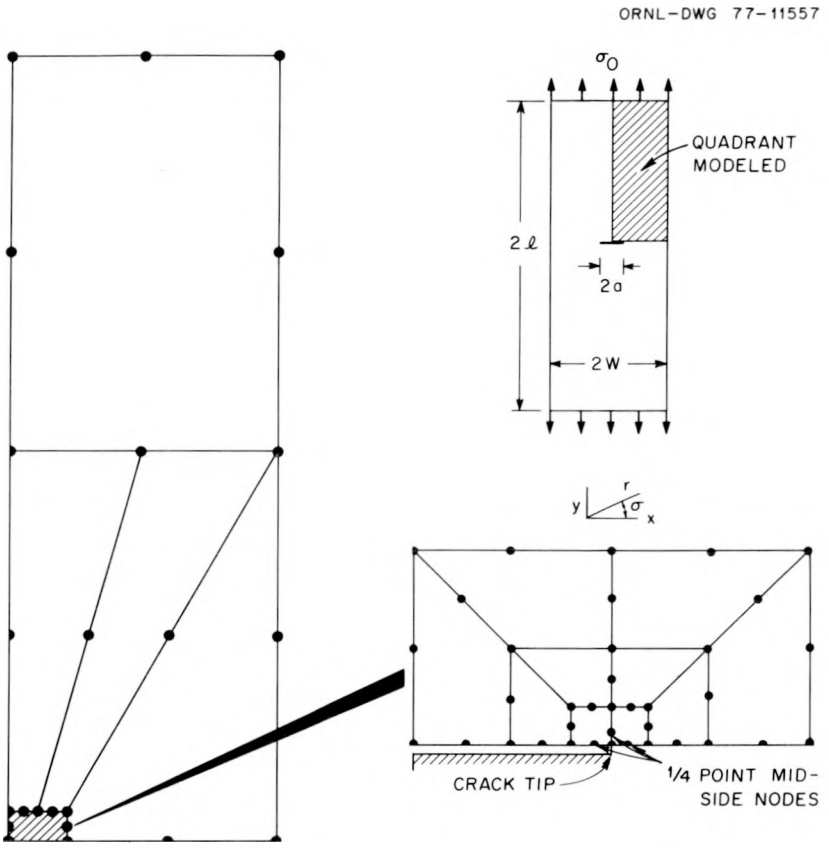

Fig. 6.21. Finite-element idealization for a centrally cracked strip.

element has the correct stiffness, the displacement of the 1/4 point midside node is inaccurate and hence may be neglected. (This node is at r/a = 0.05 in Fig. 6.22.) Figure 6.22 shows the estimates of the stress-intensity factor K_I^* obtained as follows. The plane strain expressions for the displacements[16] are given by

$$u = \frac{K_I}{G}\left(\frac{r}{2\pi}\right)^{1/2} \cos\frac{\theta}{2}\left[1 - 2\nu + \sin^2\frac{\theta}{2}\right]$$

$$v = \frac{K_I}{G}\left(\frac{r}{2\pi}\right)^{1/2} \sin\frac{\theta}{2}\left[2(1 - \nu) - \cos^2\frac{\theta}{2}\right]$$

with the higher order terms neglected. The u and v are the displacements in the x and y directions, r and θ are local polar coordinates with the origin at the crack tip, and G and ν are the modulus of rigidity and Poisson's ratio, respectively. If v* is the nodal displacement on

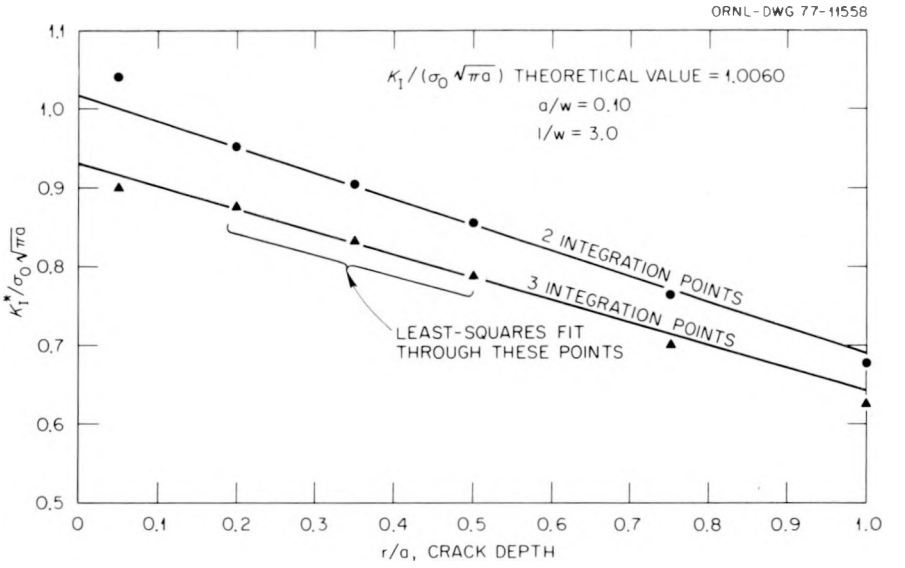

Fig. 6.22. Estimates of K_I^* as calculated from nodal displacements.

the free surface of the crack and normal to it, an estimate for the stress-intensity factor K_I^* for a plane strain solution is given by

$$K_I^* = \frac{Ev^*}{4(1-\nu^2)} \sqrt{\frac{2\pi}{r}} ,$$

where E is Young's modulus.

It may be noted from Fig. 6.22 that the estimate of K_I^* for two integration points is about 2% greater than the theoretical value.[17] This is noteworthy since finite-element K_I^* estimates are usually lower than the theoretical values. Indeed when the number of Gaussian integration points was increased to three, the estimate for K_I did decrease and was about 7% lower than the theoretical value. Whether the more accurate but higher values with two integration points are actually a characteristic of the integration scheme can only be determined by mesh-refinement-type convergence studies.

A side benefit of implementing efficient two-dimensional methods with the aim of extending them to three-dimensional problems is that they may find applicability in the ongoing two-dimensional studies.

Within the scope of this effort, mesh generation computer programs that interactively display their results are of importance and are being

studied. These could be developed locally. However, attempts are being made to acquire existing codes, and if these attempts are successful, the codes will be implemented and used.

References

1. R. D. Cheverton and S. E. Bolt, "Development of Improved COD Gage Installation," *Heavy-Section Steel Technology Program Quart. Prog. Rep. July–September 1976*, ORNL/NUREG/TM-64, pp. 94–97.
2. D. A. Canonico, "Posttest Examination of Flawed Area in TSV-1 and -2," *Heavy-Section Steel Technology Program Quart. Prog. Rep. April–June 1976*, ORNL/NUREG/TM-49, pp. 87–104.
3. R. D. Cheverton and S. E. Bolt, "Warm Prestressing," *Heavy-Section Steel Technology Program Quart. Prog. Rep. July–September 1976*, ORNL/NUREG/TM-64, pp. 85–89.
4. S. K. Iskander, *The Calculation of Stress Intensity Factors in Thick Cylinders Subjected to Transient Temperature Gradients by the Finite Element Method*, K/CSD/TM-2.
5. T. A. Cruse and W. VanBuren, "Three-Dimensional Elastic Stress Analysis of a Fractured Specimen with an Edge Crack," *Int. J. Fract. Mech.* 7 (1) (March 1971).
6. W. S. Blackburn, "Calculation of Stress Intensity Factors at Crack Tips Using Special Finite Elements," *The Mathematics of Finite Elements and Applications* (Ed. by J. Whitman), pp. 327–36, Brunel University, 1973.
7. D. M. Tracey, "Finite Elements for Determination of Crack Tip Elastic Stress Intensity Factors," *Eng. Fract. Mech.* 3, 255-66 (1971).
8. T. H. H. Pian, P. Tong, and C. H. Luk, "Elastic Crack Analysis by a Finite Element Hybrid Method," *Proceedings of 3rd Conference on Matrix Methods in Structural Mechanics*, Wright-Patterson AFB, Ohio, 1971.
9. R. D. Henshell and K. G. Shaw, "Crack Tip Finite Elements Are Unnecessary," *Int. J. Num. Meth. Eng.* 9, 495–507 (1975).
10. R. S. Barsoum, "On the Use of Isoparametric Finite Elements in Linear Fracture Mechanics," *Int. J. Num. Meth. Eng.* 10, 25–37 (1976).
11. P. M. Besuner and W. R. Caughey, *Comparison of Finite Element and Influence Function Methods for Three-Dimensional Elastic Analysis of Boiling Water Reactor Feedwater Nozzle Cracks*, Electric Power Research Institute Report NP-261 (November 1976).
12. T. K. Hellen, "On the Method of Virtual Crack Extensions," *Int. J. Num. Meth. Eng.* 9, 187–207 (1975).

13. Klaus-Jürgen Bathe, *ADINA — A Finite Element Program for Automatic Dynamic Incremental Nonlinear Analysis*, Report 82448-1, Acoustics and Vibration Laboratory, Mechanical Engineering Dept., MIT, Cambridge, Mass. 02139.

14. H. D. Hibbit, "Some Properties of Singular Isoparametric Elements," *Int. J. Num. Meth. Eng.* 11, 180–84 (1977).

15. S. K. Chan, I. S. Tuba, and W. K. Wilson, "On the Finite Element Method in Linear Fracture Mechanics," *Eng. Fract. Mech.* 2, 1–17 (1970).

16. G. S. Sih and H. Liebowitz, "Mathematical Theories of Brittle Fracture," *Fracture*, Vol. II, Academic Press, 1968.

17. M. Isida, "Effect of Width and Length on Stress Intensity Factors of Internally Cracked Plates Under Various Boundary Conditions," *Int. J. Fract. Mech.* 7, 301–16 (1971).

7. FOREIGN RESEARCH

W. L. Greenstreet

The objective of this task is to systematically collect, maintain, and review products of foreign research that are applicable to safety of LWR primary systems. The areas to be covered are fracture mechanics, metallurgy, welding, and structures fabrication. The validity and usefulness of foreign results for application to safety and licensing of LWRs are to be identified to NRC, and recommendations are to be made concerning the application of pertinent well-founded research results.

The thrust of this activity during this period has been on identification of research reports and programs on the topics listed, identification of reports and programs with organizations in each of the countries, acquisition of original language and English versions of reports potentially of direct interest to staff members, and establishing a review process. Since foreign research reports acquired under Office of Nuclear Regulatory Research exchange agreements are reported to the Nuclear Safety Information Center (NSIC) and listed in the journal *Nuclear Safety*, a listing of reports on topics of interest was compiled from Vol. 16, No. 3, through Vol. 18, No. 1; the reports were cataloged by organization and country. A second listing taken from Vol. 18, No. 2 and Vol. 18, No. 3 is being assembled.

Acquisition of original language copies is being handled through NSIC and the ORNL Central Research Library. Translated copy acquisition procedures are not established. We currently are working with A. Spano's office in an attempt to obtain English language copies of reports already translated and to obtain translation services when additional work is needed. Obtaining translated copies of the reports selected without long delays is one of the most important aspects of this activity.

The lists of reports obtained from *Nuclear Safety* are screened and subsequently reduced through review by HSST staff members. Staff members are to study the reports selected to achieve the objectives described in the first paragraph of this chapter.

To provide an overview and coherence for the foreign research activity, a copy of the report, *OECD, Nuclear Energy Agency — International*

Energy Agency, Nuclear Safety Research Index, 1976, was obtained, and projects of interest in the metallurgy and materials area were identified. These are being cataloged according to country and subject category (different for that used in the OECD report), and summaries are being assembled. Once the cataloging and compilation is completed, this material will be distributed to participating members as well as updated as new information becomes available.

8. PCRV TENDON CORROSION STUDIES

J. C. Griess J. H. DeVan
D. A. Canonico

High-strength steels are being used as tendons in prestressed concrete structures. The usual procedure is to string tendons made of several steel wires through channels in the concrete and, after tensioning the tendons to the desired level, pump a concrete grout or grease into the channels containing the tendons to inhibit corrosion. Since highly stressed high-strength steels are very susceptible to cracking in the presence of certain ions, the question arises as to what level of impurities in the grouts and greases can obtain without resulting in excessive corrosion or cracking of the steel. Some of the preliminary results obtained in an attempt to determine an answer to this question are described below.

For the tests described here, the center straight wire of a seven-wire tendon made from cold-worked 1080 steel and conforming to ASTM A416 grade 270 was used. The diameter of the wire was 5.0 mm (0.20 in.), and for the present tests the surface of the wire was used as received except surface rust was removed with fine emery paper. The wire in the presence of the test environment was strained at a very slow constant rate in a tensile machine. The length between the grips was 200 mm (8 in.), but only the center 75-mm (3-in.) length was exposed to the corrosive solution, which was held in a polyvinylchloride container. Except in two tests, no attempt was made to control the potential of the wire relative to its environment; that is, the tests were carried out at the corrosion potential.

The results obtained in tests to date are summarized in Table 8.1. Of the environments tested, only 0.2*M* NH_4NO_3 at 66 and 52°C (150 and 125°F) and sulfide at room temperature and pH values of 4 or less produced cracks. In tests 13 and 14, the potential of the specimen was controlled at −0.440 to −0.430 V with reference to the saturated calomel electrode (SCE); no cracking was found, although enhanced general corrosion occurred. In the tests with very low sulfide content (tests 20 and 21), atmospheric oxygen probably oxidized all the H_2S to elemental

Table 8.1. Summary of constant-strain-rate cracking tests with hardened 1080 carbon steel

Test No.	Temp. (°C)	Test medium	pH start/finish	Strain rate (10^{-5} per minute)	Time to break (hr)	Load [N (kg)]	Cracks
1	21	Air		640		39,100 (3990)	
5	21	Air		2.46	55.5	42,000 (4280)	
6	21	0.2*M* NH_4NO_3	5.0/7.0	2.46	57.5	40,200 (4100)	No
7	66	0.2*M* NH_4NO_3	5.0/7.4	2.46	50.5	38,900 (3970)	Yes
8	66	0.2*M* NH_4NO_3	5.0/7.0	24.6	5.2	38,700 (3950)	Yes
9	66	0.01*M* KCl	5.3/6.3	2.46	60.8	38,900 (3970)	No
10	52	0.2*M* NH_4NO_3	5.3/7.3	2.46	49.5	38,900 (3970)	Yes
11	38	0.2*M* NH_4NO_3	5.3/7.7	2.46	47.0	39,000 (3980)	No
12	21	0.2*M* NH_4NO_3	5.3/7.0	2.46	66.6	39,300 (4010)	No
13[a]	21	0.2*M* NH_4NO_3	5.4/8.0	2.46	44.3	35,800 (3650)	No
14[a]	21	0.2*M* NH_4NO_3	9.4	2.46	55.5	39,500 (4030)	No
15	21	0.01*M* KCl + CaO	11.9/11.5	2.46	55.3	39,200 (4000)	No
16	21	HCl + 0.1*M* H_2S	3.0	2.46	6.6	15,000 (1530)	Yes
17	21	H_2O + 0.1*M* H_2S	∿4	2.46	4.7	11,100 (1130)	Yes
18	21	$10^{-3}M$ Na_2S	11.1/11.2	2.46	57.8	38,400 (3920)	No
19	21	$10^{-3}M$ Na_2S + HCl	7.4/7.7	2.46	53.8	39,100 (3990)	No
20	21	$3 \times 10^{-4}M$ Na_2S + HCl	6.3	2.46	52.0	39,300 (4010)	No
21	21	$3 \times 10^{-4}M$ Na_2S + HCl	4.3	2.46	54.8	39,300 (4010)	No
22	21	$10^{-3}M$ Na_2S + HCl	4.3/6.0	2.46	19.3	35,300 (3600)	Yes
23	21	$3 \times 10^{-3}M$ Na_2S + HCl	4.3/7.4	2.46	17.0	34,200 (3490)	Yes

[a]Specimen held at potential of −0.440 to −0.430 V vs SCE.

sulfur early in the test; even in the last two tests (22 and 23), the amount of H_2S in solution undoubtedly decreased significantly.

An ∿25-mm (1-in.) length of each wire, including one failed end, was metallographically mounted along the axis to look for small cracks originating on the surface exposed to the solution. In tests 7, 8, and 10, where cracking was indicated, the depths of the cracks were so small relative to the diameter of the wire that they produced no noticeable effect on either the time to failure or the load at failure (Table 8.1). The nature of the cracks produced in 0.2*M* NH_4NO_3 at 66 and 52°C and the absence of cracks in the same environment at 38 and 21°C (100 and 70°F) are apparent in Fig. 8.1. In all cases, except in the presence of sulfide, the reduction in area at the time of failure was 38 to 40%. The formation of cracks in 0.2*M* NH_4HO_3 at 66°C and the absence of cracking at 21°C agree with the results obtained with U-bend specimens exposed

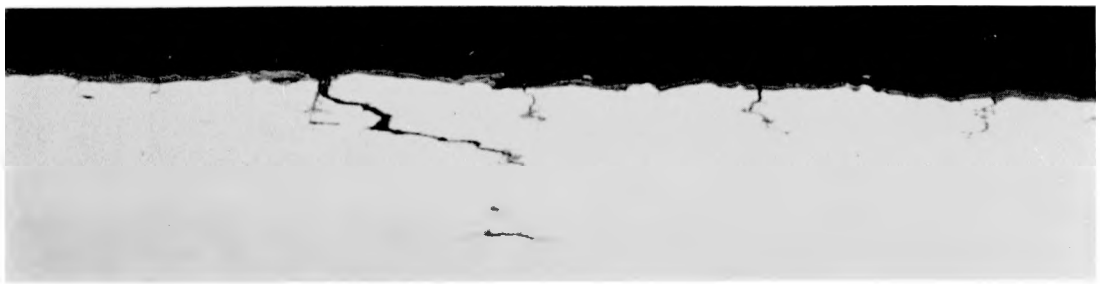

66°C Y-140169

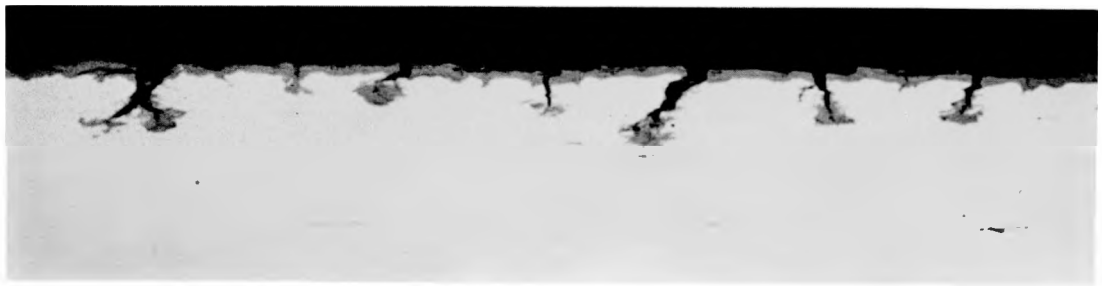

52°C Y-140166

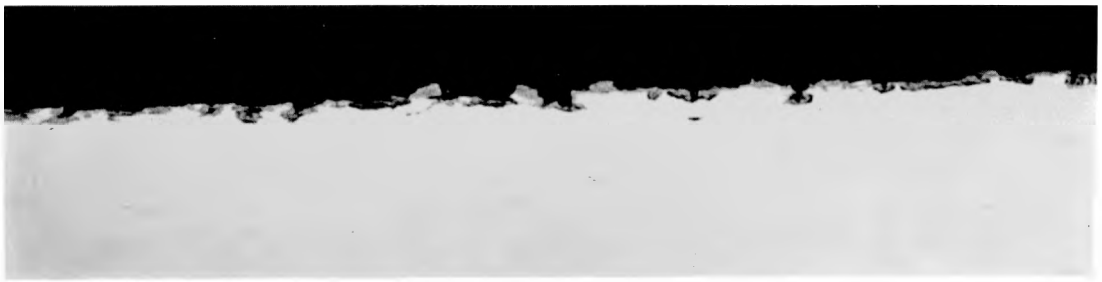

38°C Y-140165

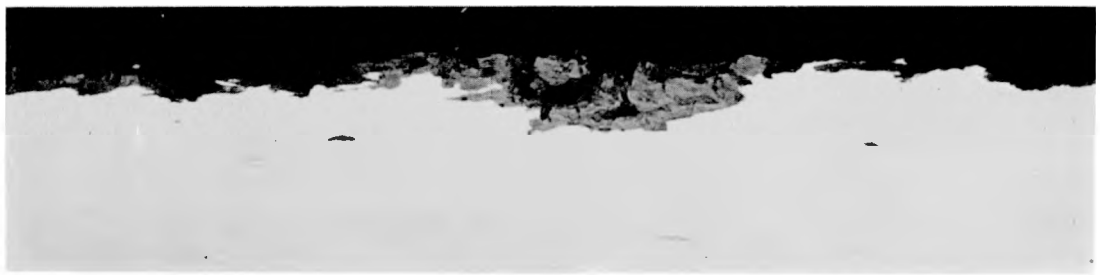

21°C Y-140170

Fig. 8.1. Longitudinal section of 1080 steel wires strained in 2*M* NH_4NO_3 at different temperatures.

to the same solution; U-bend specimens cracked in a few days at 66°C but remained intact at 21°C during 100-day tests.

Cracking produced in the presence of H_2S is caused by hydrogen embrittlement; and, when cracking occurred, reductions in area at failure were very low. No reduction in area could be measured in tests 16 and 17, and a reduction of only 4% was found in tests 22 and 23. Figure 8.2 shows one of several relatively long cracks observed on the specimen used in test 17. This crack was well removed from the fracture.

A literature search is being conducted to determine the behavior of high-strength carbon steels in environments similar to those that could exist around steel tendons when used in prestressed containers. Any future experimental program will be based on the information developed in this study.

Fig. 8.2. Longitudinal section of 1080 steel wire strained in 0.1*M* H_2S at 21°C.

ORNL/NUREG/TM-120
Dist. Category NRC-5

Internal Distribution

1. Seymour Baron
2. R. G. Berggren
3. S. E. Bolt
4. R. H. Bryan
5. J. P. Callahan
6. D. A. Canonico
7. S. J. Chang
8. R. D. Cheverton
9. C. E. Childress
10. W. E. Cooper
11. J. M. Corum
12. W. B. Cottrell
13. G. G. Fee
14. M. H. Fontana
15. W. R. Gall
16. M. J. Goglia
17. W. L. Greenstreet
18. R. C. Gwaltney
19. J. F. Harvey
20. M. R. Hill
21. P. P. Holz
22. H. W. Hoffman
23. G. Hofmann
24. S. K. Iskander
25. M. A. Karnitz
26. K. K. Klindt
27. Milton Levenson
28. R. E. MacPherson
29. R. W. McClung
30. J. R. McGuffey
31. J. G. Merkle
32. C. A. Mills
33. S. E. Moore
34. F. H. Neill
35. H. A. Photo (Y-12)
36. G. C. Robinson
37. C. D. St. Onge (Y-12)
38-39. Myrtleen Sheldon
40. G. M. Slaughter
41. C. B. Smith
42. G. C. Smith
43. J. E. Smith
44. I. Spiewak
45. W. J. Stelzman
46. D. G. Thomas
47. J. R. Weir, Jr.
48-97. G. D. Whitman
98. W. J. Wilcox
99. Patent Office
100-101. Central Research Library
102. Y-12 Document Reference Section
103-107. Laboratory Records Department
108. Laboratory Records RC

External Distribution

109-116. Director, Office of Nuclear Regulatory Research, Nuclear Regulatory Commission, Washington, D.C. 20555

117. Director, Reactor Division, Energy Research and Development Administration, Oak Ridge Operations Office

118. Director, Research and Technical Support Division, Energy Research and Development Administration, Oak Ridge Operations Office

119-284. Special HSST Distribution

285-588. Given distribution under category NRC-5 (25 copies — NTIS)

☆ U.S. GOVERNMENT PRINTING OFFICE: 1977-748-189/205